Master's thesis

NTNU
Norwegian University of Science and Technology
Faculty of Natural Sciences
Department of Materials Science and Engineering

Ola Sveen

Characterization of the Microstructural Development through Screw Extrusion of AA6060 and AA6082

Master's thesis in Materials Science and Engineering
Supervisor: Oddvin Reiso
Co-supervisor: Kristian Grøtta Skorpen, Trond Furu, Hans Jørgen Roven, Ida Westermann

June 2021

NTNU
Norwegian University of Science and Technology

Ola Sveen

Characterization of the Microstructural Development through Screw Extrusion of AA6060 and AA6082

Master's thesis in Materials Science and Engineering
Supervisor: Oddvin Reiso
Co-supervisor: Kristian Grøtta Skorpen, Trond Furu, Hans Jørgen Roven, Ida Westermann
June 2021

Norwegian University of Science and Technology
Faculty of Natural Sciences
Department of Materials Science and Engineering

NTNU
Norwegian University of Science and Technology

Abstract

Increased recycling of materials will play a key role in accelerating the transition towards a more sustainable future and circular economy. The metal continuous screw extrusion technology (MCSE) is a novel solid-state recycling technology, transforming scrap into extruded profiles. A key part of industrializing the technology and developing robust microstructural models is to understand the microstructural development through the screw extruder. In this study, AA6060 and AA6082 have been screw extruded with CO_2 as cover gas. A full characterization, from feedstock material to screw extruded profiles, has been performed. Recrystallization behaviour and evolution of intermetallic particles through the screw extruder have been assessed, in addition to grain mapping, inspection of dispersoids and precipitates, and mechanical testing of the screw extruded profiles. A standard ram extruded 6082 profile was used as a comparison.

The results from this study show that grain structure development through the screw extruder is comparable to the standard ram extrusion process. For the 6060 trial it was found that material located in zones with slow replacement consisted of either coarse elongated grains or equiaxed grains, and small elongated grains in shear intensive zones. Since the aluminium butt sections from the screw extrusion chamber were slowly cooled from 560 °C, it seemed likely that the 6060 material had initiated static recrystallization. A hypothesis for fragmentation of AlFeSi-particles through the screw extruder was followed up but not confirmed by inspection in light optical microscopy.

Screw extruded profiles displayed greater recrystallization resistance compared to ram extruded samples. This was suggested to be caused by lower strain rates and higher temperatures during screw extrusion, thus a smaller driving force for recrystallization. CO_2 had a seemingly positive effect on porosity, but could not be singled out as the only factor, as temperature during screw extrusion and thickness of feedstock material varied. In ram extruded 6082 particle analysis showed between 3 and 9 times higher number density of dispersoids compared to screw extruded 6082. Further analyses did not provide a clear answer as to why. Screw extruded 6082 outperformed ram extruded 6082 in tensile testing, T6 condition. While screw extruded 6082 reached tensile strengths of ∼350 MPa, ram extruded 6082 only reached ∼290 MPa. Fractography suggested strong crystallographic anisotropy in ram extruded 6082 samples in T6 condition, which was believed to be the main reason causing the difference.

Sammendrag

Økt resirkulering av materialer vil spille en avgjørende rolle i å fremskynde overgangen til en mer bærekraftig fremtid og sirkulær økonomi. Skruekstrudering er en nyskapende resirkuleringsteknologi som omdanner skrap til ekstruderte profiler. For å industrialisere teknologien og utvikle robuste mikrostrukturmodeller trengs det økt forståelse av hva som skjer i materialet under skruekstruderingen. I denne oppgaven har det blitt gjennomført skruekstrudering av AA6060 og AA6082 med CO_2 som dekkgass. Materiale fra granuler til ekstruderte profiler har blitt karakterisert. Rekrystallisering og intermetalliske partikler har blitt undersøkt gjennom skruekstruderen, i tillegg til kornstruktur, analyse av dispersoider og presipitater, og mekanisk testing av ekstruderte profiler. Resultater har blitt sammenlignet med en standard direkte ekstrudert 6082.

Resultatene viser at utvikling av kornsturktur gjennom skruekstrudering er sammenlignbar med standard ekstrudering. For 6060 ble det observert enten grove langstrakte korn eller ekviaksede korn i soner med langsom materialflyt, og smale langstrakte korn i skjærintensive soner. Siden materialet fra ekstruderingskammeret ble sakte avkjølt, er det sannsynlig at mikrostrukturen til 6060 skyldes statisk rekrystallisering. En hypotese for oppbrytning av AlFeSi-partikler gjennom skruekstruderen ble undersøkt men ikke bekreftet gjennom analyser i lysmikroskop.

Skruekstruderte profiler viste en bedre motstand mot rekrystallisering sammenlignet med standard ekstruderte profiler. Det ble foreslått at lavere tøyningshastighet og høyere temperatur under skruekstrudering var årsaken. Enkelte skruekstruderte prøver med CO_2 som dekkgass viste mindre tegn til porøsitet, men effekten kunne ikke tilskrives CO_2 alene, grunnet noe varierende temperatur under skruekstrudering og tykkelse på granuler. Partikkelanalyser viste at standard ekstrudert 6082 hadde mellom 3 og 9 ganger høyere antallstetthet av dispersoider sammenlignet med skruekstrudert 6082. Videre analyser ga ikke et entydig svar på hvorfor. Strekktesting viste at skruekstrudert 6082 nådde høyere verdier for flytespenning og strekkfasthet sammenlignet med standard ekstrudert 6082, begge i T6-tilstand. Mens skruekstrudert 6082 nådde rundt 350 MPa i strekkfasthet, ble det for standard ekstrudert 6082 bare oppnådd rundt 290 MPa. Fraktografi viste sterk krystallografisk anisotropi i standard ekstrudert 6082 i T6-tilstand, noe som ble antatt å være hovedårsaken til forskjellen i resultater fra strekktesting.

Preface

This master's thesis is written at NTNU, Department of Materials Science and Engineering, during spring 2021. The resulting work is a collaboration between NTNU and Norsk Hydro.

I hereby declare that this work has been carried out independently and according to the examination regulations of The Norwegian University of Science and Technology (NTNU).

Trondheim, June 15$^{\text{th}}$, 2021

Ola Sveen

Ola Sveen

Aknowledgements

I would like to thank the following list of people for invaluable help and guidance throughout the project:

- Adjunct Prof. Oddvin Reiso[1] and Dr. Kristian Grøtta Skorpen[1] for introduction to the screw extrusion technology, dozens of meetings and phone calls, and contagious enthusiasm.
- Prof. Hans Jørgen Roven[2], Adjunct Prof. Trond Furu[1] and Assoc. Prof. Ida Westermann[2] for help with administrative work.
- Staff Engineer Berit Vinje Kramer[2] for guidance and tutoring in metallographic lab.
- Engineer Birgitte Sofie Karlsen[3] for specimen preparation for TEM.
- Chief Engineer Pål Christian Skaret[2] for mechanical testing.
- Senior Engineer Yingda Yu[2] for help with analysis in SEM, and being extra helpful during a period with downtime in the SEM lab.
- PhD candidate Håkon Wiik Ånes[2] for help with particle analysis and EBSD.
- Prof. Bjørn Holmedal[2] and Dr. Tomas Manik[2] for fruitful discussions on results from EBSD.
- Prof. Randi Holmestad[2] for providing access to TEM through NORTEM on short notice.
- Senior Engineer Emil Christiansen[2] for performing all investigations in TEM.
- Sigmund and Martine for late conversations on screw extrusion and being a part of the "screw crew".
- My family and Marte for continuous support and encouragement throughout this master's thesis.

[1]Hydro Aluminium, Sunndalsøra.

[2]Norwegian University of Science and Technology (NTNU), Trondheim.

[3]SINTEF Industri, Trondheim.

Table of Contents

1 Introduction

Sustainability and use of clean energy have been a part of Norsk Hydro for a century, utilizing the geographical advantages of Norway through electricity produced from hydropower. Surges in average global temperature [1], together with implications from the urgent Paris Agreement [2], call for new initiatives in the industry. In 2019 Norsk Hydro followed up by introducing its new initiative: sustainability and profitability [3].

Although the transition towards a more sustainable aluminium industry has been greatly accelerated the past few years, Norsk Hydro, in collaboration with NTNU, patented a groundbreaking solid-state recycling technology of aluminium in 2008, the metal continuous screw extrusion (MCSE) technology [4]. Early reports of the technology suggest ca. 90 % energy savings compared to conventional remelting and ram extrusion of aluminium [5]. Since 2008 the technology has been proven and subject to research from both students and researchers, e.g. two PhD theses [6, 7], gaining insight into metallurgical phenomena and optimization of design and operation. Figure 1.1 shows one possible application of MCSE. In this figure, aluminium waste from machining and silicon waste from wafer production are combined into a Low Energy Master Alloy (LEMA) using the MCSE process. The project is a collaboration between Norsk Hydro and Nuvosil, a start-up with aims of utilizing waste from the silicon industry. Research will begin in 2021 [8].

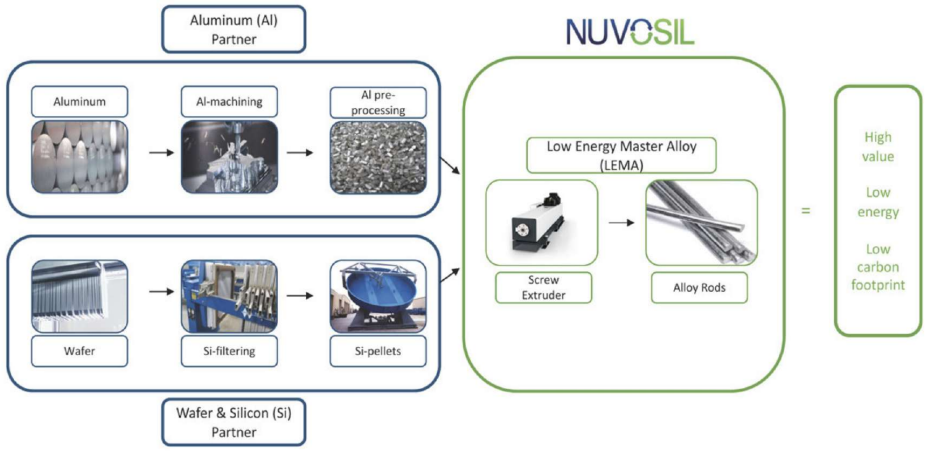

Figure 1.1: Value chain for the Low Energy Recycling (LER) project, utilizing both aluminium and silicon waste through the screw extrusion technology. From [9].

Up-scaling and successfully industrializing a technology requires a significant amount of research. For the screw extrusion technology, understanding the metallurgical phenomena occurring through the process, from input material to extruded profile, will help optimize design and better tailor-fit operational parameters, as well as provide a basis for microstructural models.

This work seeks to contribute to the ongoing research on the screw extruder by doing a full microstructural characterization of the material at various stages through the process. A step-wise guide for extracting and examining samples from the process, developed during the project work preceding this master's thesis [10], will be further tested and verified on two aluminium alloys, AA6060 and AA6082. CO_2 will be used as cover gas during screw extrusion and compared to the more traditional ambient air atmosphere. Light optical microscopy (LOM) will be used for microstructure and observations of AlFeSi-particles. Scanning electron microscopy (SEM) and transmission electron microscopy (TEM) will be used to perform in-depth grain structure analysis and particle examinations. Mechanical properties of extruded material will be tested through tensile testing and hardness measurements. A standard ram extruded AA6082 alloy will be used as a reference to the screw extruded AA6082 for all characterization methods.

2 Theory

2.1 Al-Mg-Si alloys

The Al-Mg-Si alloy class (or 6xxx series) is a group of heat treatable wrought alloys that dominates the market of extrusion ingots with its wide range of applicability. Several attributes of the alloy class contribute to its competitiveness, among those being mechanical properties, extrudability, corrosion resistance and surface appearance. These properties make the alloy class well suited for applications within automotive, building, shipping, electrical components and architectural [11]. The two primary constituents of the 6xxx series are magnesium (Mg) and silicon (Si), hence the name Al-Mg-Si alloys. Other important alloying elements are Mn, Cr and Cu, while Fe (inevitably) will be present as a contaminant [12]. Table 2.1 shows typical values for selected mechanical properties that are expected to be reached for the various sub-classes within the 6xxx series.

Table 2.1: Typical range of mechanical properties for 6xxx series. Taken from [12].

Mechanical property	Range
Yield strength, σ_y	190-360 MPa
Tensile strength, σ_u	220-390 MPa
Elongation at fracture, ε_f	12-17 %

Controlling the precipitation sequence of Mg_2Si is vital in the achievement of superior mechanical properties. One of the most important tools in that regard (for the metallurgist) is the phase diagram. The Al-Mg_2Si pseudoeutectic, binary system is shown in Figure 2.1, calculated by Zhang et al. [13]. From this phase diagram one can obtain the following information: Maximum solubility of Mg_2Si in Al is at 583.5 °C, with a calculated value of 1.91 wt%. At 13.9 wt% Mg_2Si the pseudoeutectic point exists, and a ternary phase can be seen in the range between 583.5 and 594 °C, consisting of L+Al+Mg_2Si.

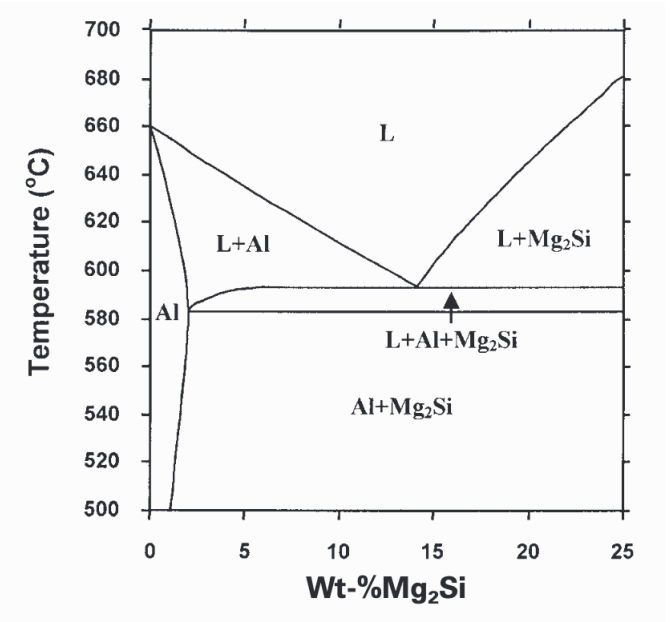

Figure 2.1: Pseudoeutectic binary Al-Mg_2Si phase diagram. Taken from [13].

Two important sub-classes within the 6xxx series are AA6082 and AA6060. An internal Metal Markets analysis by Norsk Hydro estimated that approximately 10 % of all aluminium alloys sold in Europe as extrusion ingots were of the type AA6082 [11].

2.1.1 AA6082

AA6082 is classified as a medium strength alloy and is typically offered for structural applications, for example structural beams, bumper rails and train floors [14]. The ultimate tensile strength of an AA6082 solid profile is shown as a function of ageing time in Figure 2.2. As can be seen, values close to 340 MPa can be reached given the correct temperature and ageing time balance. Other than strength, the alloy offers a good combination of ductility, weldability, corrosion resistance and anodizing response [14]. The chemical composition range of AA6082 is presented in Table 2.2. Although Mg and Si are the main alloying elements, AA6082 contains a significant amount of Mn (and sometimes Cr). Addition of Mn and/or Cr will result in the formation of dispersoids during homogenization, which will retard the (unwanted) recrystallization process. This causes the extruded material to preserve its fiber structure, thus increasing the overall strength [15, 16, 17].

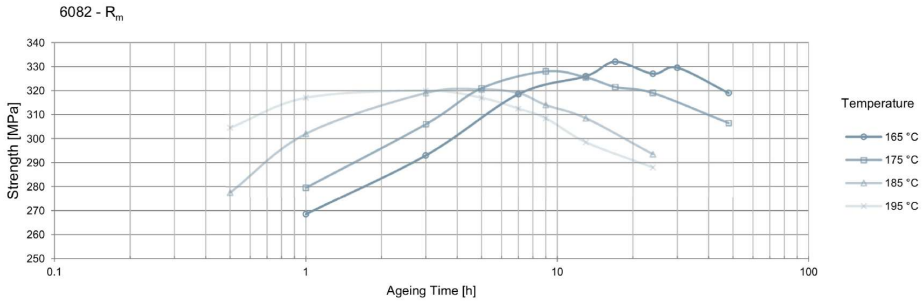

Figure 2.2: Ultimate tensile strength of an AA6082 profile as a function of ageing time. Solid profile, 200 x 3 mm, water quenched after extrusion, 24 h natural ageing prior to artificial ageing, properties in extrusion direction. Taken from [14].

2.1.2 AA6060

AA6060 is not as well suited as AA6082 for structural purposes requiring high strength, but is in turn excellent when high quality finish is desired. Typical applications of this series are architectural products, door and window frames, railings and furniture [18]. Ultimate tensile strength of an AA6060 solid profile is shown as a function of ageing time in Figure 2.3. Here, maximum values are close to 240 MPa, significantly lower than AA6082. While strength is a bit lower, the alloy has excellent corrosion resistance and is suitable for decorative anodizing, hence the applications mentioned above. Chemical composition is compared to AA6082 in Table 2.2. The lower alloying content (and no dispersoids) in AA6060 allows for recrystallization to occur after deformation.

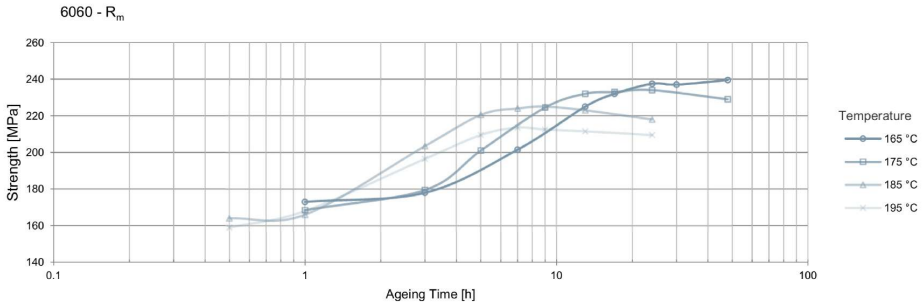

Figure 2.3: Ultimate tensile strength of an AA6060 profile as a function of ageing time. Solid profile, 200 x 3 mm, water quenched after extrusion, 24 h natural ageing prior to artificial ageing, properties in extrusion direction. Taken from [18].

Table 2.2: Chemical composition range (in wt%) of AA6082 and AA6060 as specified by the standard BS EN 573-3:2009.

Chemical element	AA6082	AA6060
Si	0.70 - 1.30	0.30 - 0.60
Fe	<0.50	0.10 - 0.30
Cu	<0.10	<0.10
Mn	0.40 - 1.00	<0.10
Mg	0.60 - 1.20	0.35 - 0.60
Zn	<0.20	<0.15
Ti	<0.10	<0.10
Cr	<0.25	<0.05
Al	Balance	Balance

2.2 Conventional ram extrusion

The typical (direct) extrusion process is shown in Figure 2.4. A force is applied to the billet through the ram, and the extrusion ingot is converted into an extruded rod of desired shape and size by material flow through the die. For aluminium, temperatures are often in the range 500-550 °C, where formability is higher [19]. The material flow is indicated by black arrows leading into the extrusion die.

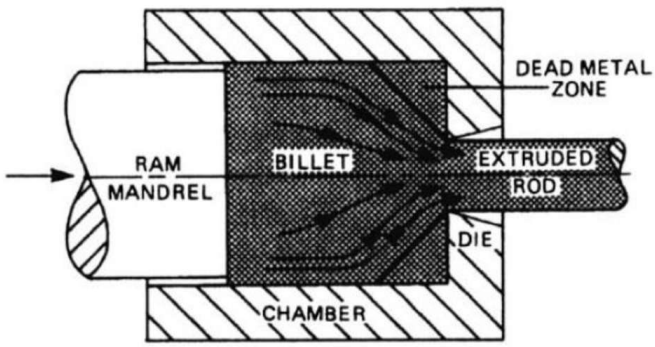

Figure 2.4: Schematic drawing of a direct extrusion process. Taken from [19].

2.3 Microstructure evolution during conventional extrusion

To allow for plastic flow of an extrusion ingot, i.e. area reduction through an extrusion die, temperatures close to that of the melting point of aluminium will be reached. The high temperatures will heavily influence the microstructure and affect the mechanical properties. A typical temperature-time plot of an extrusion ingot, from casting to ageing, is shown in Figure 2.5.

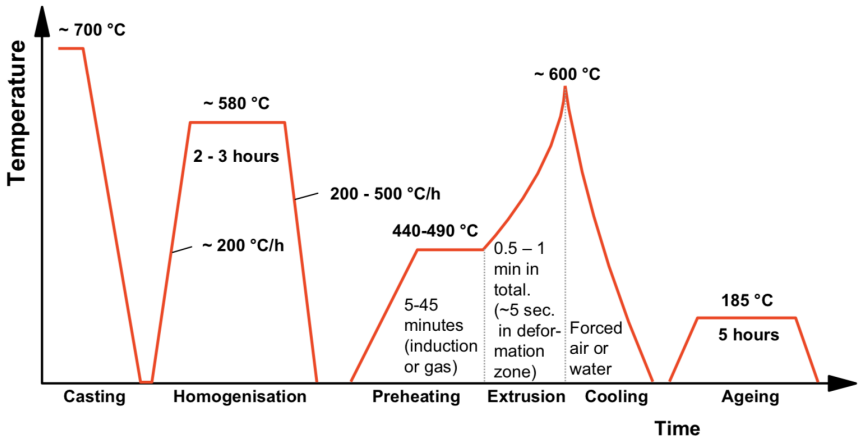

Figure 2.5: Typical temperatures and times used for conventional extrusion of Al-Mg-Si alloys. From [11].

The first step, casting, will produce billets of varying lengths and diameters. Due to some level of micro segregation in the solidification process, a homogenization step is performed after casting. Here, the billet is heated to an elevated temperature of approximately 580 °C. Several wanted microstructural effects occur at this temperature: achieving a more homogeneous distribution of alloying elements, spherodizing the brittle β-AlFeSi particles and transforming them into α-AlFeSi particles, dissolution of low melting point eutectics, and controlling the precipitation of dispersoid particles [11].

After homogenization the billet is typically transported to the last step prior to extrusion, namely preheating. By overheating the billet, higher extrusion speeds can be reached and thus increased productivity. Overheating is done by first heating the billet to a temperature above the solvus temperature of the alloy (to bring all the Mg and Si into solid solution) and then cooling it down to desired extrusion temperature fast enough to avoid new precipitation of Mg_2Si-particles [11]. The area reduction achieved through extrusion of aluminium typically results in two

types of structures (after extrusion and press quenching): one being a fibrous core of extruded grains with heavily sheared grains along the periphery, the other being a fibrous core surrounded by a shell of recrystallized grains [20]. The former typically applies for low-temperature extrusions, the latter in high-temperature extrusions. A typical microstructure evolution of aluminium through the ram extruder is shown in Figure 2.6.

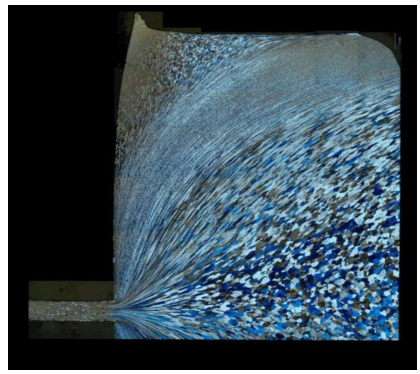

Figure 2.6: Grain structure through conventional ram extrusion of aluminium. (Printed with permission of Oddvin Reiso [11], originally from Anne Lise Dons, SINTEF.)

As will be explained in more detail in the next section, the material seeks towards recrystallization after extrusion in an attempt to lower its energy. Certain alloying elements, such as Mn or Cr, can retard this phenomena [15]. Figure 2.7 shows a comparison between two alloys in as-extruded condition, one not alloyed with Mn (AA6060) and one with 0.54 wt% Mn (AA6082).

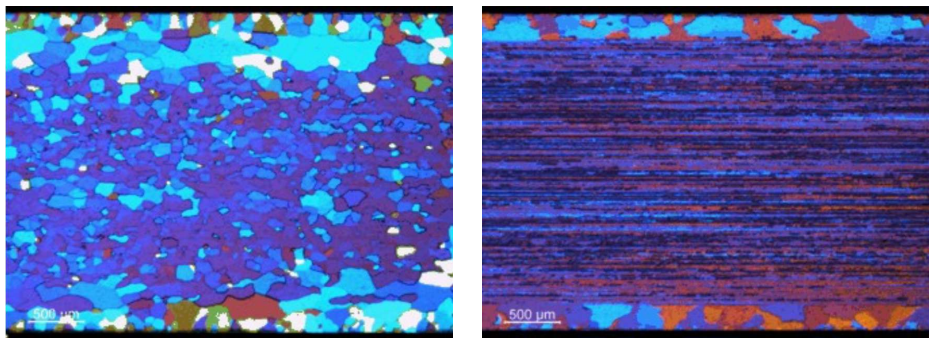

(a) AA6060. **(b)** AA6082.

Figure 2.7: Light optical micrographs of grain structures in aluminium, as-extruded condition. Taken from [21].

2.4 Recovery, recrystallization and grain growth

After thermo-mechanical processing, such as extrusion, the material will be in a thermomechanically unstable condition. The deformation imposed by the process will cause plastic deformation and increase the dislocation density, typically reaching values of about $10^{16}/\mathrm{m}^2$ in aluminium [22]. The stored energy in a crystalline material with dislocations may lower its energy by the process of recovery, recrystallization and grain growth [23]. Although these phenomena may occur in a continuous matter, i.e. recovery and recrystallization taking place gradually with no clear distinction, they are often regarded as separate phenomena and best described as discontinuous processes occurring heterogeneously throughout the material [23]. A description of each separate phenomena might be useful [24]:

- *Recovery*: The elevated temperature enhances atomic diffusion, which in turn causes the stored internal energy to be relieved through dislocation motion. Dislocation density decreases through rearrangement and annihilation. Subgrains, with boundaries being dislocation free, will grow. While the overall energy is lowered, it is still considered a metastable state.

- *Recrystallization*: The formation of new, strain-free and equiaxed grains with low dislocation densities. Driving force for the recrystallization is the stored energy imposed by the deformation process, and the material seeks toward an equilibrium state by nucleation and growth of new grains. This process will continue until the new grains consume the parent material. The process is heavily influenced by both temperature and time.

- *Grain growth*: Grain boundaries represent energy in the form of crystallographic misalignment between two areas of different atomic arrangement. Bonding energies are higher on grain boundaries because of higher bond angles compared to a perfect crystalline structure. Therefore, if left at an elevated temperature, the grains will grow in size in order to minimize the misalignment, thus decreasing the total energy associated with grain boundaries.

Recovery and recrystallization occuring during annealing after deformation are termed *static* annealing phenomena. For alloys such as AA6060, i.e. without dispersoids, recrystallization after extrusion typically occurs after a fraction of a second [25]. When the two phenomena take place during deformation at elevated temperatures, they are referred to as *dynamic* annealing phenomena. During deformation, such as extrusion, high strain rates and low temperatures will lead to more storage of dislocations and thus a higher driving force for recrystallization.

These two factors, strain rate and temperature, are commonly expressed through the well-known Zener-Hollomon parameter [26], given in equation 2.1.

$$Z = \dot{\varepsilon}\exp\left(\frac{Q}{RT}\right) \tag{2.1}$$

Where $\dot{\varepsilon}$ is the strain rate, Q the activation energy, R the gas constant and T the deformation temperature. The Zener-Hollomon parameter will give a representation of the amount of stored energy in the metal at a given deformation temperature, and is often related to recrystallization behaviour. It can readily be seen that large strain rates and lower temperatures will give higher values of Z. A simple estimate of the strain rate during conventional extrusion is made by Feltham [27]:

$$\dot{\varepsilon} = \frac{6D_B^2 V_R \ln R}{D_B^3 - D_E^3} \tag{2.2}$$

Where D_B and D_E are the billet and extrudate diameters, V_R the ram extrusion speed and R the extrusion ratio D_B^2/D_E^2.

2.5 Intermetallic particles and dispersoids in Al-Mg-Si alloys

Solubility of alloying elements drastically decreases when the aluminium melt solidifies. As a concequence, intermetallic phases with limited or no solubility will be present as particles in the aluminium matrix. They typically have a melting point different from that of aluminium and solidify with the residual melt, i.e. on grain and dendrite arm boundaries. They are often referred to as constituent or primary particles and tend to remain stable in subsequent thermo-mechanical processing [28].

In commercial pure aluminium, the maximum solubility of iron has been calculated to be 0.052 wt% [29, 30]. Together with other alloying elements present in 6xxx series, such as Mn and Si (and the parent material Al), Fe will precipate and form primary particles. Microstructure and phase composition in as-cast aluminium have been studied by numerous authors, such as Liu et al. [31, 32], and several Fe-containing primary particles have been observed. Examples are $\beta-Al_5FeSi$, $\alpha-Al_{15}(Fe,Mn)_3Si$ and $\pi-Al_8FeMg_3Si_6$. In literature the first two are often referred to as β-AlFeSi and α-AlFeSi.

As mentioned above (Section 2.3), one important task of the homogenization step is to transform the brittle β-AlFeSi phase into α-AlFeSi in order to increase productivity at the extrusion press [11]. In a bright field micrograph these phases are easily visible and will appear in a grey color, as opposed to the much lighter (gray)

colour of the aluminium matrix. Figure 2.8 shows one such successful transformation, where β-AlFeSi can be seen in Figure 2.8a and α-AlFeSi in Figure 2.8b. Mg_2Si-particles can also be observed.

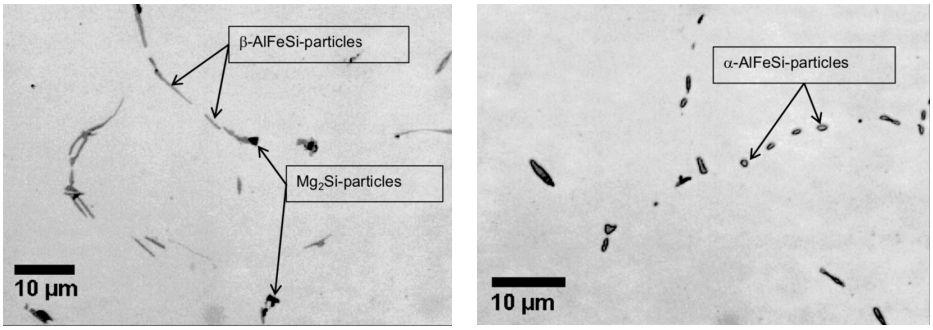

(a) As-cast. **(b)** Homogenized (580°C/ 2.5 h).

Figure 2.8: Light optical micrographs of intermetallic particles in samples from an Al-Mg-Si alloy. Alloy composition (wt.%): 0.47 % Mg, 0.44 % Si, 0.20 % Fe. From [11].

Mn and/or Cr are added in small amounts to modify the microstructure of certain alloys, for example AA6082. At elevated temperatures (400-580 °C), smaller particles containing Mn and/or Cr are formed, referred to as dispersoids [15], typically within a size range of 10-1000 nm [28]. They are widely dispersed in the aluminium matrix and are of much smaller sizes than the primary particles. Although the direct strengthening effect from dispersoids is relatively small, they have an important secondary effect in controlling recrystallization behaviour [15]. The dispersoids will act as pinning points for grain boundaries, thus retarding the recrystallization behaviour. This will allow the material to preserve its fibrous structure, which is advantageous with regards to strength.

2.5.1 Fragmentation of AlFeSi-particles through convential extrusion

The evolution of AlFeSi-particles through conventional extrusion has been investigated by Sheppard [20]. In an attempt to explain the origin of micro-die lines on the extrusion surface of aluminium, observations on the fragmentation of AlFeSi-particles were made. It was proposed that the high shear stress experienced at entry to the die throat of the extrusion press caused the fragmentation of larger AlFeSi-particles into smaller ones, interspersed with considerable cavitation. These smaller fragmented particles were then spherodized due to capillarity-driven processes. It was argued that the strings of voids created by the cavitation between fragmented AlFeSi-particles were the direct cause for the observed micro-die lines on the surface.

Figure 2.9 summarizes the observations. Figure 2.9a displays bands of small spherical AlFeSi-particles together with larger particles, while Figure 2.9b shows the disintegration of coarser AlFeSi-particles.

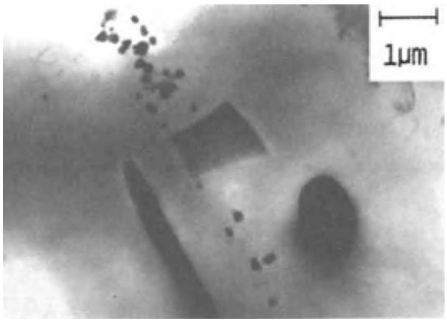

(a) Residual fragmented coarse AlFeSi and bands of spheroidized particles.

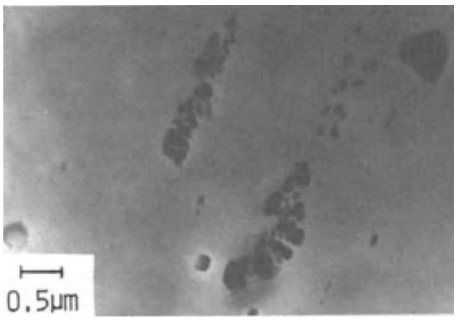

(b) Disintegration of coarse AlFeSi-particles.

Figure 2.9: Morphology of AlFeSi-particles in the outer layer of an extruded Al-Mg-Si alloy. Taken from [20].

2.6 Strengthening mechanisms

The Al-Mg-Si alloys gain most of their strength through artificial age hardening, and a significantly higher strength can be reached than in as-cast condition. For aluminium in general, there are typically four mechanisms of importance [33]:

- Work hardening (σ_ρ)
- Grain boundary strengthening (σ_{GB})
- Solid solution strengthening (σ_{ss})
- Precipitation hardening (σ_p)

A common assumption is that the stress contribution from each mechanism can be added independently into the overall strength of the alloy. However, as the mechanisms have a varying degree of contribution to the overall strength, Myhr et al. [34, 35] propose the following yield strength model for Al-Mg-Si alloys.

$$\sigma_y = \sigma_i + \sigma_{ss} + \sigma_p \tag{2.3}$$

Where σ_y is the yield strength, σ_i is the intrinsic contribution from pure aluminium, σ_{ss} is the contribution from alloying elements in solid solution and σ_p is the contribution from precipitates. A brief presentation of the four mechanisms will be

given in the following, with emphasis on precipitation strengthening. If not stated otherwise, the theory is based on Dieter [33].

2.6.1 Work hardening

Work hardening (or strain hardening) is typically used for metals that do not respond to heat treatment. Much of the theory behind work hardening can be explained on the basis of dislocations. Deformation of a metal causes interaction and multiplication of dislocations, restricting the motion of each dislocation as more is being produced. Dislocations will interact with each other and with barriers impeding their motion through the crystal lattice, thus increasing the stress necessary to further plastically deform the metal.

2.6.2 Grain boundary strengthening

Through extensive experimental studies conducted on bicrystals in the 20th century, a relationship between yield stress and grain size was found. Hall [36] and Petch [37] independently proposed the following relationship (which is now known as the Hall-Petch relation):

$$\sigma_y = \sigma_i + \frac{k}{\sqrt{D}} \tag{2.4}$$

Where σ_y is the yield stress, σ_i is the friction stress of the crystal lattice, k is a parameter that measures the relative hardening contribution of the grain boundaries and D is the grain diameter. As can be seen, yield stress is inversely proportional to the square root of the grain size, i.e. a decreasing grain size increases the yield stress of the metal. This is explained on the basis of dislocation motion and pile-up. When two neighbouring grains have different crystallographic orientations, the dislocation which is performing slip motion in a specific grain cannot continue when reaching a grain boundary. If stress is continually applied to the metal, dislocations will pile-up at grain boundaries, thus acting as barriers to the dislocation motion. To continue slip past the grain boundary a critical shear stress must be applied. If there are more grain boundaries in the metal (i.e. smaller grain size), dislocations will more frequently pile-up at grain boundaries and a higher stress is required to continue plastic deformation.

2.6.3 Solid solution strengthening

Elements in solid solution will disrupt the perfect crystalline lattice of the parent material and create a strain field that makes dislocation motion difficult. Solute atoms can either occupy lattice points through substitutional or interstitial solid

solution. The former is more likely for elements with a similar size to that of the host, while the latter is more likely for smaller atoms. The strengthening effect caused by elastic interaction is sketched in Figure 2.10. Here, the misfit of the solute atoms expands the lattice, causing a strain field to arise. A by-passing edge dislocation (with its own surrounding strain field) will interact and effectively be opposed by the strain field surrounding the solute atoms. This way, a higher (applied) stress is required for the dislocation to continue slip motion.

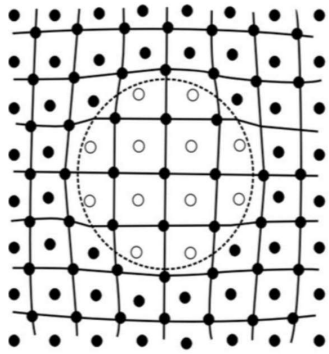

Figure 2.10: Strain field surrounding atoms in solid solution.

2.6.4 Precipitation hardening

Precipitation hardening (or age hardening) is the strength contribution achieved from fine precipitates in the metal that oppose dislocation motion. A necessity for precipitation hardening to occur is a decreasing solubility with temperature of a second phase, such as Mg_2Si in Al, shown in Figure 2.1. Al-Mg-Si alloys are therefore well suited and can produce hardening precipitates by careful thermo-mechanical processing.

First step in the process is solutionizing, or solid-solution heat treatment (SSHT), at a temperature above the solvus line. The material is held at this temperature until all alloying elements are in solid solution. Next, the material is quenched to room temperature, i.e. rapid cooling from a high temperature. The alloying elements will now be in solid solution and, because of decreasing solubility, form a super saturated solid solution (SSSS). Then, the material is heated to an elevated temperature (typically in the range 160-190 °C) in order to accelerate the formation of metastable and coherent particles. The strain field produced by the coherent particles will increase the hardness because of interactions with dislocations. If the material is artificially aged for too long, loss of coherency will occur and equilibrium

phases will form. A proposed precipitation sequence for Al-Mg-Si alloys is given in Equation 2.5 [38, 39, 40].

$$SSSS \rightarrow atomic\ clusters \rightarrow GP\ zones \rightarrow \beta'' \rightarrow \beta', \mathrm{U1}, \mathrm{U2}, \mathrm{B}' \rightarrow \beta \tag{2.5}$$

Figure 2.11 shows the strength of an Al-Mg-Si alloy as a function of ageing time. As can be seen, maximum level of hardness is reached when a combination of β' and β'' is present. Table 2.3 provides more detailed information on these precipitates.

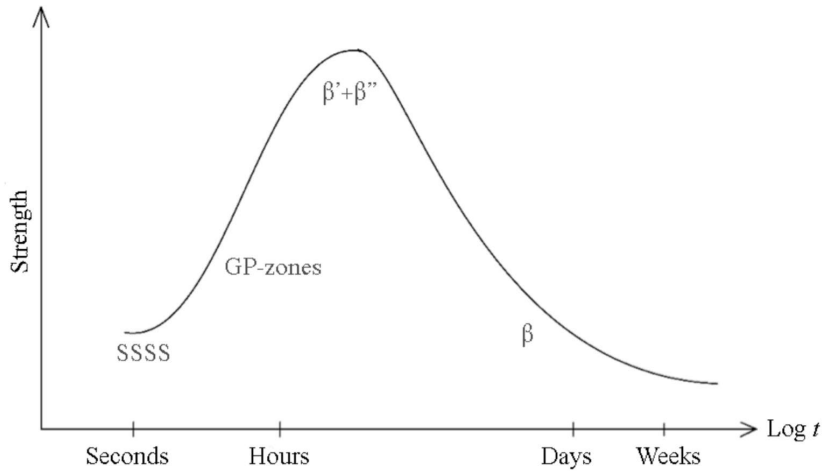

Figure 2.11: Strength of an Al-Mg-Si alloy as a function of ageing time. From [41].

Table 2.3: Precipitates and phases in Al-Mg-Si alloys [42, 43, 44, 45, 46].

Phase	Shape	Formula	Space group
GP-zone	Semi-coherent needle	$AlMg_4Si_6$	Monoclinal
β''	Semi-coherent needle	Mg_5Si_6	Monoclinal
β'	Semi-coherent needle	$Mg_{1.8}Si$	Hexagonal
U1	Needle	$MgAl_2Si_2$	Hexagonal
U2	Needle	$Mg_4Al_4Si_4$	Hexagonal
B'	Lath	$Mg_9Al_4Si_7$	Hexagonal
β	Incoherent plates	Mg_2Si	Cubic

When modelling the contribution of precipitates to the macroscopic yield strength in aluminium, a common assumption is to approximate the needles as equivalent spherical particles, as the NaMo model does [34]. Other models, e.g. the Holmedal model [47], takes into account needle shaped particles piercing more slip planes than spherical ones. Following the arguments of Holmedal, β"-needles will grow in <001> directions and act as dislocation barriers in the {111} slip planes. Therefore, obstacle strength will increase as a function of precipitate size – both length and cross-sectional area. In addition, strength increases with number density of precipitates [34].

2.7 Quench sensitivity

A material is said to be quench sensitive if the strength after ageing decreases with decreasing cooling rate from solution temperature [15]. The ageing potential of 6xxx alloys is then reduced by the slow cooling, which may cause Mg and Si to form coarse precipitates on heterogeneous nucleation sites, such as primary particles and grain boundaries. Dispersoids, e.g. Mn and Cr in 6082, will act as potent nucleation sites for the non-hardening β'-phase and lead to a lower ageing potential by reducing the supersaturation of Mg and Si [48].

2.8 Oxidation inhibition in aluminium alloys

Oxidation of aluminium is an unwanted reaction with the surrounding atmosphere, causing mass gain of the oxide layer by diffusion of elements from the bulk material and subsequent reactions with the oxidizing atmosphere. Figure 2.12 shows the mass gain of an AA6010 alloy as a function of holding time at various temperatures. It may be observed that the oxidation process rapidly increases with holding temperature.

Oxidation inhibition in aluminium alloys has been extensively researched in the past, primarily focused on the Al-Mg system (5xxx series) during liquid processing [49, 50, 51]. Attempts to reduce the rate of oxidation have included:

- Small additions (2-200 ppm) of beryllium (Be) to the melt, forming a protective BeO layer at the oxide-metal interface [49, 50, 52, 53]
- Small additions of yttrium (Y) to the melt [54]
- Pure argon (Ar) atmosphere [55]
- Small amounts of CO_2 to the surrounding atmosphere [51, 54, 55, 56]

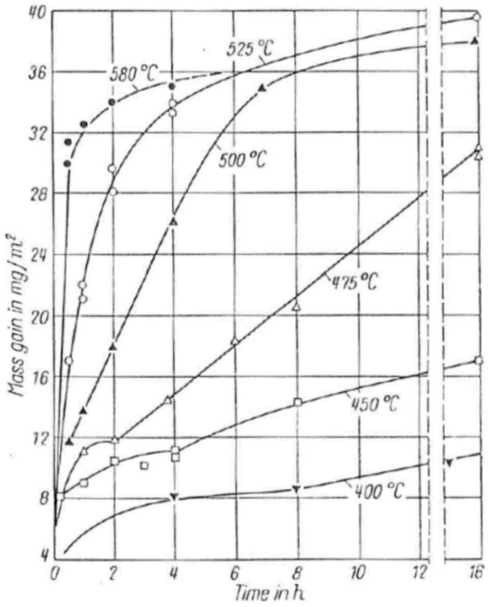

Figure 2.12: Mass gain per area of an AA6010 alloy as a function of holding time at various temperatures, in dry air atmosphere. Taken from [57].

Traditionally, beryllium has been used as an oxidation inhibitor for Al-Mg alloys. However, strong negative health impacts have been found related to the use of beryllium, and a more viable option is therefore desirable [58]. Smith et al. [54] performed trials with (a) yttrium addition, and (b) CO_2 as cover gas during heating of an Al-Mg alloy (5 wt% Mg) over various holding times at 750 °C. Addition of 100 ppm Y had only limited impact on the oxidation, while as little as 5 % CO_2 to the air atmosphere reduced oxidation close to that of beryllium additions. Similar findings on the effect of CO_2 have been done by Smith et al. in other papers, e.g. [52], where small concentrations of CO_2 in the cover gas gave a pronounced effect on the oxidation inhibition in an Al-Mg5 alloy.

More recently, Solem et al. [55] assessed the effect of (a) synthetic air, (b) pure Ar atmosphere, and (c) CO_2 as cover gas on the rate of oxidation of an Al-Mg-Si alloy with a holding time of 7 hours at 750 °C. When changing from synthetic air to pure Ar, a decrease in mass gain from 12.33 % to 2.80 % was measured. More promising, the trial with 4 % CO_2 as cover gas resulted in a mass gain of only 0.46 %, significantly lower than the other two.

A mechanism behind the inhibiting effect of CO_2 on oxidation of Al-Mg alloys was

proposed by Smith et al. [56]. Characterization of the oxide layer morphology formed during heating of the melt strongly suggested an interaction between CO_2 molecules and the MgO layer on the surface. This lead to the conclusion that the oxide layer continues to grow around the CO_2 molecules, reducing the partial pressure of oxygen below the oxide surface. Further, Smith et al. suggested that Mg and CO_2 react to form an Mg-O-C phase, structurally different to the MgO formed in air atmospheres. Diffusion of Mg from bulk will then be reduced by the carbon-rich MgO layer, which acts as "cap". This results in less Mg available for oxidation at the surface.

2.9 Metal Continuous Screw Extrusion

Extensive research on solid-state recycling of aluminium between NTNU and Norsk Hydro resulted in the development of the metal continuous screw extrusion (MCSE) technology [4]. A principal sketch of the screw extruder is shown in Figure 2.13. Here, aluminium granules are fed from the rear part of the machine through a small hole. The granules are transported forward by a rotating Archimedes screw (powered by a motor) and subsequently heated and compacted by the frictional forces between the rotating screw and (stationary) container. Pressure is generated by the continuous feeding of new granules and aluminium is compacted into a solid plug in front of the screw. Eventually, when pressure is high enough, material will be extruded through the extrusion die [6].

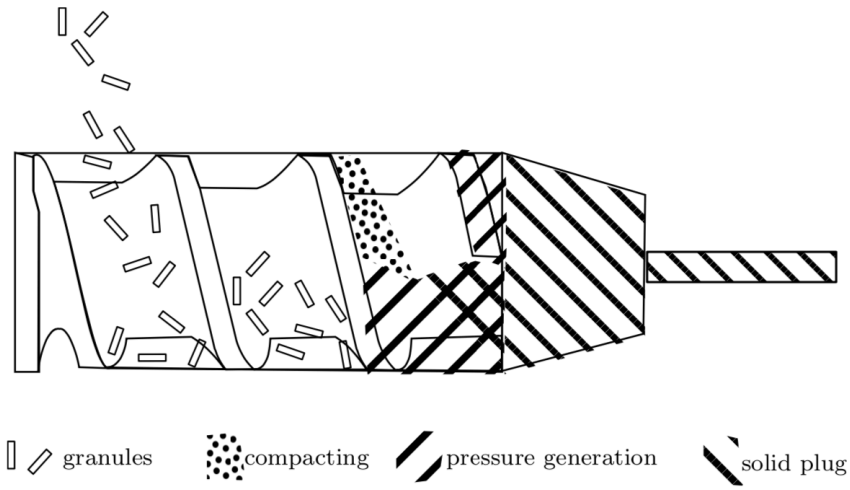

Figure 2.13: Sketch of the screw extruder, highlighting the stages from granules to solid plug. Taken from [4].

2.10 Literature review from selected studies on MCSE

2.10.1 Material flow

Material flow through the screw extrusion process has been investigated by Widerøe and Welo [59], using contrast material techniques and batch-wise feeding. Figure 2.14 shows the longitudinal cross sections of aluminium butt sections after extrusion trials using a double flight screw. The figures reveal the location of dead zones and zones of slow material movement. These are located at the end of the screw channel and close to the container wall. In Figure 2.14b, these are indicated by "Dead zone" and "Slow replacement". Material is primarily transported from the flight tip and inward, towards the die orifice, i.e. along the path of lowest resistance.

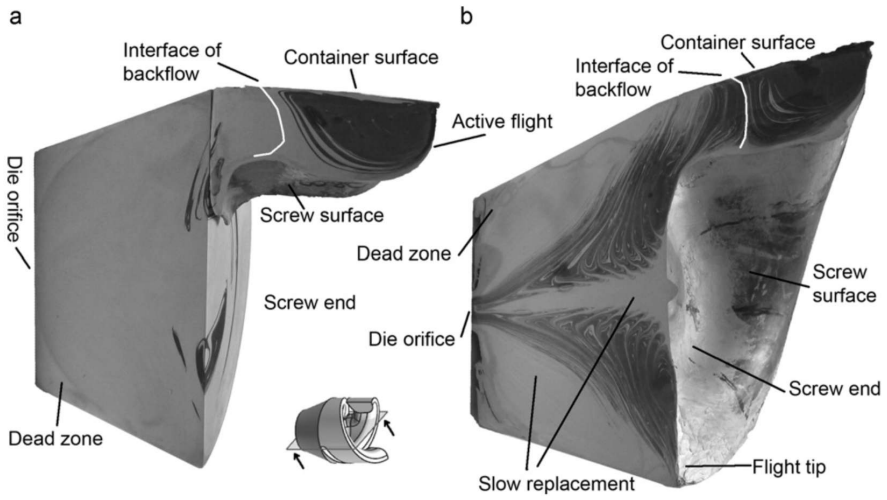

Figure 2.14: Etching of aluminium plugs from double flight screw extrusion, showing the material flow: (a) after 60 s of contrast material feeding; (b) after 100 s. Extrusion direction is horizontally to the left in both images. Taken from [59].

The main findings from the study of Widerøe and Welo were summarized in a schematic drawing shown in Figure 2.15. The speed of which material is replaced by is indicated by the size of the arrows.

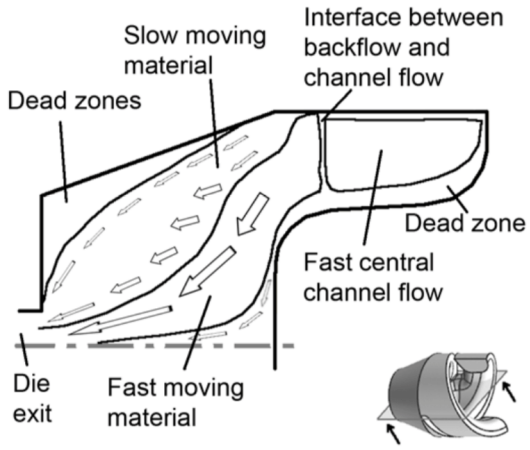

Figure 2.15: Schematic drawing of material flow through screw extrusion, with key findings from studies using a double flight screw. Taken from [59].

2.10.2 Total accumulated strain in MCSE

Skorpen et al. [60] formulated a comprehensive model on the total accumulated strain through the MCSE technology. In it, four contributions to the total strain were considered and linearly added to the total strain. Figure 2.16 shows a schematic drawing of the screw extruder with approximate locations of the four areas. They are (1) extrusion; (2) extrusion chamber region; (3) screw tip region and (4) screw channel region.

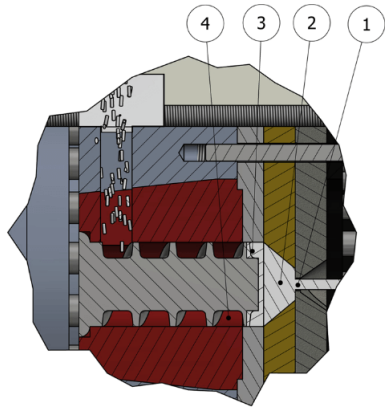

Figure 2.16: Schematic drawing of the screw extruder together with areas contributing to the total strain: (1) extrusion; (2) extrusion chamber region; (3) screw tip region and (4) screw channel region. Taken from [60].

The total accumulated strain is presented as:

$$e_{tot} = e_1 + e_2 + e_3 + e_4 \tag{2.6}$$

Numeric estimates from their studies on an Al-5%Mg alloy resulted in a total accumulated strain of ∼15 for a Ø10 mm profile. In most cases, strain in the extrusion chamber region, i.e. Area (2) in Figure 2.16, contributed with as much as ∼50 % of the total strain.

2.10.3 CO_2 as cover gas during screw extrusion

Ragnvaldsen [61] studied (among other things) the effect of CO_2 as cover gas during screw extrusion of a 5183 Al-Mg alloy matrix reinforced with TiC nanoparticles. By using a small addition of CO_2 to the atmosphere, a significant reduction in porosity of the screw extruded profiles was found, compared to the traditional ambient air atmosphere. Figure 2.17 shows a comparison between two screw extruded profiles; (a) without CO_2 as cover gas, and (b) with CO_2 as cover gas.

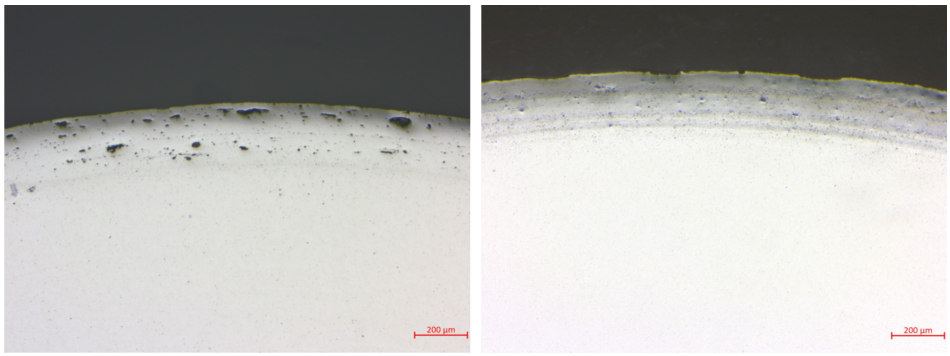

(a) With ambient air atmosphere. **(b)** With CO_2 as cover gas.

Figure 2.17: Light optical micrograph of screw extruded 5183 alloy with TiC nanoparticles. Taken from [61].

3 Experimental

The following chapter provides a detailed description of material characteristics, methods and techniques utilized for experiments and analyses. As the present work is partially a continuation of the project work preceding it, a flow chart displaying activities in both is presented in Figure 3.2. Please note, while both paths start from identical extrusion ingots, they diverge in terms of different processing conditions. Also, colour coding (i.e. red or green) indicates which activities are performed in each semester.

3.1 Base materials

Material was provided in the form of Ø95 mm extrusion ingots, AA6060 and AA6082, produced by Hydro Sunndal. The billets were DC-cast and subsequently homogenized. The chemical compositions are shown in Table 3.1, while homogenization parameters are shown in Figure 3.1. Billets were machined by Finmekanisk at NTNU into small granules, to be used as feedstock material for the screw extrusion process. Visual appearance of the granules can be seen in Figure 3.3.

Table 3.1: Chemical compositions of extrusion ingots used to produce feedstock (wt.%).

Material	Si	Fe	Cu	Mn	Mg	Zn	Ti	Cr	Al
AA6060	0.45	0.20	0.001	0.02	0.50	0.004	0.01	0.001	Balance
AA6082	1.08	0.26	0.003	0.56	0.65	0.01	0.02	0.16	Balance

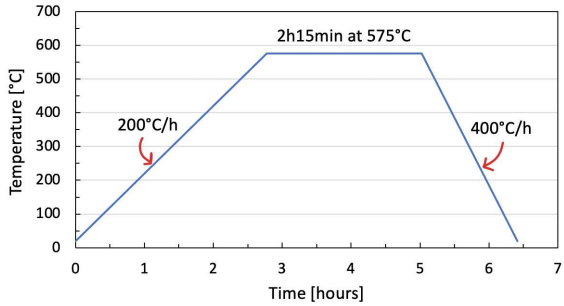

Figure 3.1: Homogenization procedure for extrusion ingots AA6060 and AA6082. The procedure starts and ends at room temperature. Heating and cooling rates are displayed.

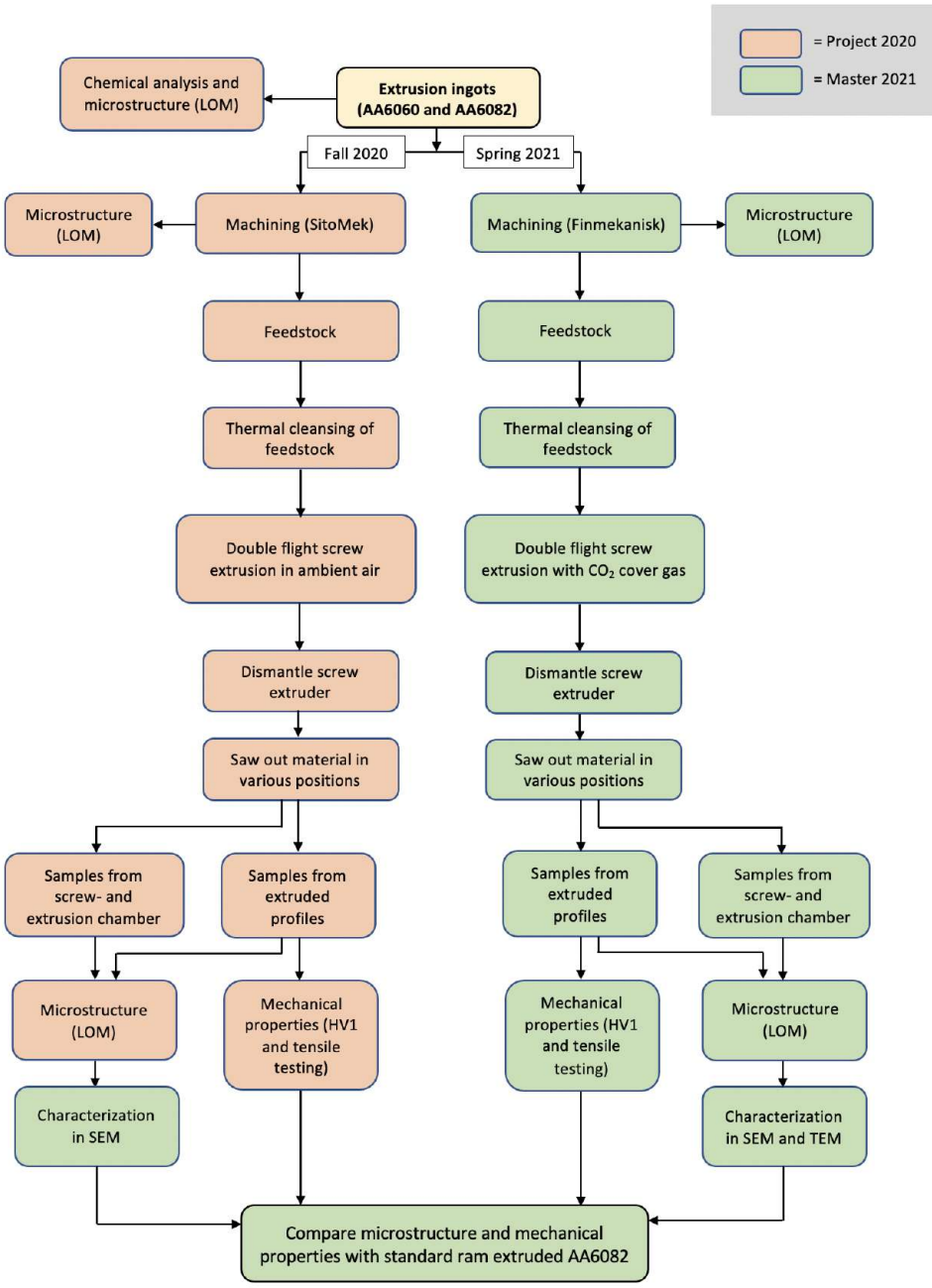

Figure 3.2: Flow chart showing activities in both project work and master's thesis.

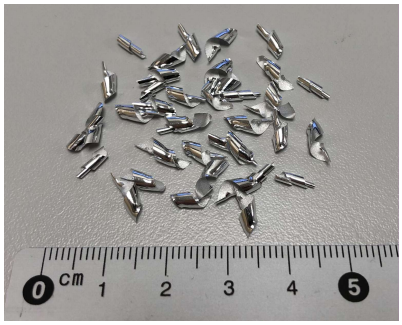

Figure 3.3: Feedstock material machined from AA6060 extrusion ingot by Finmekanisk. Similar shapes and sizes of feedstock were machined for the AA6082 batch. Thickness of the granules was about 100 µm.

3.2 Screw extrusion

The following section presents operational considerations during production of the screw extruded profiles, as well as retrieval of aluminium butt sections (hereon referred to as "plugs") left in the screw extrusion chamber.

Figure 3.4 shows the flow of aluminium from extrusion ingot to screw extruded profile, along with the main process steps. Two series of screw extruded profiles were successfully produced as a part of this thesis. One using AA6060 granules as feedstock, and one using AA6082 granules. Prior to screw extrusion the feedsotck material was heated at 350 °C for 30 min. The thermal cleansing was based on the work done by Bilsbak [62], where the main purpose is to remove grease and dirt from previous process steps.

The trials were performed using a double flight screw and a die opening of Ø10 mm. CO_2 was added to the ambient air atmosphere inside the screw extrusion chamber, and the resulting atmosphere thus contained a mixture of CO_2 and dry air. The CO_2 gas was added from a hose connected to a bottle at 3 bar pressure, guided through a copper tube for stability. For both trials, gas flow was equal to 70 % of max, where max was 2 NL/min. Feedstock and gas were added through the same funnel, above the screw extruder, as shown in Figure 3.4. Although the ratio of CO_2 to dry air was not logged, it was believed that concentrations of CO_2 were high enough to have an effect on oxidation. This assumption was based on promising results with as little as 4 % CO_2 as an oxidation inhibitor of aluminium alloys during heating (Smith [54] and Solem [55]), as presented in Section 2.8.

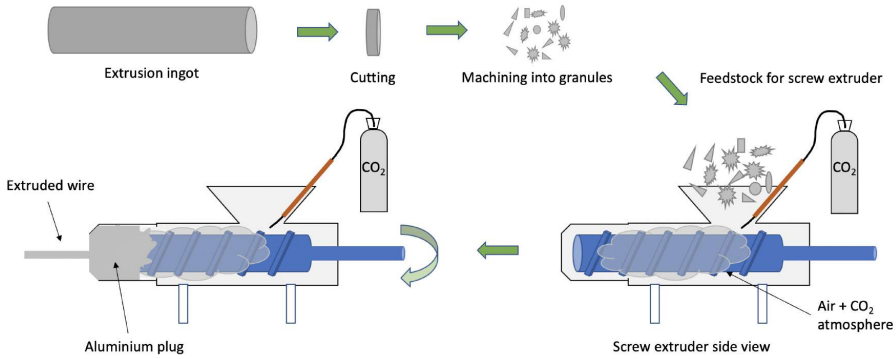

Figure 3.4: Flow of aluminium from extrusion ingot to screw extruded profile. Addition of CO_2 gas to the atmosphere is indicated by a hose connected to a battery, guided through a copper tube for stability.

Prior to extrusion, the screw extruder was preheated by a copper induction coil in front of the screw. The profile temperature at the exit of the die was stabilized around 560 °C for both trials. Figure 3.5 shows the six main steps before, during and after screw extrusion. Table 3.2 summarizes operational parameters, such as atmosphere, temperature and extrusion speed for all extrudates considered in this thesis. The two highlighted trials in bold, named **MCSE 6060C** and **MCSE 6082C**, remain the main focus of this thesis, and were both produced with CO_2 as cover gas, hence the "C" at the end. **MCSE 6060** and **MCSE 6082** were produced in the preceding project work [10], in ambient air atmospheres. The reference sample, **RAM 6082**, was produced by a standard ram extrusion process by Kristiansen [63], from the exact same AA6082 extrusion ingot used in this work, and extruded into a Ø10 mm profile.

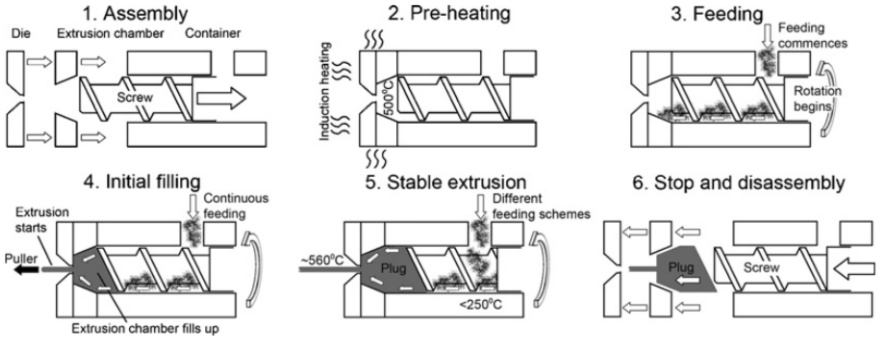

Figure 3.5: Experimental procedures during screw extrusion. From [59].

Temperature during operation was logged in selected positions along the screw extruder. Complete temperature logs for the screw extrusion trials are given in Appendix A, while the average temperatures in the extrusion die are given in Table 3.2. Along with temperature, length of the extruded profiles as a function of time was logged. Linear regression was performed on this data to obtain the extrusion speed, i.e. the derivative of the extruded length. The average values are given in Table 3.2 together with the calculated value for RAM 6082, taken directly from Kristiansen [63]. Notice that the ram extruded profile had a considerably higher extrusion speed, in some cases ∼11 times higher.

Table 3.2: Process parameters for screw extruded profiles and a reference sample from ram extrusion. The two highlighted trials in bold are the main focus of this thesis.

Name	Produced	Alloy	Atmosphere	Temp. [°C][a)]	Extrusion speed [cm/min][b)]
RAM 6082[c)]	Spring 2020	AA6082	Air	∼500	168
MCSE 6060	Fall 2020	AA6060	Air	560	16
MCSE 6082	Fall 2020	AA6082	Air	564	19
MCSE 6060C	Spring 2021	AA6060	CO_2	559	15
MCSE 6082C	Spring 2021	AA6082	CO_2	564	25

[a)] Average temperature in the extrusion die. See Appendix A for complete temperature logs during screw extrusion. [b)] Parameters from screw extrusion trials are based on linear regression of extruded length vs time for the profiles. [c)] Produced by Kristiansen [63].

Upon reaching steady state during screw extrusion, the extruded profiles were collected and dismantling of the screw extruder began. A key part of the thesis was to retrieve the aluminium plug left in the extrusion chamber with minimum damage, schematically shown as Step 6 in Figure 3.5. Due to bonding and frictional forces between the plug (aluminium) and container wall (steel), it proved difficult to separate the aluminium and the steel without some form of deformation of the aluminium. A hammer and chisel were used to separate the two pieces from each other; in some cases several hours were needed to complete the task. The two plugs retrieved from the trials with CO_2 as cover gas are shown in Figure 3.6. These are named **Plug 6060C** and **Plug 6082C**.

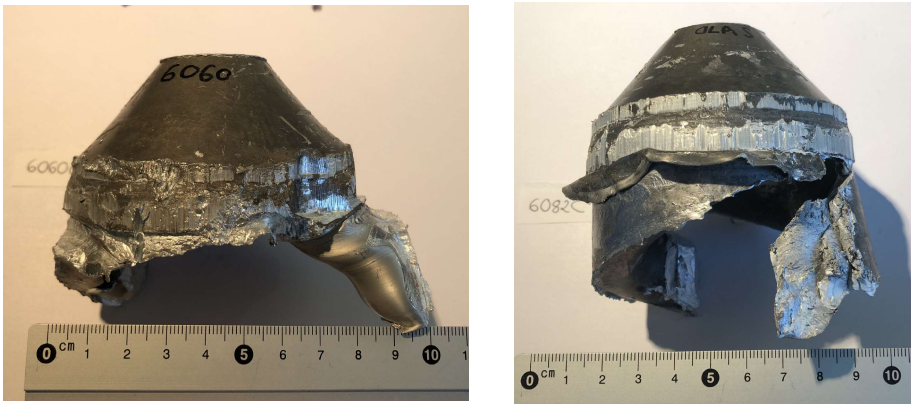

(a) Plug 6060C. **(b)** Plug 6082C.

Figure 3.6: Aluminium plugs retrieved from screw extrusion chamber.

3.3 Cutting of samples from screw plugs

In the following, a method for investigating samples from the two plugs will be presented, including naming and location of samples within the plugs. A complete step-by-step guide of the cutting steps is presented in Appendix B.

Figure 3.7 shows a schematic drawing of the typical aluminium plug after double flight screw extrusion. From the two plugs considered in this thesis (Figure 3.6), six samples were retrieved from each, indicated by numbers 1-6. Samples 1, 2, 3 and 5 are from the same cross-sectional plane, while the plane where Sample 6 is retrieved from lies perpendicular to theirs. For samples along the screw flights, a reference system was created in which a measuring tape was used to find the distance from samples to the reference starting point. As an example, in Figure 3.7 Sample 4 is located 8 cm along Flight A. For this thesis, the flight names "Flight A" and "Flight B" are arbitrary, as only one sample was retrieved along the flight from each plug. In other words, because of symmetry, one sample from Flight A should give similar information as one sample from Flight B.

For all samples, the whole area where the numbers are inscribed in was taken out for inspection. For example, for Sample 1 this means the whole triangle, while for Sample 2 and 3 this means the whole rectangles. For both of the plugs, Plug 6060C and 6082C, Sample 4 was located 8 cm along one of the flights, normal to flow direction, as indicated in Figure 3.7.

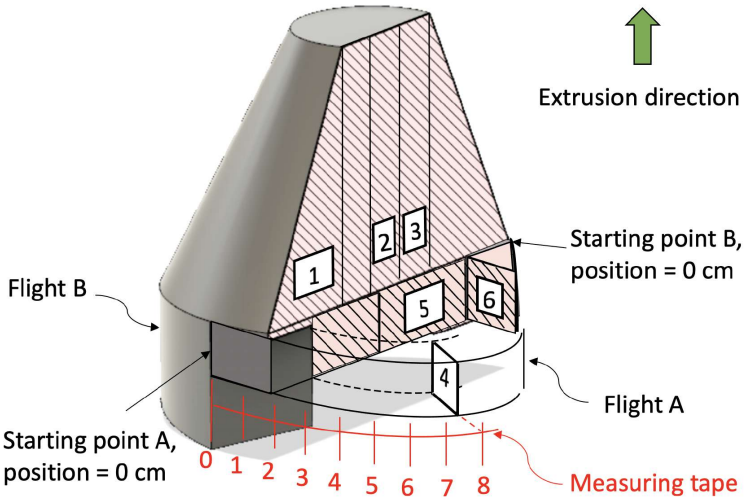

Figure 3.7: Schematic drawing of a typical aluminium plug retrieved after double flight screw extrusion. Samples from different cross sections and locations are indicated and numbered 1-6. Starting point A and Starting point B are reference positions for measuring distance along the screw flights. Sample 4 was located 8 cm along Flight A for both plugs in this thesis. Modified figure from Langelandsvik et al. [64].

3.4 Metallographic procedures

The following section presents sample preparation and techniques for microstructural investigations, including light optical microscopy (LOM), scanning electron microscopy (SEM) and transmission electron microscopy (TEM). An open-source method for quantitative analysis of images from SEM is also presented.

3.4.1 Sample preparation

Samples were investigated from all steps through the value chain of this project, as described in Figure 3.4. For all cutting operations, a Struers Labotom-5 was utilized. Cubic samples were sawed out from the Ø95 mm extrusion ingots, both AA6060 and AA6082, following the schematic drawing shown in Figure 3.8. Feedstock material was investigated without any further processing, prior to thermal cleaning. Samples from extruded material, both screw and ram extruded, were cut according to Figure 3.9 to allow for inspection of both longitudinal and transverse cross sections.

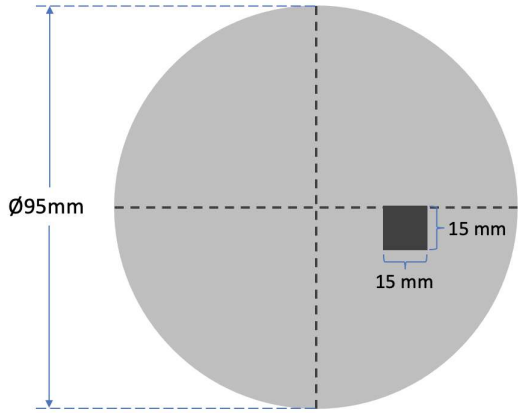

Figure 3.8: Samples from extrusion ingots, transverse cross section.

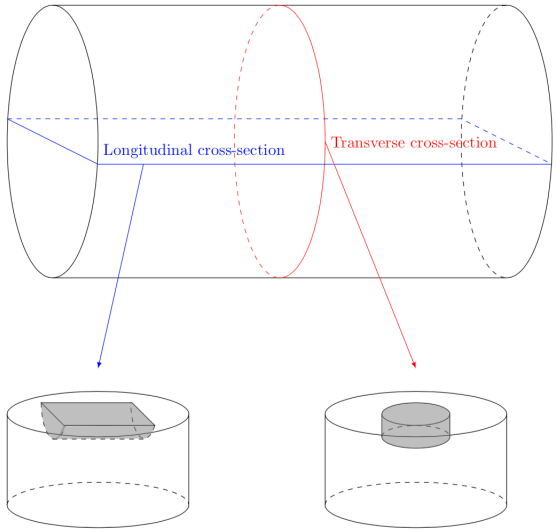

Figure 3.9: Samples from both screw and ram extruded profiles. From [61].

Samples were then cast in Epofix epoxy-resin and polished using a Struers Tegramin-30 automatic polishing machine. Duration, lubricant and surface used for each step are shown in Table 3.3. This procedure was utilized for investigations of particles in both LOM and SEM, including EBSD. Prior to each polishing step the samples were manually cleaned in a VWR Ultrasonic cleaner. Ideally, the samples would have been cleaned in an automatic Struers Lavamin ultrasonic water-cleaner, but it continued to be out-of-order throughout the semester. Although the samples ap-

peared to be scratch-free and have a smooth surface, the manual cleaning machine seemed to have difficulties removing SiO_2-particles from the surface, which most likely were acquired from the polishing suspension OP-S NonDry. This affected the particle analysis of selected samples imaged in SEM, and will be further explained in Section 3.4.3. Samples from various process steps are displayed in Figure 3.10.

Table 3.3: Polishing procedure with indicated duration on each step.

Step	Surface/Roughness	Suspension/Lubricant	Duration
1	SIC FEPA #320	Water	1 min
2	MD-Largo 9 µm	Diaprao All/Lar.	3 min
3	MD-mol 3 µm	Diapro Mol	5 min
4	MD-NAP 1 µm	NAP-R	1 min
5	MD Chem	OP-S NonDry	1 min

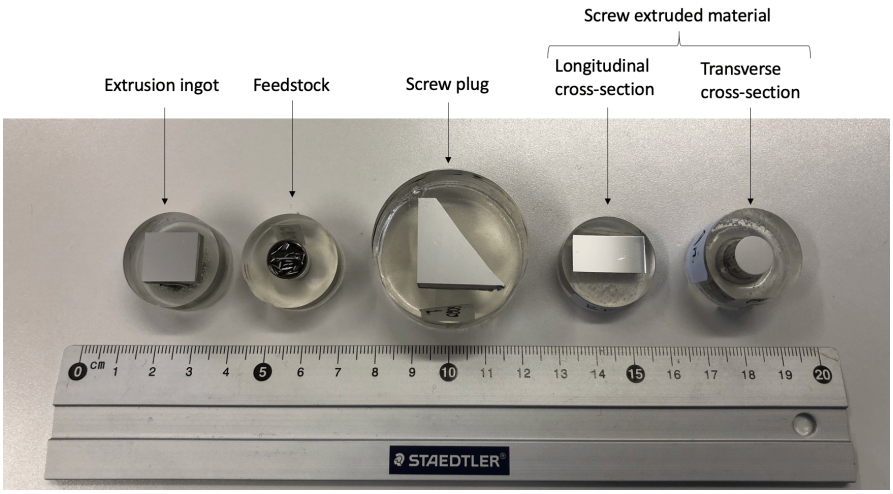

Figure 3.10: Polished samples from various process steps.

Samples investigated for grain structure in LOM were – in addition to the polishing procedure in Table 3.3 – anodized in a 5 % HBF_4 solution for 90 seconds, with an applied voltage of 20 V and a current of 1 A. After anodizing they were immediately rinsed in water.

Samples for investigations in TEM were prepared according to Figure 3.11. Initially, pieces of 1x1 cm and 1 mm thickness from the longitudinal cross section were

taken out. These were then (manually) ground on one side with progressively finer SiC foil: #320, #500, #800, #1200 and #2000. Further, the ground sides were connected to a Plexiglass by a double-sided tape, and the other sides were then ground in a similar manner as the first, to the smallest thicknesses possible. Lastly, samples were lowered in liquid nitrogen for 30-60 seconds and then removed from the Plexiglass with a scalpel. A punch press was used to press out foils of 3 mm diameter.

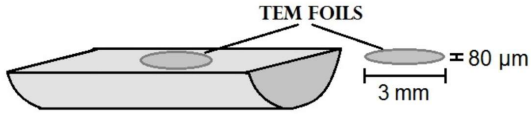

Figure 3.11: Samples for investigations in TEM. Sketch taken from [65].

Successfully ground foils were then electropolished by a Struers TenuPol-5 apparatus. The electrolyte consisted of a 2:1 mixture of methanol and nitric acid, operating at 20 V and -30 °C. Etching continued until the foils had a small hole in the center.

3.4.2 Light optical microscopy

Light optical microscopy images were taken using a Leica MeF4 microscope and post-processed in ProgRes CapturePro, v.2.8.8. Polished samples were imaged in a regular bright-field setting, while anodized samples were imaged with cross-polarized light and a sub-λ-plate. Grain sizes from images in LOM were measured using the linear intercept method.

3.4.3 Scanning electron microscopy

For investigations in SEM, only samples from the screw and ram extruded profiles were considered. Based on availability, both Zeiss Ultra 55 Limited Edition and Zeiss Supra 55 VP FESEM were utilized. All samples were encased in aluminium foil and copper tape to avoid charging, as well as storage in an oven at 65 °C a minimum of 8 hours before imaging in SEM. Settings and analysis methods are given in Table 3.4.

Particle analysis and topography

Primary particles and dispersoids were imaged using back-scatter electrons (BSE) to acquire atomic number contrast (or Z-contrast), which would separate particles, for example containing Fe, Si and Mn, from the aluminium matrix. As was

Table 3.4: Settings for investigations in SEM.

	Particle analysis	Topography	Texture	Fractography
Operation mode	BSE	SE	EBSD	SE
Acceleration voltage	10 kV	10 kV	20 kV	20 kV
Working distance	10 mm	10 mm	∼26 mm	25-30 mm
Current mode	High	High	High	High
Aperture diameter	120 µm	120 µm	300 µm	300 µm
Tilting angle	0°	0°	70°	0°

explained in Section 3.4.1, troubles with cleaning of specimen surfaces after polishing made imaging of MCSE 6060C and MCSE 6082C difficult. Therefore, particle analysis in SEM was primarily performed on samples from the project work, i.e. samples MCSE 6060 and MCSE 6082, on whom the automatic ultrasonic water-cleaner was working. An attempt was made to perform dispersoid analysis on MCSE 6082C, but results are to be considered substandard because of possible contamination of SiO_2 on the surface.

Images with Z-contrast were further analyzed in an open-source software created by PhD student Håkon Wiik Ånes at the Department of Materials Science and Engineering, NTNU. A brief description of the program is given in Appendix C. In short, the program uses a BSE image from SEM as input, converts it into grayscale and 8 bit, marks each particle by separating it from the matrix, and finally acquires particle properties from a binary image. From this analysis, size distribution, number density and area fraction of particles were obtained. In this study, all particles with an equivalent circle diameter of less than 1 µm was counted as a dispersoid, while all particles with an equivalent circle diameter of more than 1 µm was counted as a primary particle.

As a supplement to the images taken with the BSE detector, an image of the same area was taken using the secondary electron (SE) detector. This provided information on the surface topography of the sample, contrary to Z- and orientation contrast from the BSE detector.

Texture

EBSD techniques were used to examine the grain structure of extruded profiles. For this purpose, a Zeiss Ultra microscope was used together with settings listed

in Table 3.4. The indexing step was chosen as 2 µm and diffraction patterns were collected using the software NORDIF, developed by Prof. Jarle Hjelen at NTNU. Results were further post-processed using the software TSL OIM Data Collection 7 and TSL OIM Analysis 7, both developed by EDAX. In OIM, the filter "Grain Dilation" with "Grain Tolerance Angle: 15" was utilized on EBSD data.

Fractography

Fracture surfaces were imaged using the SE detector and settings that allowed for a large depth of field focus. Prior to imaging, the surfaces were rinsed in ethanol and stored in an oven at 65 °C for ∼1 hour. Based on diameter estimates provided by the images, reduction of area at fracture, q, was calculated through the formula given below.

$$q = \frac{A_0 - A_f}{A_0} \tag{3.1}$$

Where A_0 is the original area of the cross section of the specimen and A_f is the area at fracture. The former was obtained by using the measured diameter before tensile testing, while the latter was obtained by measuring the diameter of the fracture surfaces in SEM. RAM 6082 in T6 condition had a non-circular fracture surface and were treated as en ellipse; the area was calculated by the measured semi-major and semi-minor axes through the formula for the area of an ellipse.

3.4.4 Transmission electron microscopy

Samples aged to maximum strength (T6 condition) were investigated in a JEOL JEM-2100 Transmission Electron Microscope. Specimens were tilted to a certain angle in order to align <100> directions perpendicular to the electron beam. Images were then taken at 200 keV in regular bright field mode. Distribution of dispersoids and precipitates were investigated, as well as observations of grain boundaries. An Oxford X-Max 80 SDD EDX detector was used to perform the EDS analysis.

3.5 Mechanical properties

In the following, a short description of the mechanical testing procedures are presented. Similar to investigations in SEM, only samples from screw and ram extruded profiles are considered here.

3.5.1 Hardness testing

Hardness testing followed the procedure suggested by Bilsbak [62], schematically presented in Figure 3.12. Vickers hardness tests were performed on both longitudinal and transverse cross sections of polished samples, using a 1 kg load and dwell time of 10 seconds, with an Innovatest Nova 360 hardness testing machine. 5 indentations were taken for each position along the cross sections.

Figure 3.12: Hardness measurement indents on extruded profiles. From [62].

3.5.2 Tensile testing

Four variations of extruded profiles were considered for the tensile tests. These are given in the list below. All profiles were air cooled after extrusion. Three or four parallels were tensile tested for each heat treatment scheme listed below.

- **As-extruded**: No heat treatment
- **Age hardened**: 185 °C for 6 hours (no prior solutionizing)
- **T6a**: 560 °C for 10 min → water quench → 185 °C for 6 hours
- **T6b**: 560 °C for 10 min → water quench → 165 °C for 20 hours

To obtain T6 condition, samples were solutionized at 560 °C for 10 min in a salt bath and then immediately water quenched. After quenching, the samples were stored for 1 hour at room temperature before age hardening in a Memmert Oil Bath. Two different temperature and time schemes were considered, hence the naming "T6a" and "T6b". In addition, a set of samples were artificially aged without any prior solutionizing. These were named "Age hardened" and are similar to the industrial T5 condition.

Sample geometry of tensile test specimens is given in Figure 3.13. Profiles were machined by Finmekanisk verksted after heat treatment was completed. An MTS 810 Hydraulic tensile testing machine with a maximum load of 100 kN was used with a crosshead speed of 2 mm/min.

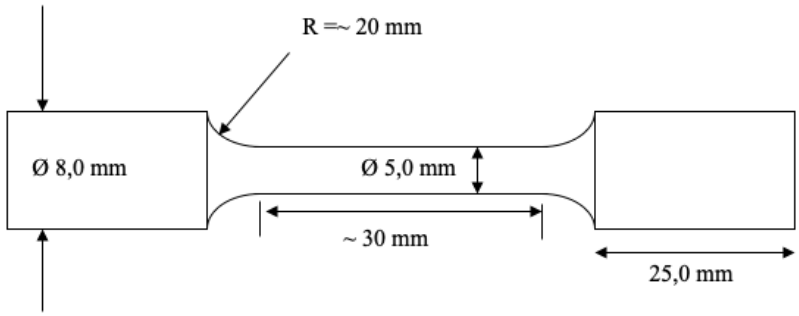

Figure 3.13: Sample geometry of round tensile test specimens.

4 Results

Results are presented in an order similar to that of the value chain in Figure 3.4, i.e. from extrusion ingots to extruded profiles.

4.1 Extrusion ingot

Figure 4.1 displays the microstructures of homogenized extrusion ingots. The average grain size of AA6060 was ∼100 µm, while the average grain size of AA6082 was ∼68 µm. Intermetallic particles were typically found on grain boundaries, and are shown in Figure 4.2. α-AlFeSi- and Mg_2Si-particles are highlighted.

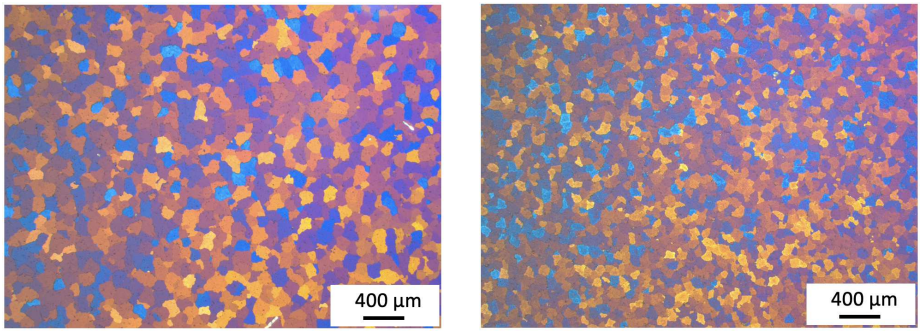

(a) AA6060. Grain size is about 100 µm.

(b) AA6082. Grain size is about 68 µm.

Figure 4.1: Light optical micrograph of extrusion ingot samples under polarized light.

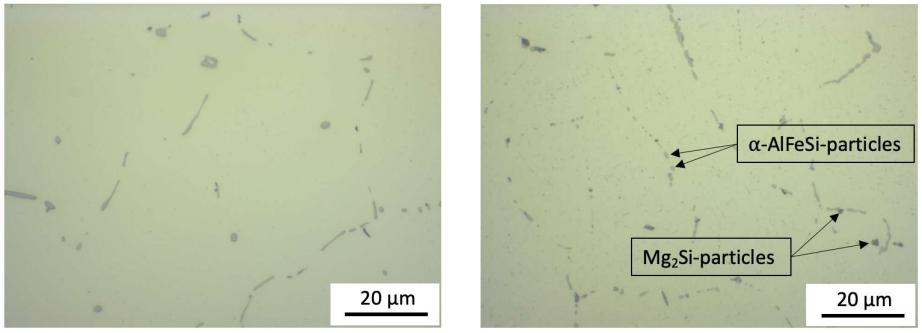

(a) AA6060.

(b) AA6082.

Figure 4.2: Light optical micrograph of extrusion ingot samples under regular bright field imaging.

4.2 Feedstock material

Figure 4.3 shows the microstructures of feedstock material prior to thermal cleaning. Grains were heavily deformed as a result of the machining process, with elongation in machining direction. The smallest measured thickness of a granule was ∼100 µm. Intermetallic particles in feedstock material are shown in Figure 4.4. Particles appear more aligned than in extrusion ingot samples, but morphology and sizes are seemingly similar.

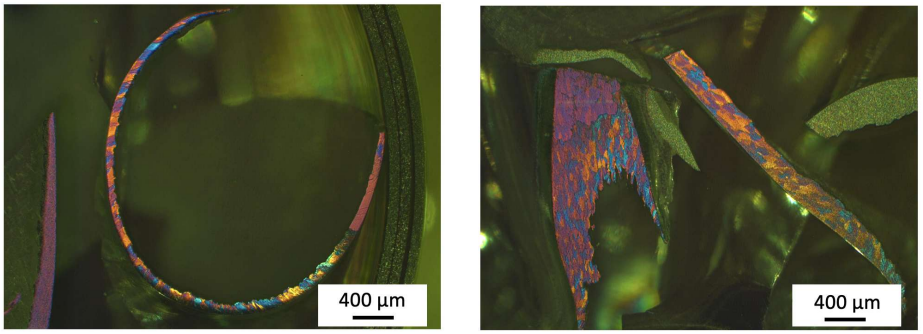

(a) AA6060. **(b)** AA6082.

Figure 4.3: Light optical micrograph of anodized feedstock material prior to thermal cleaning under polarized light. The smallest measured thickness of a granule was about 100 µm.

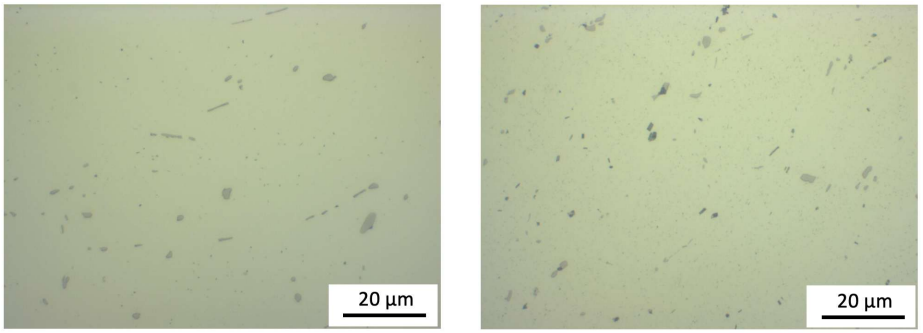

(a) AA6060. **(b)** AA6082.

Figure 4.4: Light optical micrograph of feedstock material prior to thermal cleaning under regular bright field imaging.

4.3 Aluminium plug

In the following section, images taken of samples from aluminium plugs are presented. As the grain structure of Plug 6082C revealed little information (mostly prolonged fibers and unclear images), a large majority of the images under polarized light are from Plug 6060C. The reader is referred to Figure 3.7 for a reference system for sample location in plugs.

4.3.1 Microstructure

Figures 4.5–4.10 display microstructures in all six samples from Plug 6060C. In each figure there are three supporting subfigures with higher magnification and their own scale bar. Above the images, sketches of the plug are drawn together with red markers to indicate where the samples are taken from.

The evolution of the microstructure close to the extrusion die is seemingly similar across samples (Figures 4.5– 4.7). A zone of equiaxed grains can be seen close to the vertical center line (subfigures labeled (c)), while grains are more elongated along the material flow direction (Figure 4.5b). Also, closest to the extrusion die, a zone of coarse elongated grains can be seen, most notably in subfigures (a) in both Figures 4.5 and 4.7.

The microstructure farther away from the extrusion die displays a more chaotic flow pattern (Figures 4.8–4.10). For example, in Sample 5 there are zones of small and large grain sizes, which indicate a layered structure of material feeding (Figure 4.9b). Sample 5 is the zone where material is transported from the screw tip and farther down the extrusion chamber, which can be seen by the material flow from bottom right to top left corner.

Selected images from Plug 6082C are shown in Figure 4.11. For these samples, the grain structure is much less prominent and consists mostly of a fibrous microstructure. Also, several smaller cracks are visible close to the extrusion die in Figure 4.11, Sample 1, upper left corner.

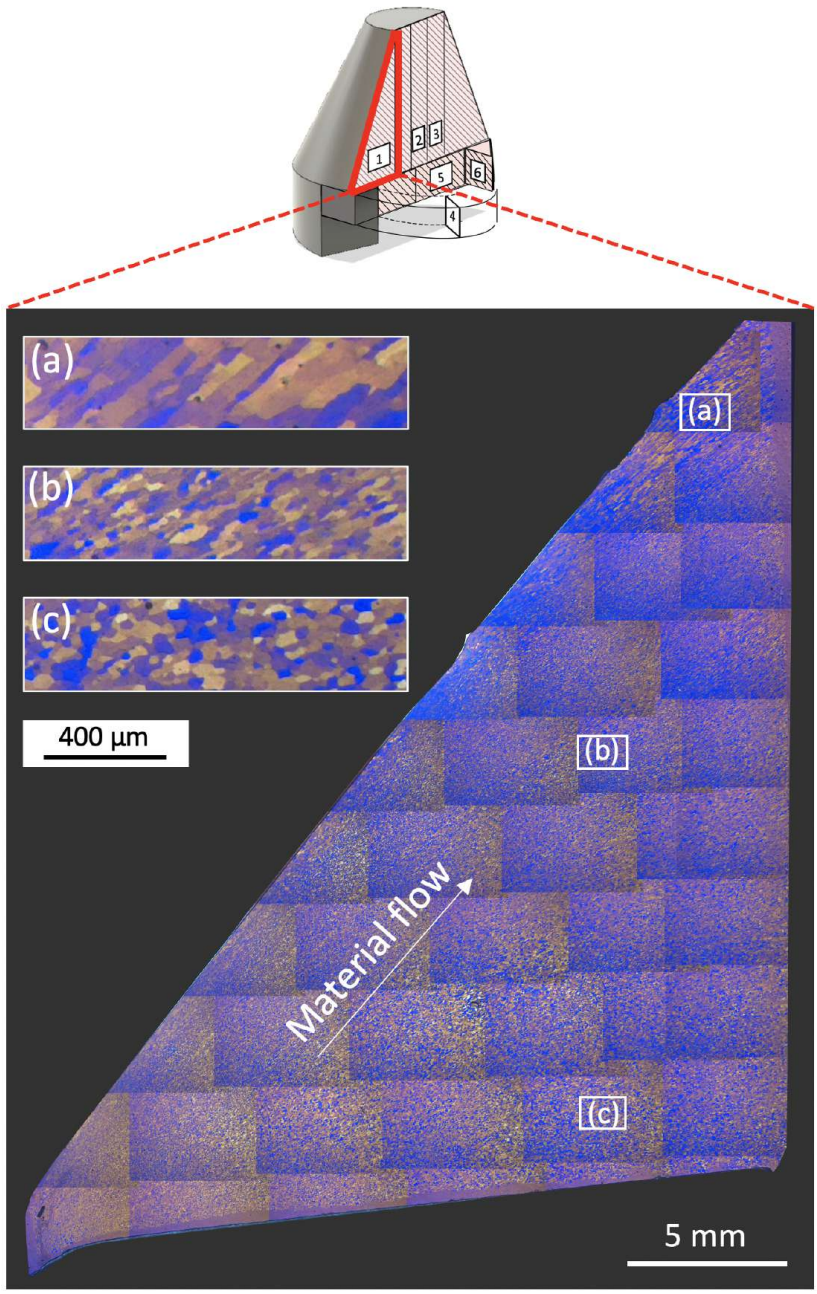

Figure 4.5: Light optical micrographs of Sample 1 from Plug 6060C under polarized light. Close-ups of selected areas of interest are included in image boxes labeled (a), (b) and (c). The smallest scale bar (400 µm) refers to those images. Average grain size in (c) is about 42 µm.

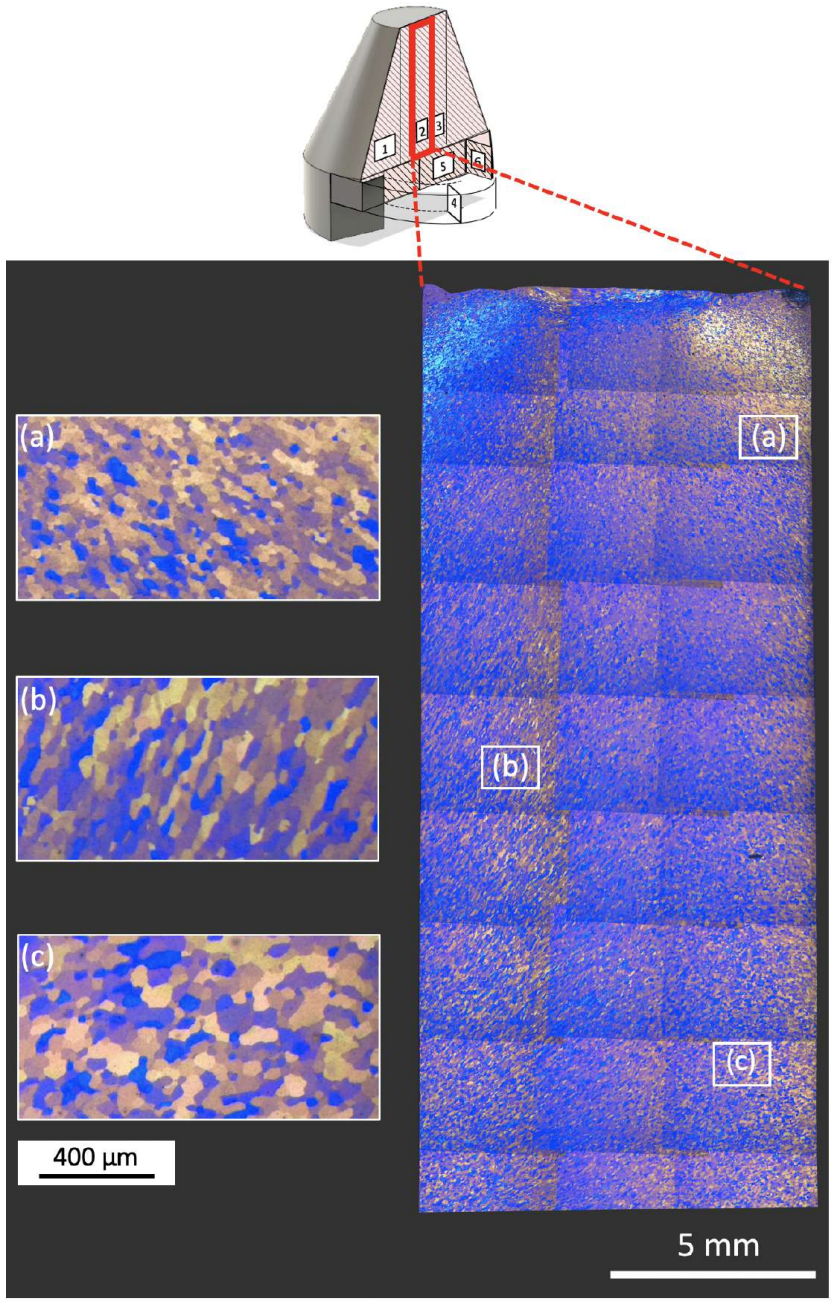

Figure 4.6: Light optical micrographs of Sample 2 from Plug 6060C under polarized light. Close-ups of selected areas of interest are included in image boxes labeled (a), (b) and (c). The smallest scale bar (400 µm) refers to those images. Average grain size in (c) is about 47 µm.

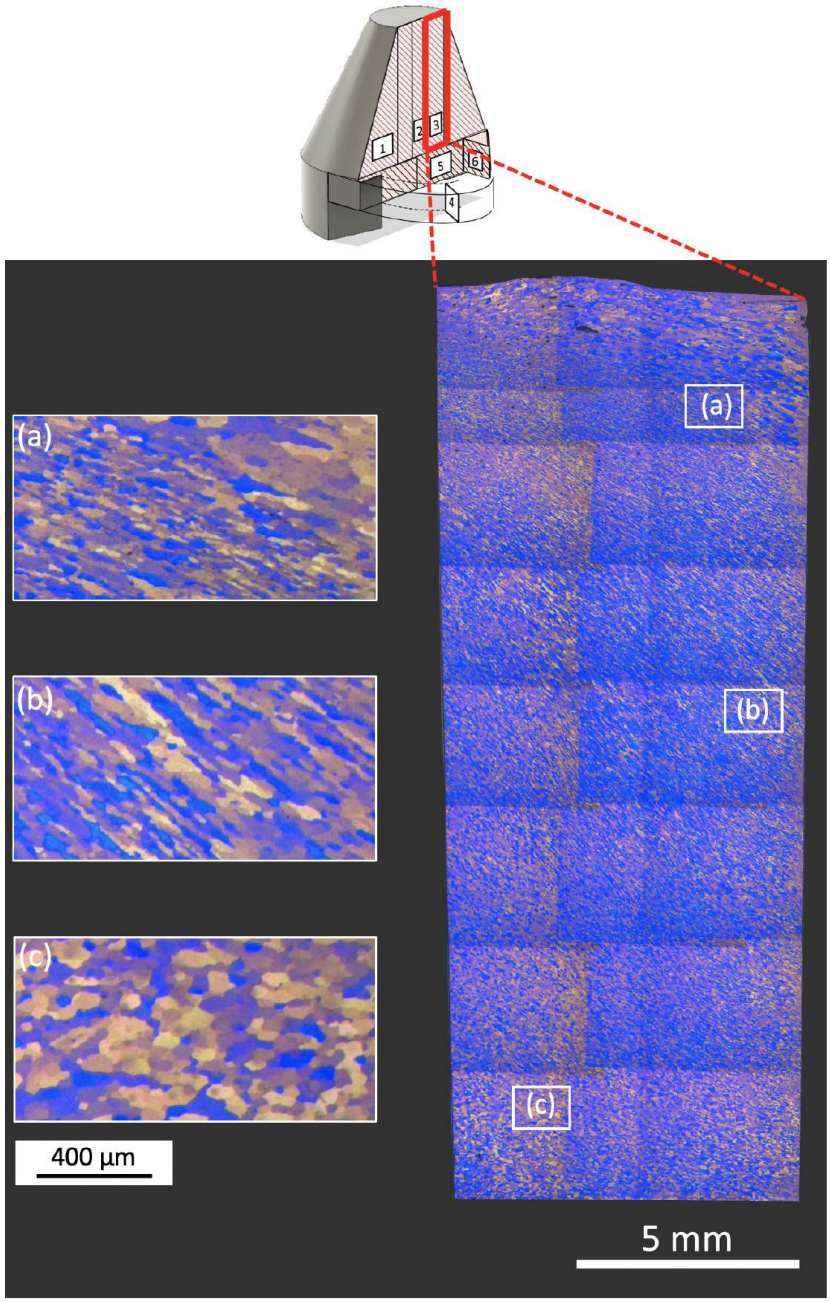

Figure 4.7: Light optical micrographs of Sample 3 from Plug 6060C under polarized light. Close-ups of selected areas of interest are included in image boxes labeled (a), (b) and (c). The smallest scale bar (400 µm) refers to those images. Average grain size in (c) is about 53 µm.

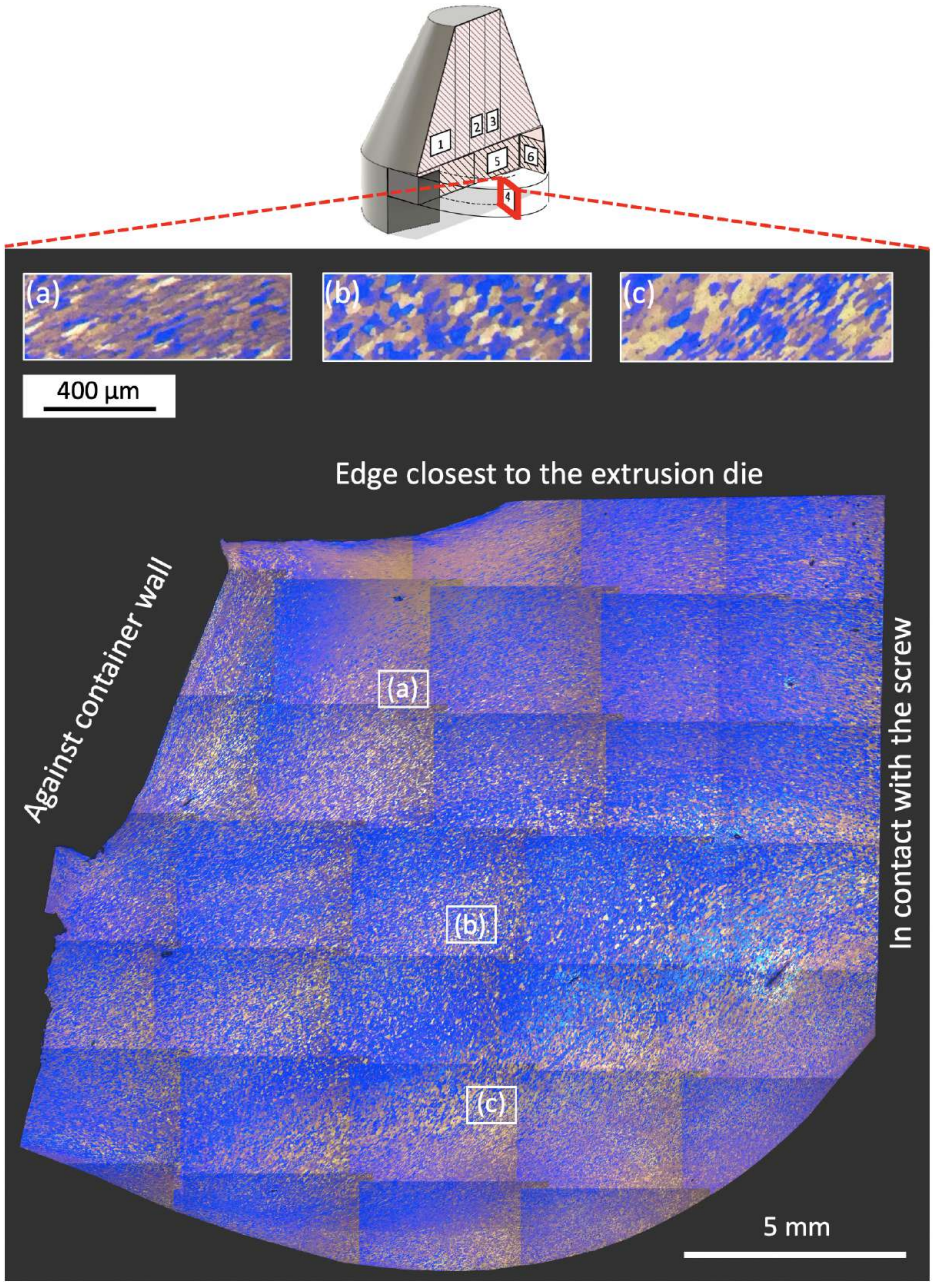

Figure 4.8: Light optical micrographs of Sample 4 from Plug 6060C under polarized light. Close-ups of selected areas of interest are included in image boxes labeled (a), (b) and (c). The smallest scale bar (400 µm) refers to those images. Micrographs are taken normal to the material flow along one of the screw flights. Orientation of the sample is indicated by locating the container wall, extrusion die and screw.

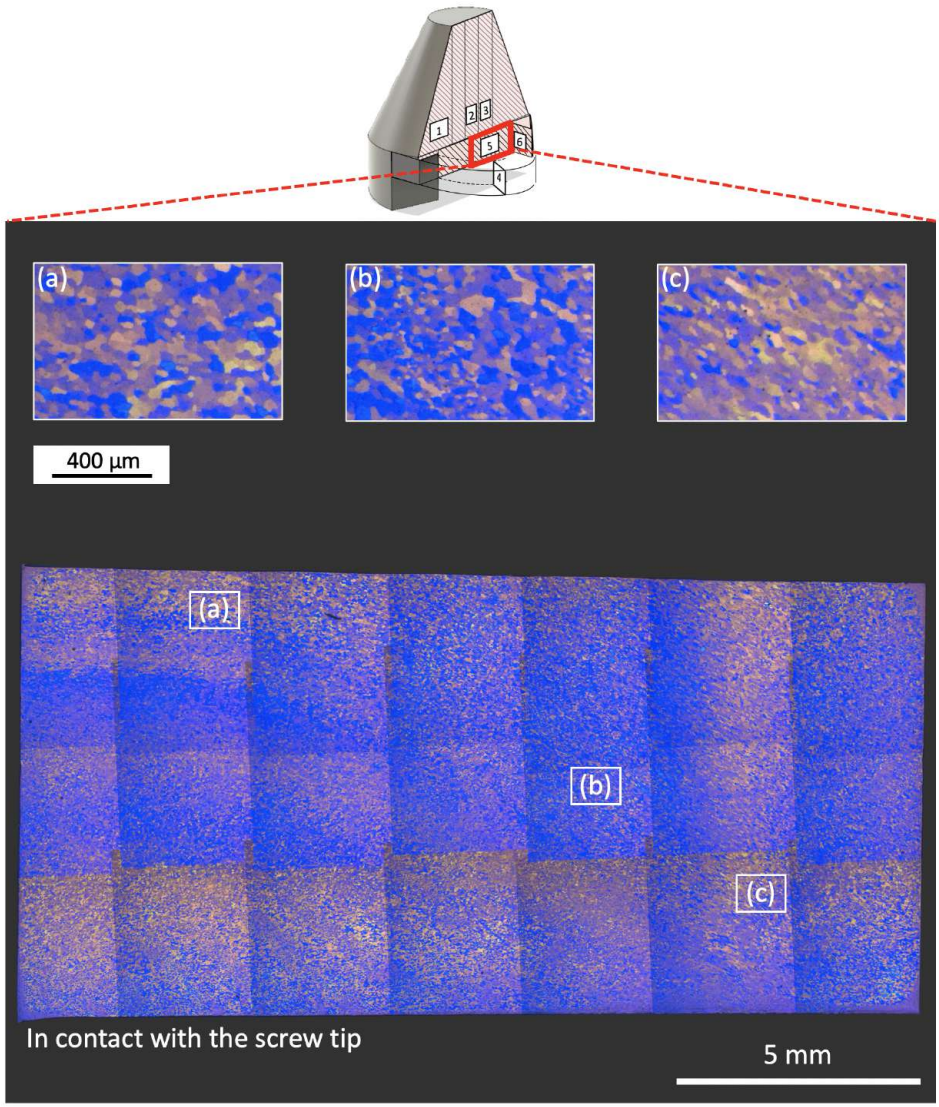

Figure 4.9: Light optical micrographs of Sample 5 from Plug 6060C under polarized light. Close-ups of selected areas of interest are included in image boxes labeled (a), (b) and (c). The smallest scale bar (400 µm) refers to those images.

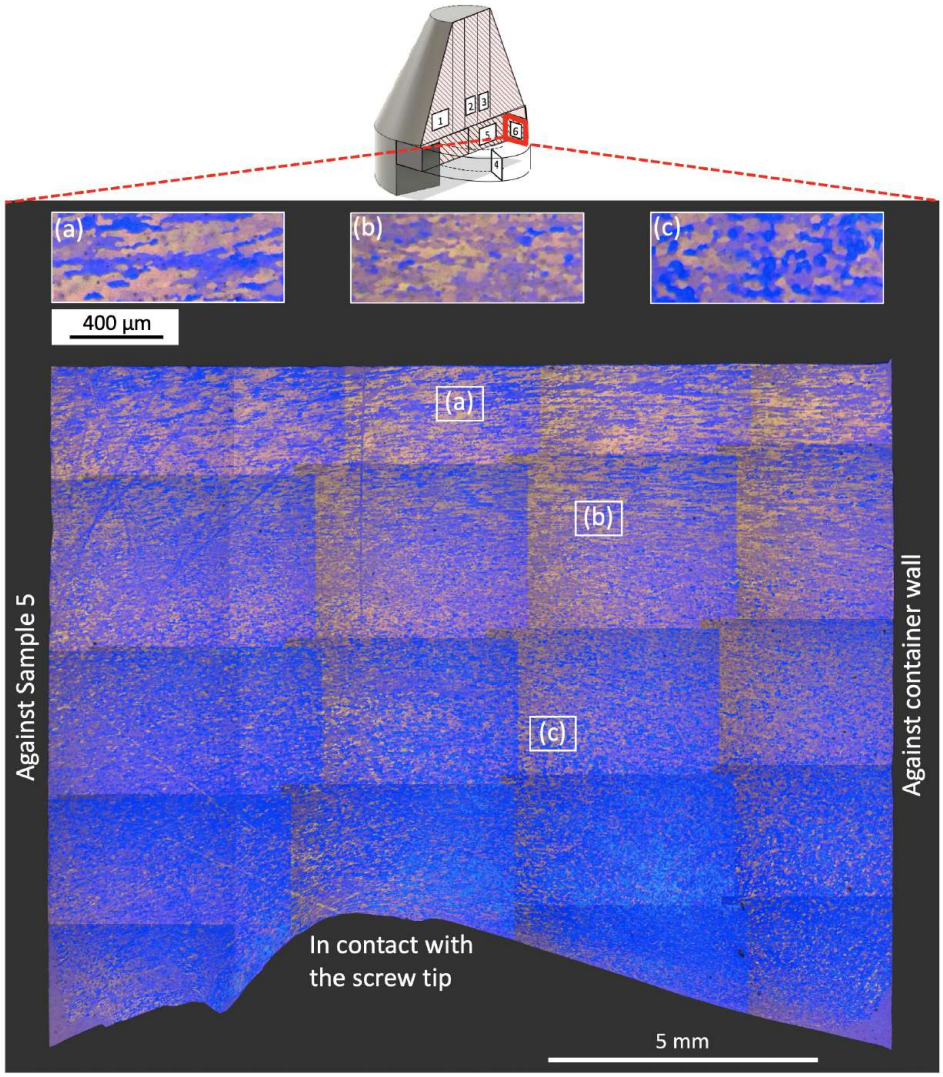

Figure 4.10: Light optical micrographs of Sample 6 from Plug 6060C under polarized light. Close-ups of selected areas of interest are included in image boxes labeled (a), (b) and (c). The smallest scale bar (400 µm) refers to those images.

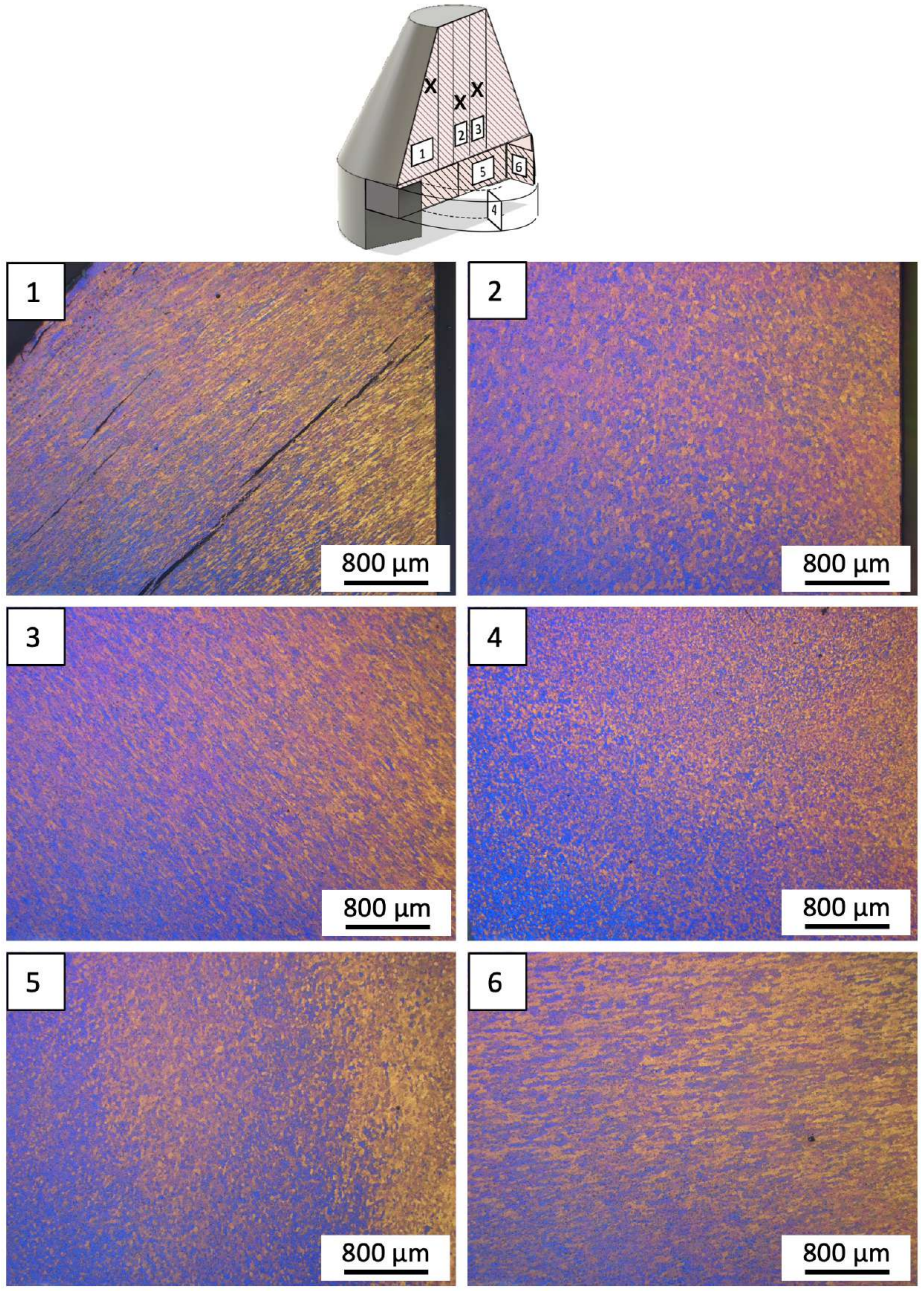

Figure 4.11: Light optical micrographs of selected areas from Plug 6082C under polarized light. Black crosses in the sketch above indicate (approximately) where images in samples 1, 2 and 3 are from. Images numbered 4, 5 and 6 are from the middle of each respective sample.

4.3.2 Intermetallic particles

Images displaying the evolution of intermetallic particles through the screw extruder are shown for Plug 6060C in Figure 4.12, and for Plug 6082C in Figure 4.13.

For both trials there seems to be a homogeneous distribution of particles, with a weak form of alignment in the screw extrusion direction. This is most visible in Plug 6060C (Figure 4.12, Sample 1), where some zones are depleted of particles and material flow direction is seen from bottom left to upper right corner. AlFeSi-particles and Mg_2Si are visible in both plugs, but with a seemingly higher particle density in Plug 6082C (Figure 4.13), as expected from the alloying contents. Mg_2Si is typically seen precipitated on larger AlFeSi-particles.

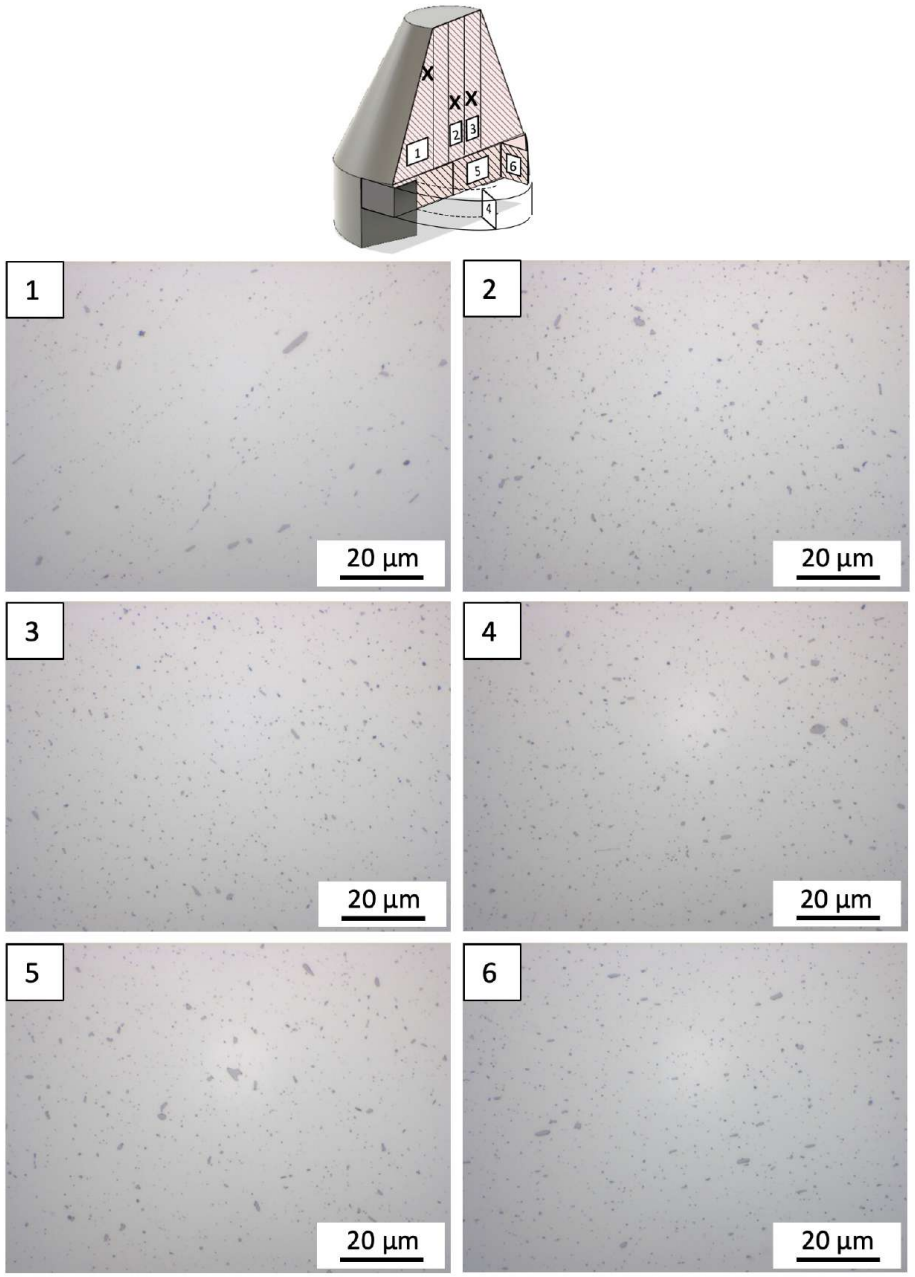

Figure 4.12: Light optical micrographs of selected areas from Plug 6060C under regular bright field imaging. Black crosses in the sketch above indicate (approximately) where images in samples 1, 2 and 3 are from. Images numbered 4, 5 and 6 are from the middle of each respective sample.

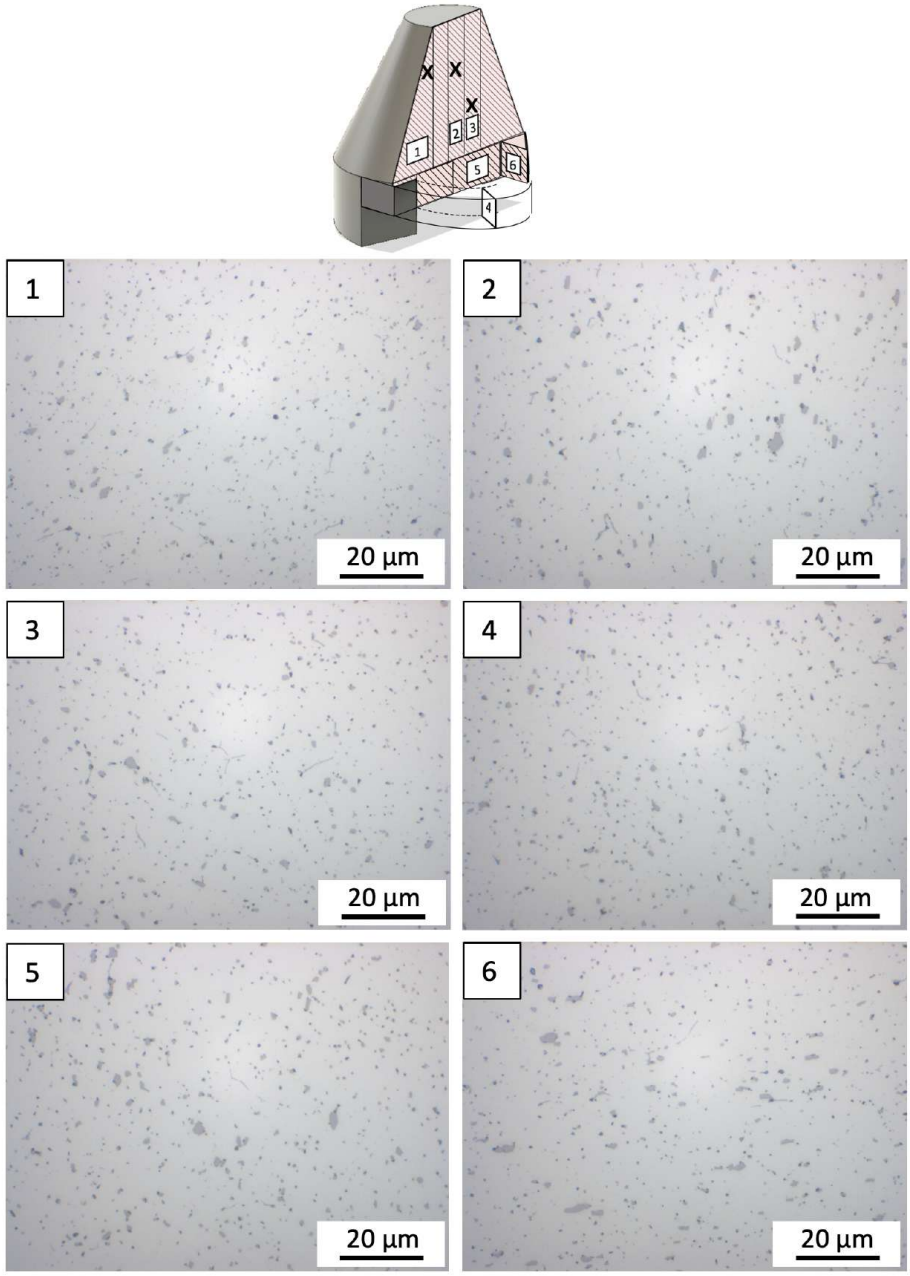

Figure 4.13: Light optical micrographs of selected areas from Plug 6082C under regular bright field imaging. Black crosses in the sketch above indicate (approximately) where images in samples 1, 2 and 3 are from. Images numbered 4, 5 and 6 are from the middle of each respective sample.

4.4 Extruded profiles

In the following section, analysis of the extruded profiles will be covered. This includes visual inspection, microstructure and particle analysis.

4.4.1 Visual inspection

Figure 4.14 shows the surface appearance of extruded samples. Die lines were present in extrusion direction for both MCSE 6060C and MCSE 6082C, while RAM 6082 was smooth with no visible defects.

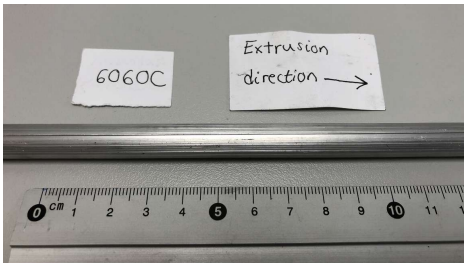

(a) MCSE 6060C.

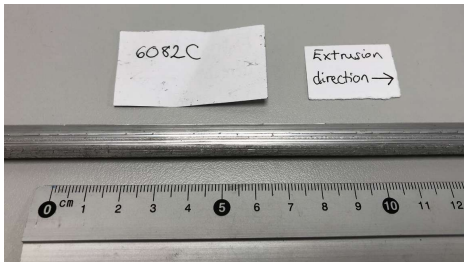

(b) MCSE 6082C.

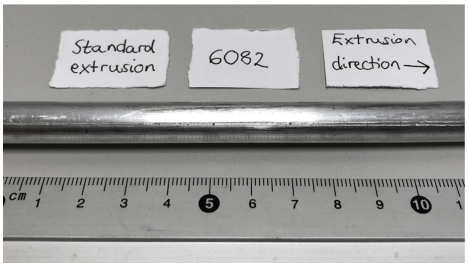

(c) RAM 6082.

Figure 4.14: Visual inspection of extruded profiles in as-extruded condition.

4.4.2 Microstructure

A comparison between screw extruded profiles produced with or without CO_2 as cover gas is displayed in Figure 4.15. The two trials performed in ambient air atmosphere are shown in Figures 4.15a and 4.15c, while the two trials performed with CO_2 are shown in Figures 4.15b and 4.15d. The images show the transverse cross section of each screw extruded trial in as-extruded condition. Porosity is visible as dark spots in each image.

There seems to be no visible effect on the two trials with 6060, i.e. comparing MCSE 6060 and MCSE 6060C. However, for the two trials with 6082, a decrease

in porosity is observed. In addition, MCSE 6060C and MCSE 6082C have a more irregular shape.

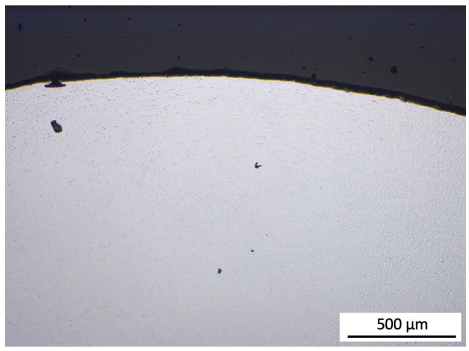

(a) MCSE 6060.

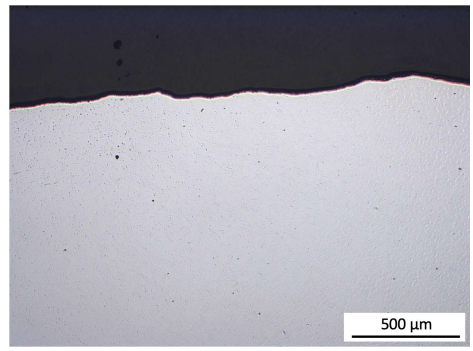

(b) MCSE 6060C.

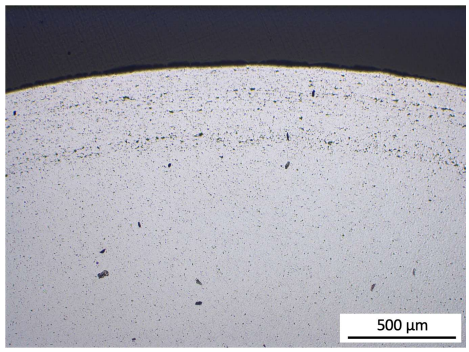

(c) MCSE 6082.

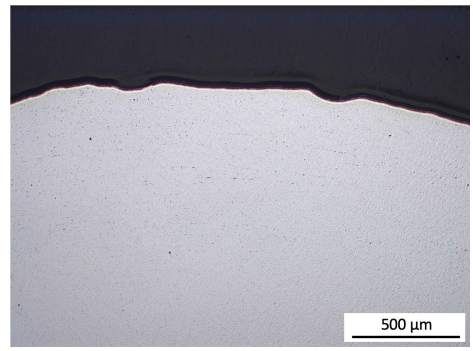

(d) MCSE 6082C.

Figure 4.15: Light optical micrographs of transverse cross section samples from screw extruded profiles, regular bright field imaging; (a) and (c) in ambient air atmosphere, (b) and (d) with CO_2 as cover gas. A decrease in porosity may be observed for the 6082 trials, comparing (c) to (d). Also notice the irregular shapes in (b) and (d).

Figure 4.16 displays the grain structure of extruded profiles in as-extruded condition. MCSE 6060C has a structure of prolonged grains with a thin recrystallized outer layer. MCSE 6082C is fibrous throughout the whole cross section, while RAM 6082 is fibrous with a coarse recrystallized layer of ∼900 µm thickness.

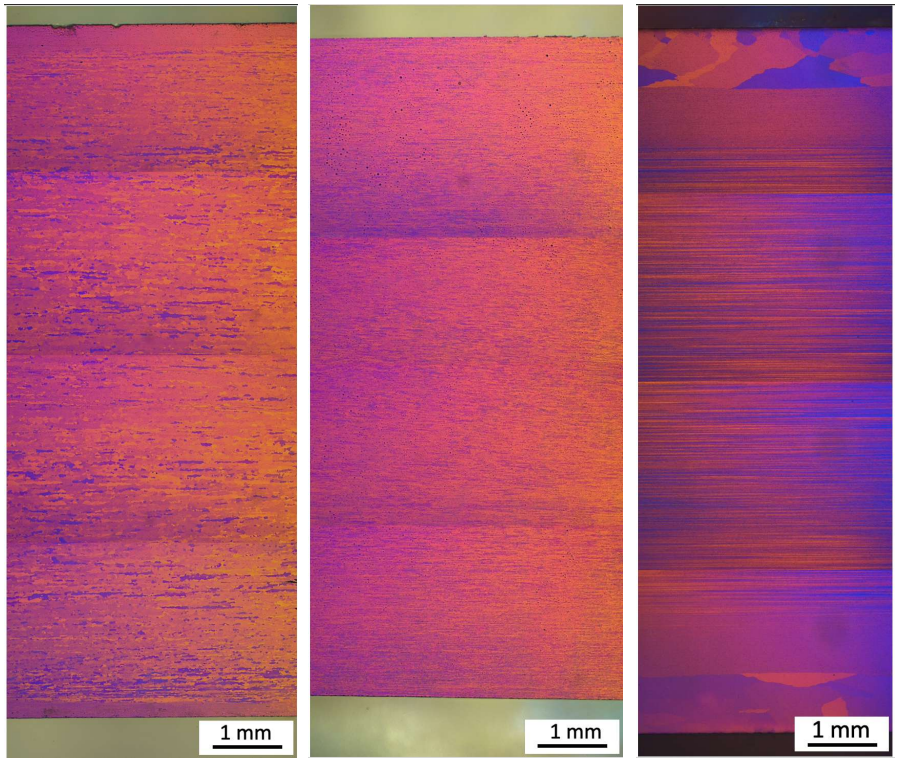

(a) MCSE 6060C. **(b)** MCSE 6082C. **(c)** RAM 6082.

Figure 4.16: Light optical microcgraphs showing microstructure of longitudinal cross section, as-extruded condition. The recrystallized layer in (c) is about 900 µm. Extrusion direction is horizontally to the right in each image. The profile in (b) appears thinner than the two other due to the longitudinal cross section being slightly off-center.

EBSD scans of longitudinal cross sections are shown in Figures 4.17–4.19. A supportive light optical micrograph is presented along with the EBSD scans to show where the scans are performed. Low angle grain boundaries (LAGB) and high angle grain boundaries (HAGB) are coloured with gray and black lines, respectively. In all three scans there seem to be two dominant orientations: the <111> and <001> fibers. The distribution of LAGB and HAGB is also approximately similar for the three samples, with a slightly higher fraction of HAGBs in MCSE 6082C.

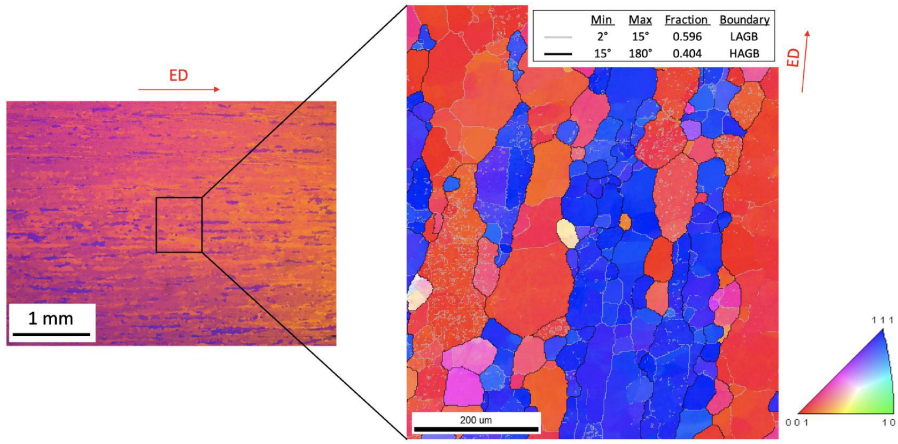

Figure 4.17: EBSD grain mapping of MCSE 6060C, longitudinal cross section in as-extruded condition. Colours indicate crystallographic orientation of grains in extrusion direction. The left micrograph is from an anodized sample in light optical microscopy, whereas the right one is from a polished sample in EBSD. Low angle grain boundaries (LAGB) are displayed in a light gray colour, high angle grain boundaries (HAGB) in a black colour.

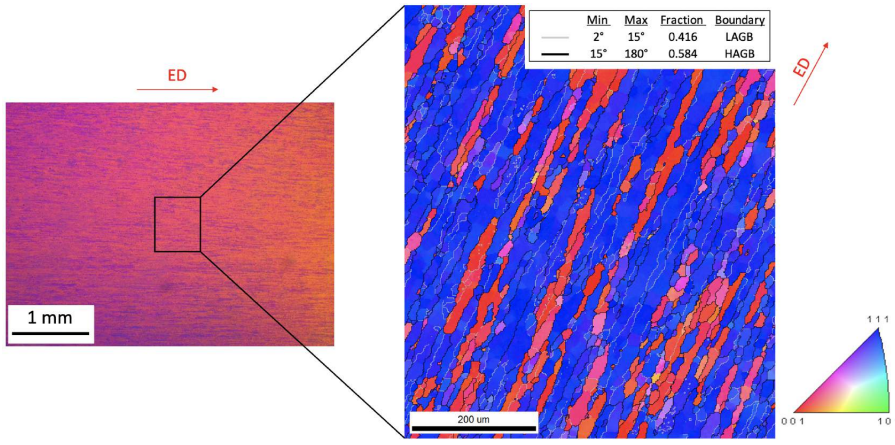

Figure 4.18: EBSD grain mapping of MCSE 6082C. Orientations and grain boundary colouring is similar to that of Figure 4.17.

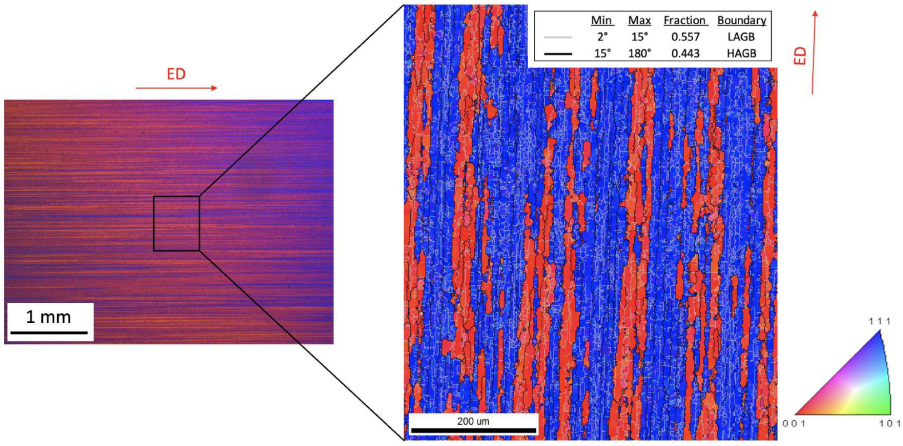

Figure 4.19: EBSD grain mapping of RAM 6082. Orientations and grain boundary colouring is similar to that of Figure 4.17.

Grain size diameter distributions for the three samples are shown in Figures 4.20–4.22. Scan area is similar to the three previous figures. Colours have no physical meaning with respect to orientation, only to enhance grain contrast. Grain sizes for MCSE 6060C are severely right-shifted compared to MCSE 6082C and RAM 6082, as expected by the apparent larger grains. For MCSE 6082C and RAM 6082 however, the distributions are seemingly multimodal.

In MCSE 6060C the structure seems to be partly recrystallized with grains having a diameter of 30–70 µm, together with coarse elongated grains in extrusion direction. The fiber structure is more prominent in MCSE 6082C, but also some regions of sub-grains are visible, having a diameter of about 4–10 µm. For RAM 6082, the fibrous un-recrystallized grains are even more dominant, in addition to sub-grains that are more numerous and shifted towards the left, but still within the range 4–10 µm.

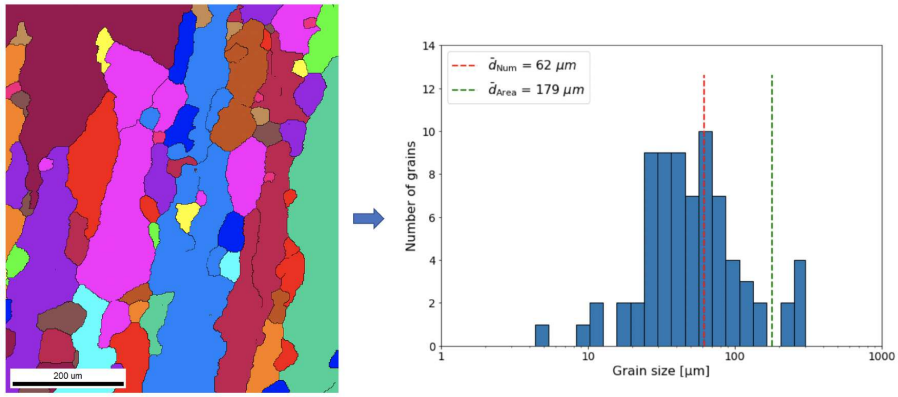

Figure 4.20: EBSD grain mapping of MCSE 6060C, identical scan area as Figure 4.17. Colours have no physical meaning, only to enhance grain contrast. Grain size diameter distribution is shown to the right, where threshold for a grain was set to >15° misorientation angle. Both numerical and area weighted averages are indicated. A total of 74 grains counted.

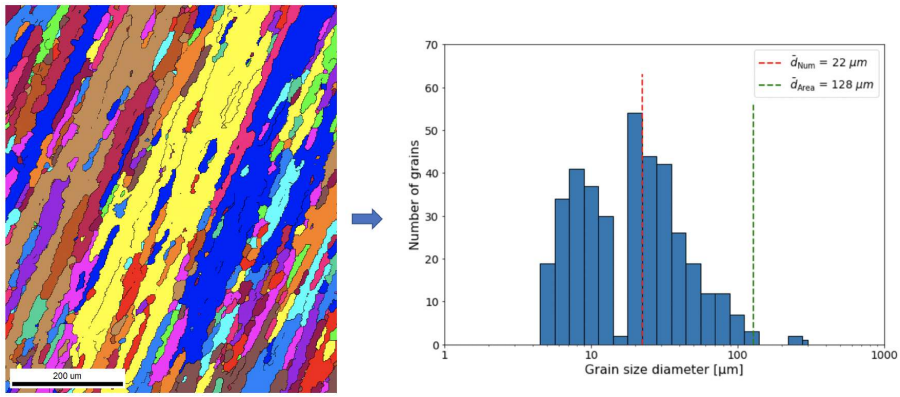

Figure 4.21: EBSD grain mapping of MCSE 6082C, identical scan area as Figure 4.18. Refer to Figure 4.20 for a complete description of the figure. A total of 384 grains counted.

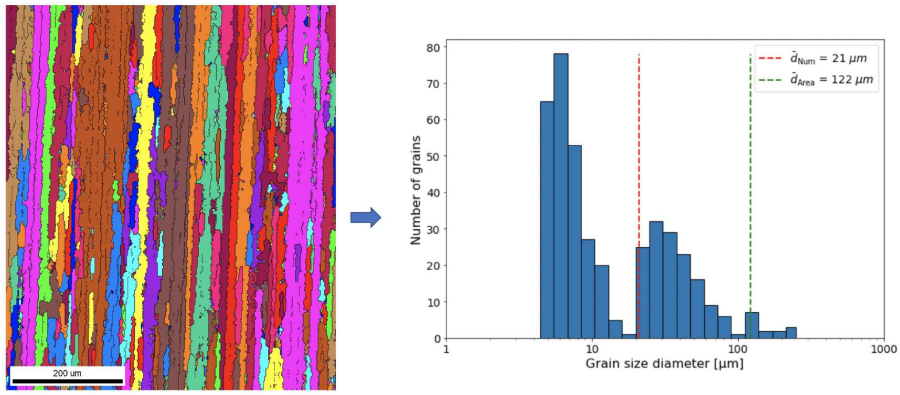

Figure 4.22: EBSD grain mapping of RAM 6082, identical scan area as Figure 4.19. Refer to Figure 4.20 for a complete description of the figure. A total of 404 grains counted.

Pole figures and inverse pole figures from the image scans by EBSD are presented in Figure 4.23. Pole figures projected in [001] and [111] directions strengthen the observations made in Figures 4.17–4.19, with indications of strong <001> and <111> fiber texture. This is also confirmed by the inverse pole figures. The right-hand scale bars, showing texture intensity, indicate that the texture was weaker in MCSE 6060C compared to MCSE 6082C and RAM 6082.

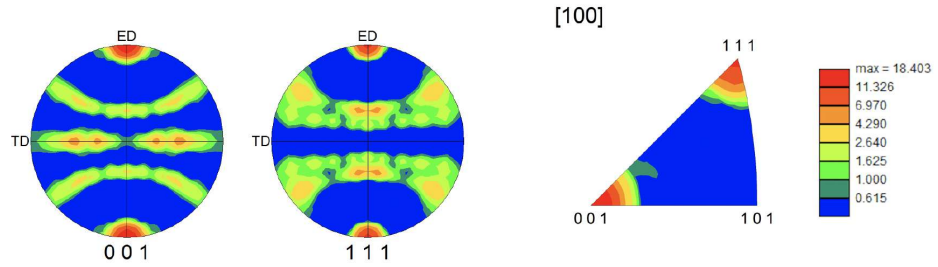

(a) MCSE 6060C. Similar scan area as in Figure 4.17.

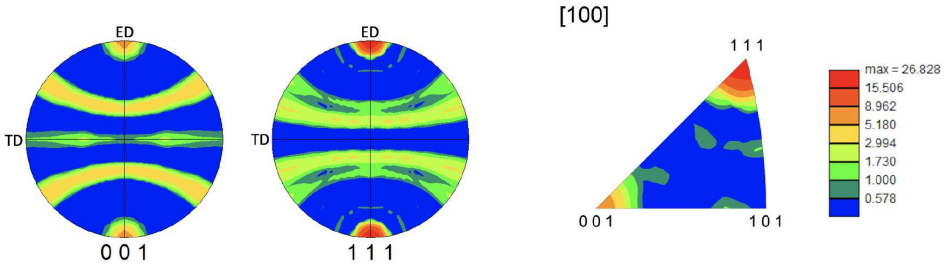

(b) MCSE 6082C. Similar scan area as in Figure 4.18.

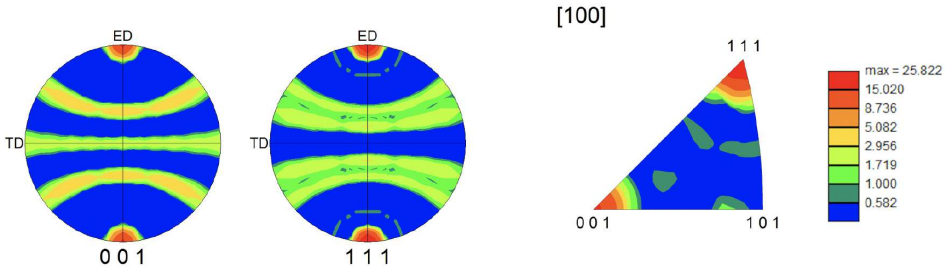

(c) RAM 6082. Similar scan area as in Figure 4.19.

Figure 4.23: Pole figures projected in [001] and [111] direction (left) and inverse pole figures (right). Texture intensity is coloured by a scale bar to the right of each figure, with units "times random orientation".

4.4.3 Particle analysis

Intermetallic particles imaged under regular bright field settings in light optical microscopy are shown in Figure 4.24. Primary particles seem to be more evenly dispersed and less aligned in the screw extrusion process, comparing MCSE 6082C to RAM 6082. A lower number density of particles in MCSE 6060C is observed, as expected by the alloy class.

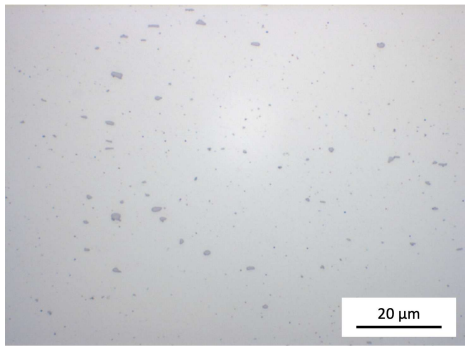

(a) MCSE 6060C.

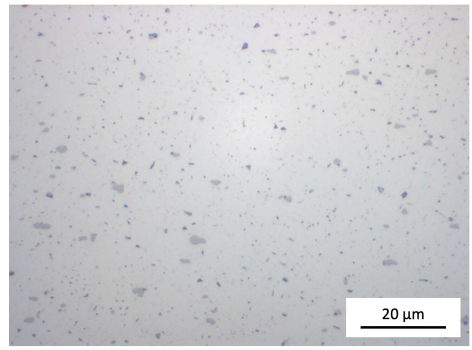

(b) MCSE 6082C.

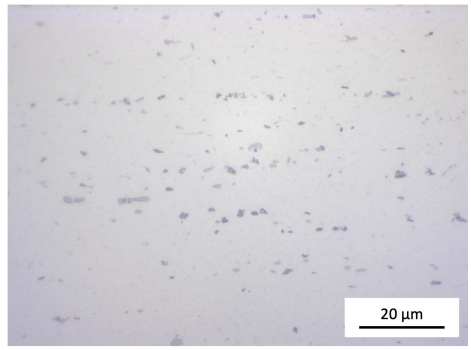

(c) RAM 6082.

Figure 4.24: Light optical micrographs of samples from the center of longitudinal cross section. As-extruded profiles, regular bright field imaging. Morphology and distribution of intermetallic particles are shown. Extrusion direction is horizontally to the right in each image.

Figure 4.25 shows a representative selection of dispersoid images, using both SE and BSE detector. As there are no dispersoids in the 6060 alloy class, MCSE 6060C is not included. Instead, MCSE 6082 (screw extrusion trial with ambient air atmosphere) is included together with MCSE 6082C (trial with CO_2 as cover gas). However, the images taken of MCSE 6082C should be considered suboptimal due to difficulties with cleaning, as explained in Section 3.4.3. In images with the BSE detector, dispersoids are visible as small white dots.

By comparing the three samples it is evident that the number density of dispersoids was higher in RAM 6082. Also, similar to the observations made in LOM, particles (and dispersoids) appear more aligned in the ram extruded sample. Some of the contamination (in the form of small SiO_2-particles) is indicated by red circles in Figure 4.25c, and should be kept in mind when inspecting the BSE image of MCSE 6082C.

Figure 4.26 shows the size distribution of dispersoids. Notice the relative difference in frequency, given by the y-axes. Visual observations of the dispersoids are confirmed by the histograms, as the plot for RAM 6082 is left-shifted towards smaller and more numerous dispersoids.

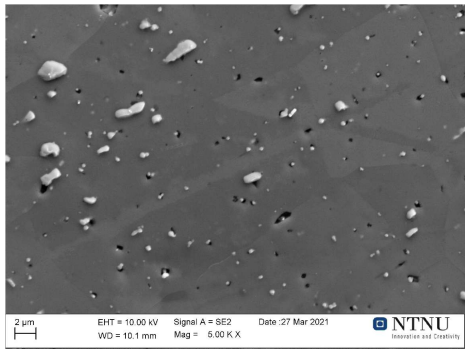

(a) MCSE 6082 SE image.

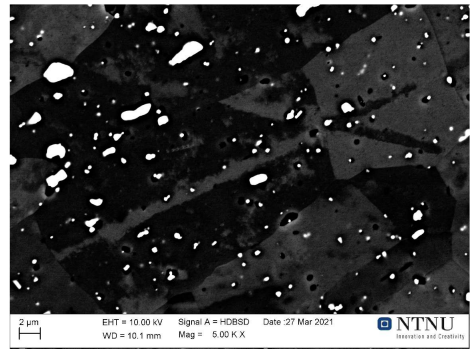

(b) MCSE 6082 BSE image.

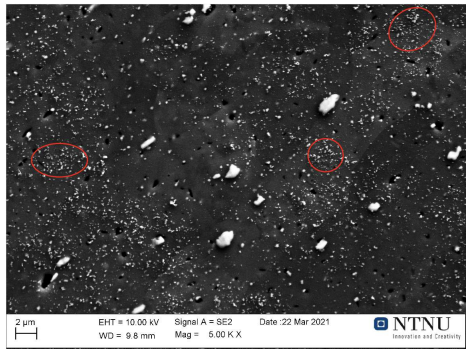

(c) MCSE 6082C SE image.

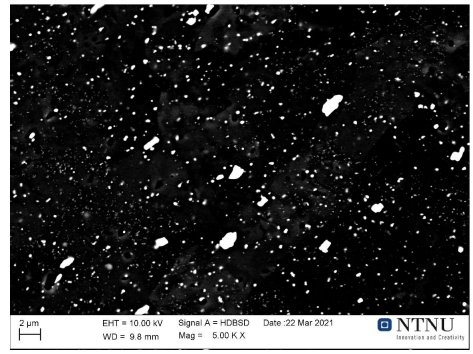

(d) MCSE 6082C BSE image.

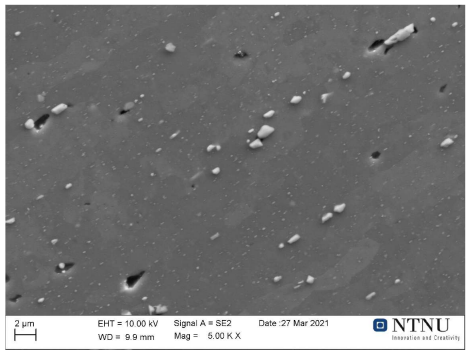

(e) RAM 6082 SE image.

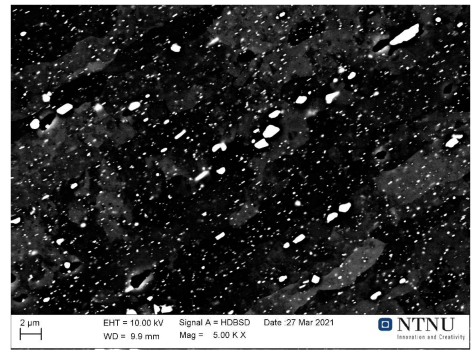

(f) RAM 6082 BSE image.

Figure 4.25: A representative selection of dispersoid images taken with SE detector (left column) and with BSE detector (right column). In (c) red circles indicate areas of SiO_2 contamination from last polishing step. The subfigures are horizontally coupled such that two images in the same row are from the same area. For example, (a) and (b) are two images from the same area, only difference being the choice of detector.

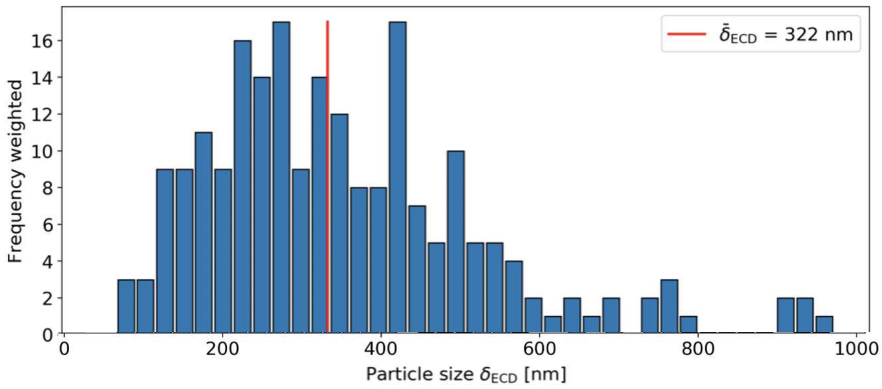

(a) MCSE 6082.

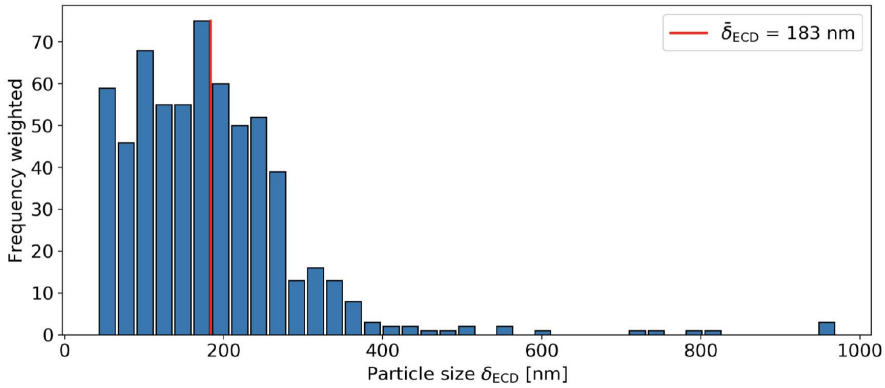

(b) MCSE 6082C.

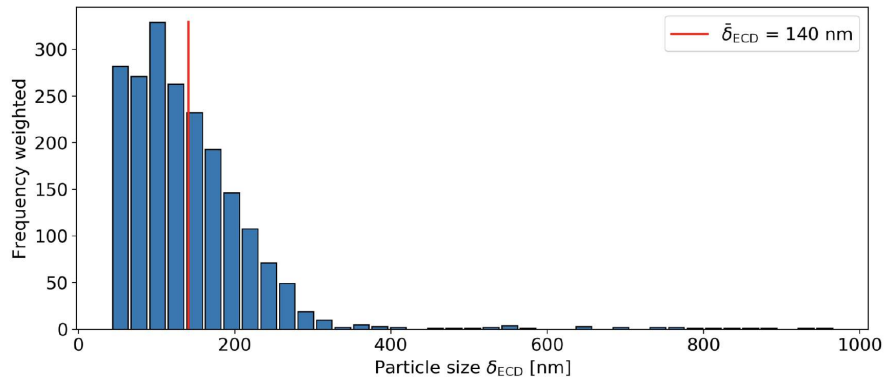

(c) RAM 6082.

Figure 4.26: Size distribution of dispersoids. The three distributions presented here are based on the three respective BSE images in Figure 4.25. Mean equivalent circle diameter is indicated in each subfigure.

Results from both primary particles and dispersoids are presented Figures 4.27–4.29. For the analyses of primary particles, MCSE 6060 and MCSE 6082 (both produced in ambient air atmosphere) are presented, due to the difficulties with cleaning of MCSE 6060C and MCSE 6082C (Section 3.4.3).

Figure 4.27 shows the average size of primary particles and dispersoids. Standard deviations are high because of the Weibull distribution of particle sizes, as shown in Figure 4.26. Primary particles seem to be of even sizes across samples, while dispersoids seem to be smaller in RAM 6082 compared to MCSE 6082 and MCSE 6082C.

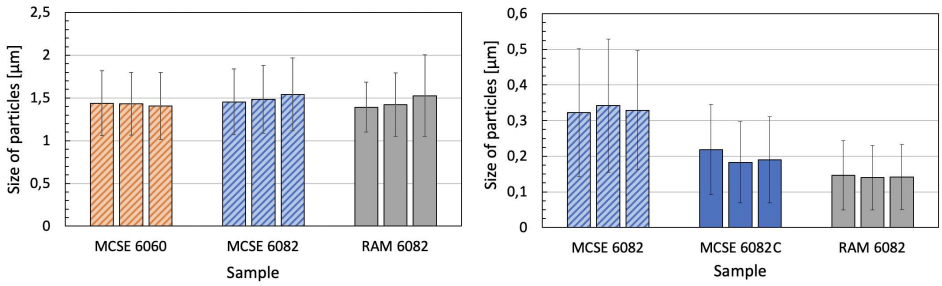

(a) Primary particles. **(b)** Dispersoids.

Figure 4.27: Average size of particles. Three analyzed images for each sample.

Figure 4.28 shows the number density of primary particles and dispersoids. For primary particles, number density is ∼3 times higher in MCSE 6082 and RAM 6082 compared to MCSE 6060. For dispersoids, RAM 6082 has a much higher number density, ∼3 times higher than MCSE 6082C and ∼9 times higher than MCSE 6082.

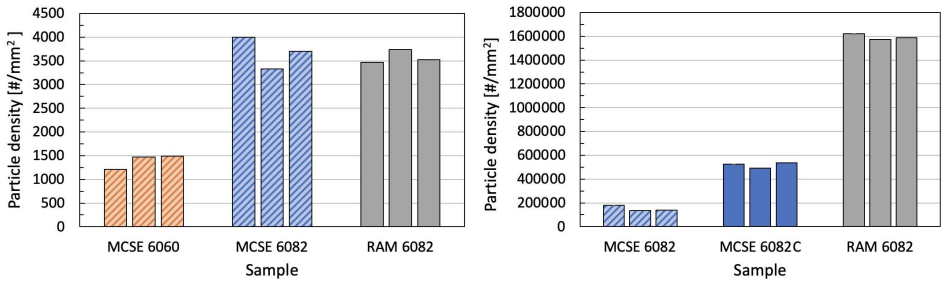

(a) Primary particles. **(b)** Dispersoids.

Figure 4.28: Number density of particles. Three analyzed images for each sample.

Figure 4.29 shows the area fraction of primary particles and dispersoids. Obser-

vations are similar to those of the number density of particles, but the difference in area fraction of dispersoids is somewhat lower because of the dispersoids being larger in both MCSE 6082 and MCSE 6082C (Figure 4.27b).

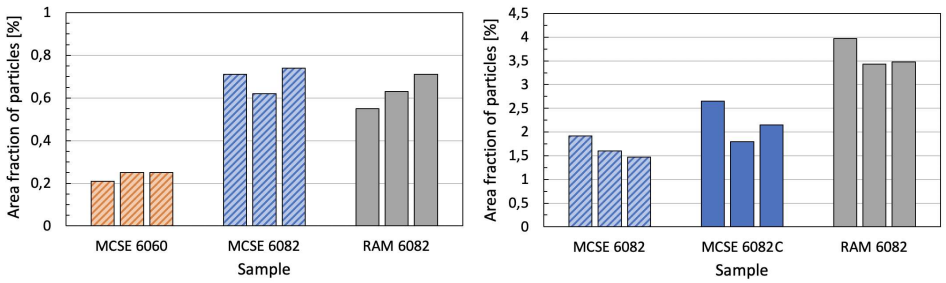

(a) Primary particles.

(b) Dispersoids.

Figure 4.29: Area fraction of particles. Three analyzed images for each sample.

TEM images of dispersoids are shown in Figure 4.30. In general, the dispersoids observed in RAM 6082 were smaller, aligned and more numerous compared to MCSE 6082C. A total of 8 dispersoids can be counted for MCSE 6082C in Figure 4.30a, against ∼50 dispersoids for RAM 6082 in Figure 4.30c. Image size is similar in both pictures, but too small to perform any accurate statistical analysis. However, the difference is significant and comparable to the observations in SEM (Figure 4.25). Representative images of the morphology and sizes of dispersoids in MCSE 6082C and RAM 6082 are shown in Figure 4.30b and 4.30d, respectively. The dispersoids in both MCSE 6082C and RAM 6082 were shown to contain about similar amounts of Fe, Si, Mn and Cr (Appendix D).

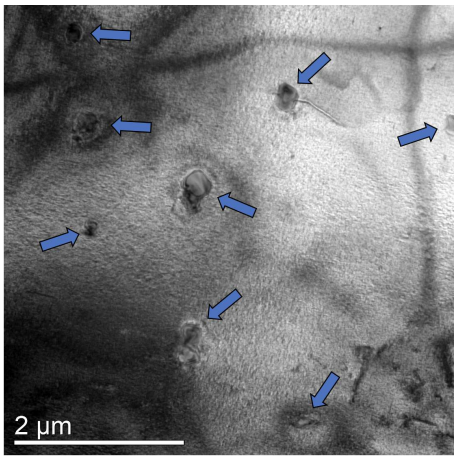

(a) MCSE 6082C dispersoid distribution.

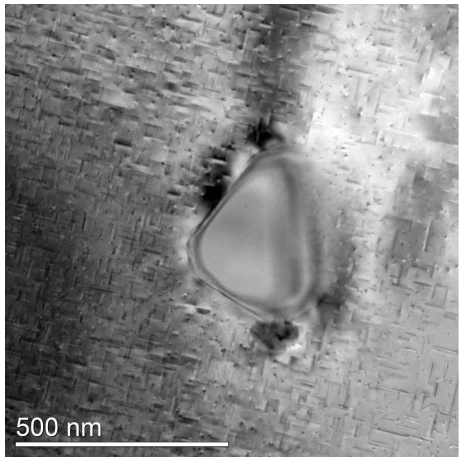

(b) MCSE 6082C dispersoid close-up.

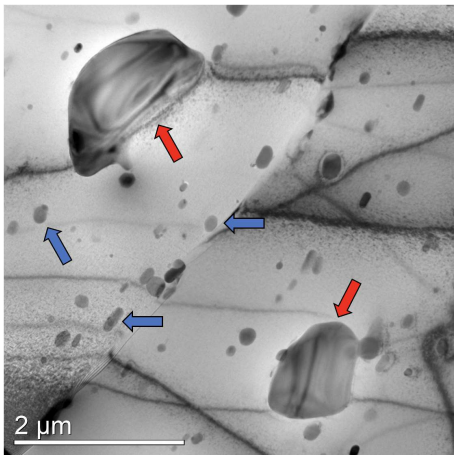

(c) RAM 6082 dispersoid distribution.

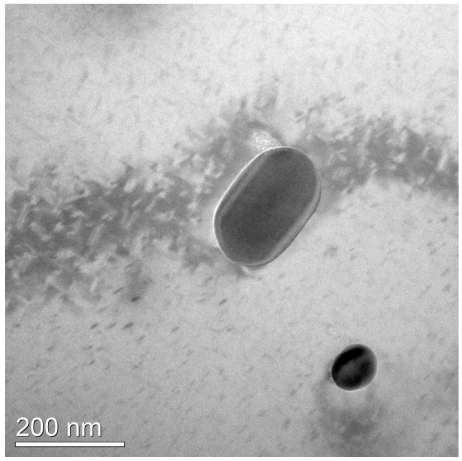

(d) RAM 6082 dispersoid close-up.

Figure 4.30: Dispersoids in extruded profiles, T6b condition. Imaged in regular bright field TEM. Dispersoids are shown in blue arrows, primary particles in red arrows. Only a fraction of the dispersoids in (c) are highlighted with arrows, while all visible dispersoids are highlighted in (a). Notice the varying scale bars.

Figure 4.31 shows the precipitate distribution in extruded profiles, T6b condition. Precipitates in MCSE 6060C seem to be marginally shorter compared to MCSE 6082C and RAM 6082. Comparing MCSE 6082C to RAM 6082, length and width of precipitates are about similar. As the thickness of each sample was not properly measured, a quantitative analysis on the number density of precipitates could not be performed.

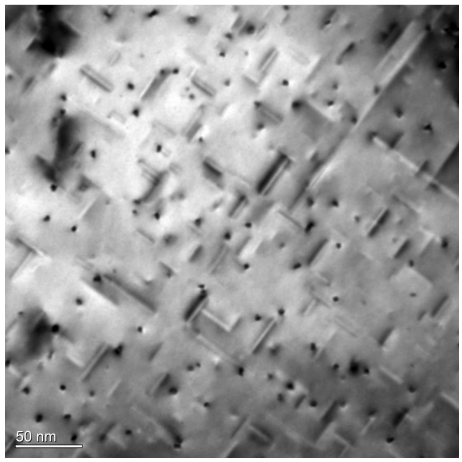

(a) MCSE 6060C.

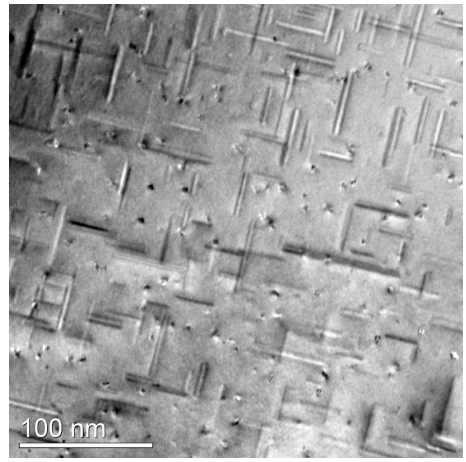

(b) MCSE 6082C.

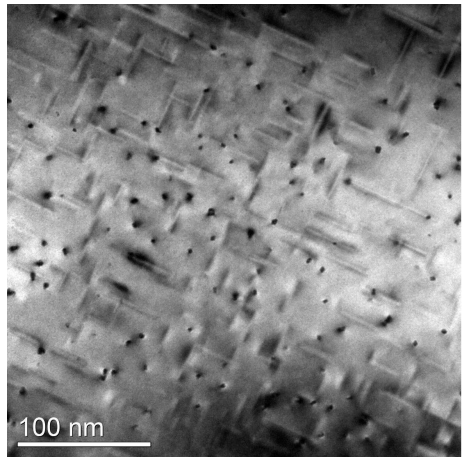

(c) RAM 6082.

Figure 4.31: Hardening precipitates of extruded profiles in T6b condition. Imaged in regular bright field TEM near the [001] zone axis.

Dimensionless histograms showing length distribution of precipitates are presented in Figure 4.32. The histograms confirm that precipitates in MCSE 6060C were slightly shorter compared to the other two, with a distribution more centered around lengths from 10-25 nm. For both MCSE 6082C and RAM 6082 the distributions are shifted to the right, with a higher frequency of larger precipitates. Precipitates in MCSE 6082C were (on average) slightly longer compared RAM 6082, as well as a "fatter tail" for the distribution of MCSE 6082C.

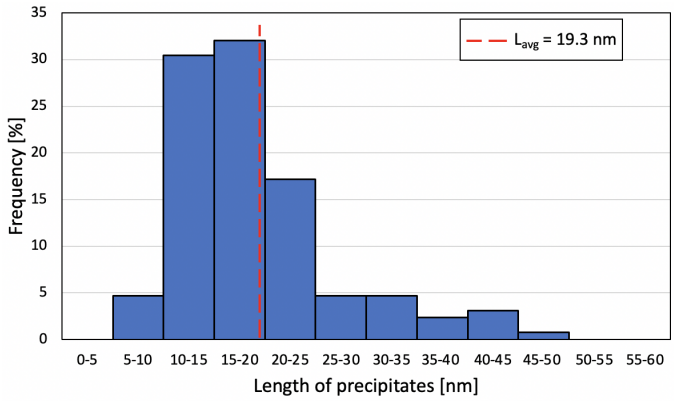

(a) MCSE 6060C. Total number of precipitates counted: 128.

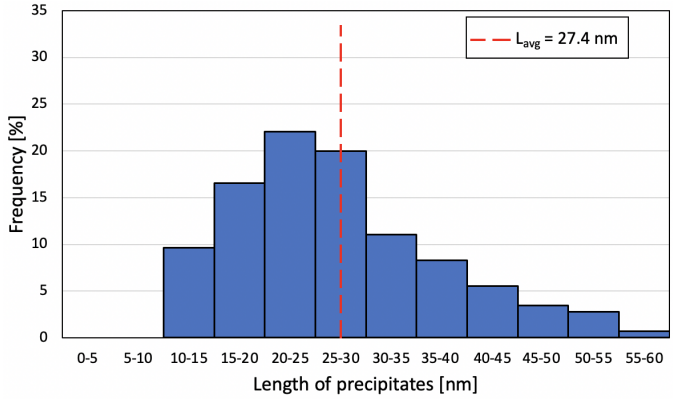

(b) MCSE 6082C. Total number of precipitates counted: 145.

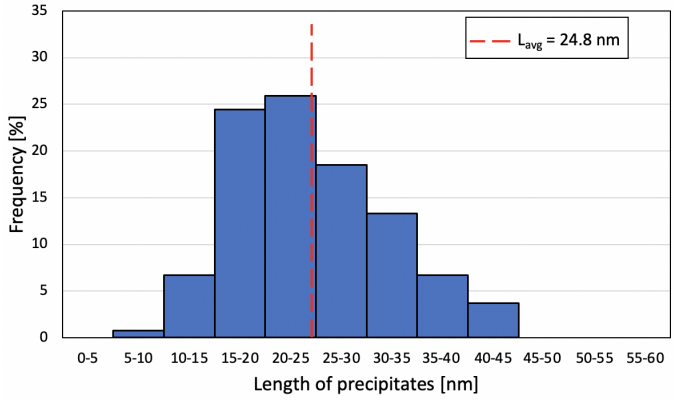

(c) RAM 6082. Total number of precipitates counted: 135.

Figure 4.32: Length distribution of precipitates. Measurements were manually performed on TEM images in Figures 4.31. Only precipitates in the image xy-plane were measured.

Grain boundary observations are shown in Figure 4.33. Particles and/or dispersoids are seen pinned on grain boundaries in all three samples. Such observations were more frequent in the two samples containing dispersoids, i.e. MCSE 6082C and RAM 6082.

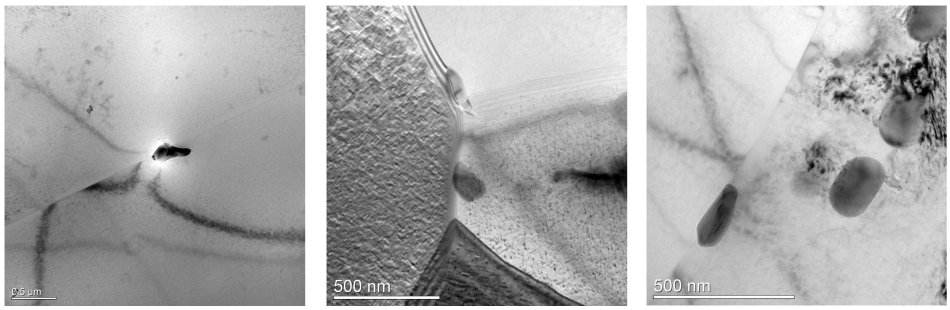

(a) MCSE 6060C. **(b)** MCSE 6082C. **(c)** RAM 6082.

Figure 4.33: Grain boundary pinning in extruded profiles, T6b condition. Imaged in regular bright field TEM.

4.4.4 Mechanical properties

Hardness measurements

Figures 4.34–4.36 present the measured hardness of both longitudinal and transverse cross sections, as-extruded condition. Measurements indicate a homogeneous strength throughout both cross sections for all three samples, with no clear variations. All hardness measurements can be found in Appendix E.

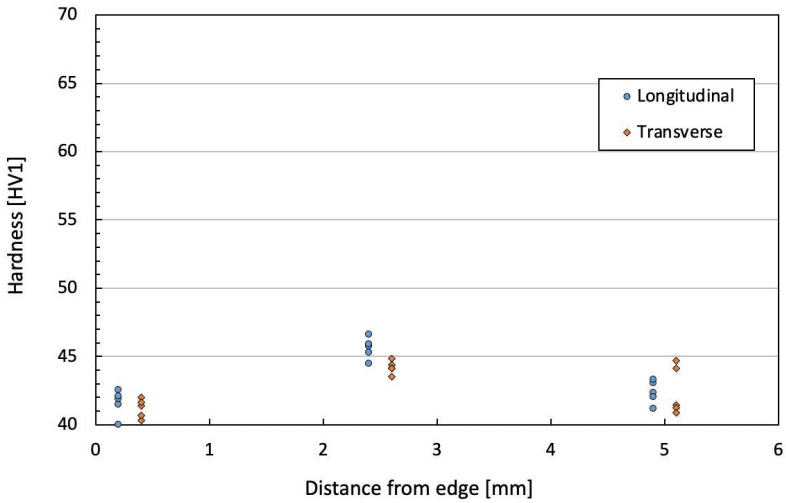

Figure 4.34: Hardness measurements of MCSE 6060C in as-extruded condition. Both longitudinal and transverse cross section are presented.

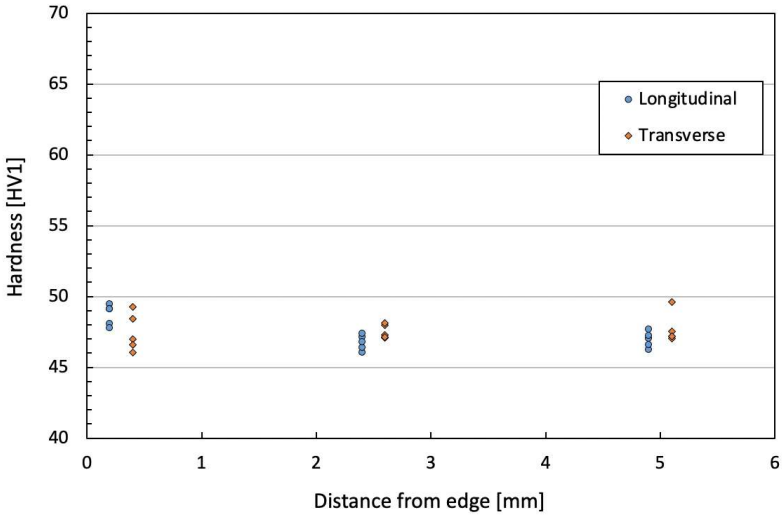

Figure 4.35: Hardness measurements of MCSE 6082C in as-extruded condition. Both longitudinal and transverse cross section are presented.

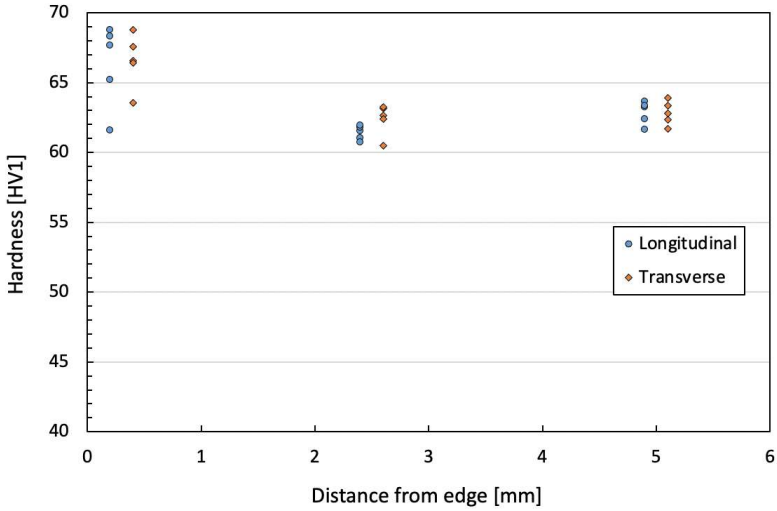

Figure 4.36: Hardness measurements of RAM 6082 in as-extruded condition. Both longitudinal and transverse cross section are presented.

Tensile tests

Results from tensile tests are shown in Figures 4.37–4.39 in terms of nominal stress and strain. Specimens from RAM 6082 were not included in trials named "Age hardened", i.e. as-extruded and aged samples, due to a limited amount of extruded profiles left from the trials with RAM 6082. Figures 4.40–4.42 summarize the numerical results gathered from all tensile tests in tables, and compares yield strength, ultimate tensile strength and elongation at fracture. Parallel T6b (1) for MCSE 6082 (Figure 4.38) was partially unsuccessful, as the force was initially too low and therefore adjusted during the test.

All samples seem to have responded to the change in heat treatment schedule by showing an increase in UTS when lowering ageing temperature and increasing holding time, i.e. from T6a to T6b. The only exception being one parallel for RAM 6082, namely T6b (1) in Figure 4.39, where yielding started earlier. The difference between MCSE 6082C and RAM 6082 is also noticeable, where MCSE 6082C shows significantly higher yield strengths and UTS values for all tests in T6 condition. On average, the difference was ∼60 MPa for both yield strength and UTS. Complete tables with numerical results are given in Appendix F.

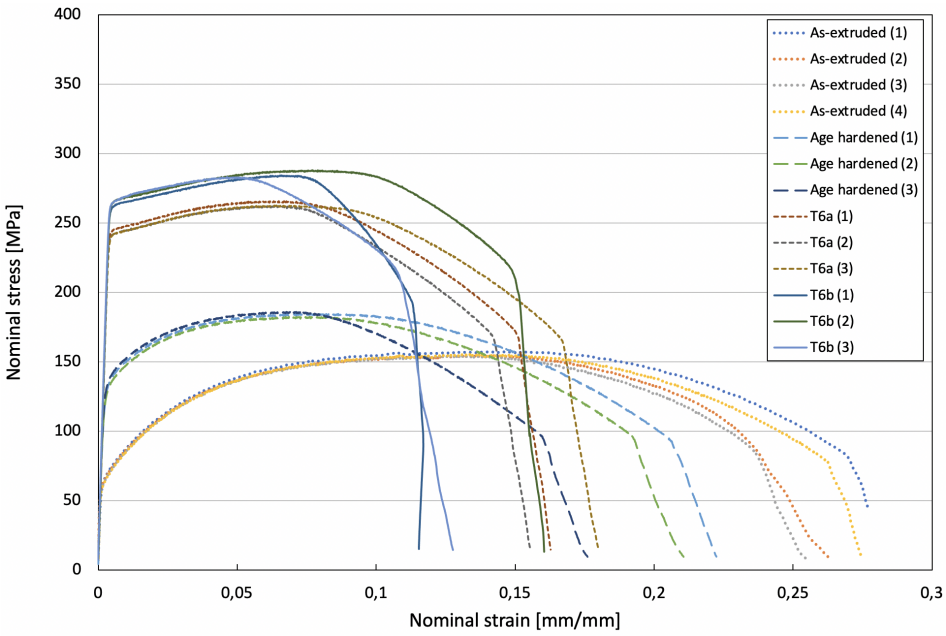

Figure 4.37: Tensile tests of MCSE 6060C.

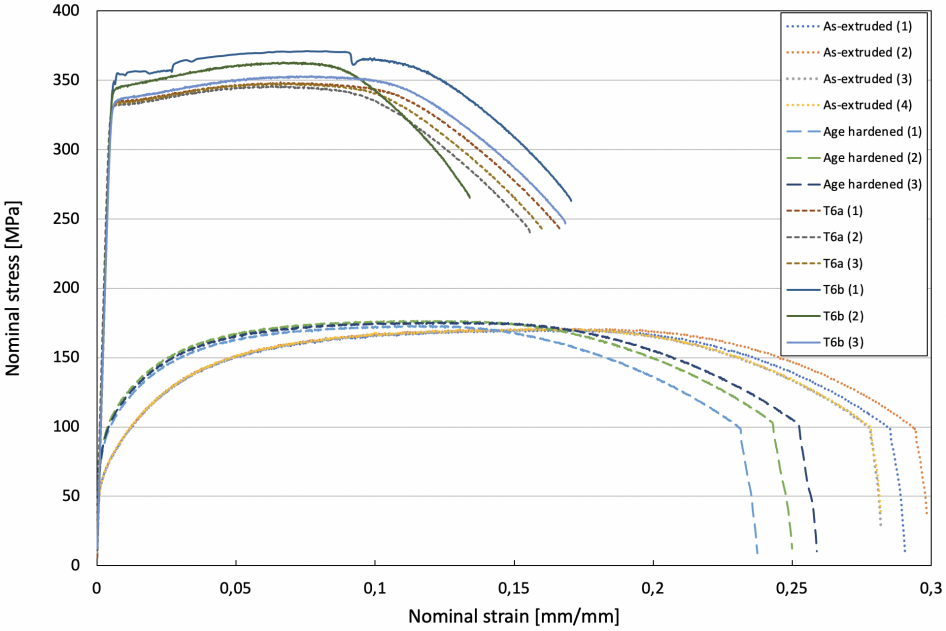

Figure 4.38: Tensile tests of MCSE 6082C.

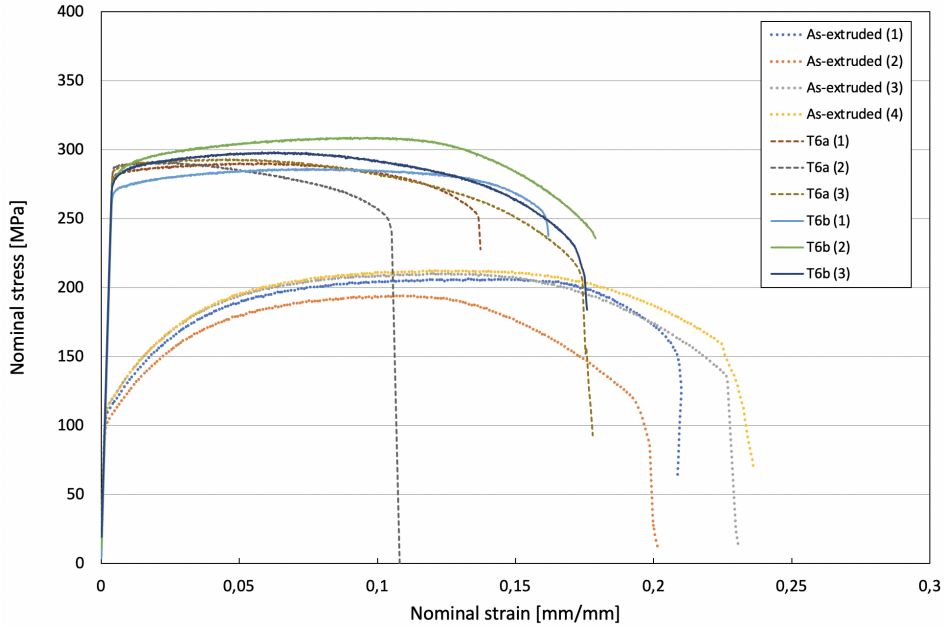

Figure 4.39: Tensile tests of RAM 6082.

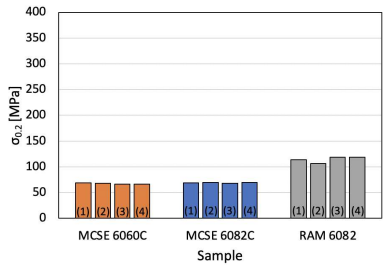

(a) As-extruded.

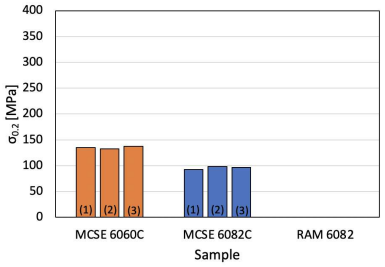

(b) Age hardened.

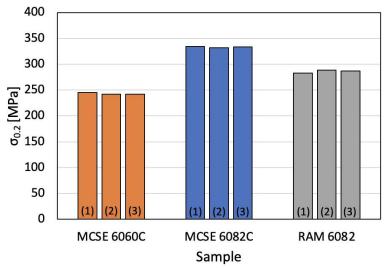

(c) T6a.

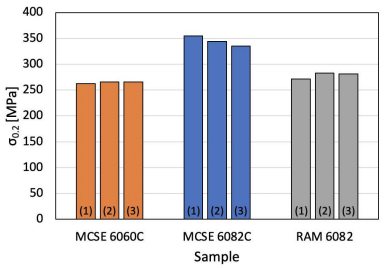

(d) T6b.

Figure 4.40: Yield strength of extruded profiles.

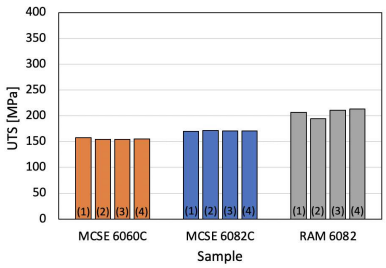

(a) As-extruded.

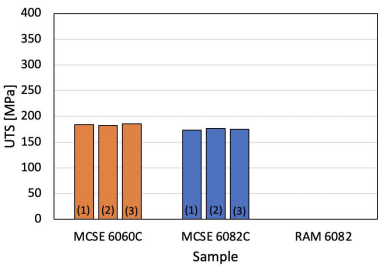

(b) Age hardened.

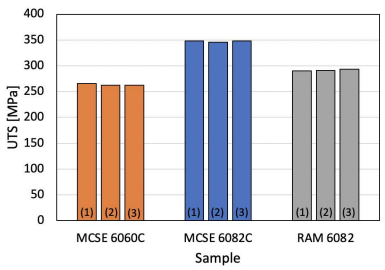

(c) T6a.

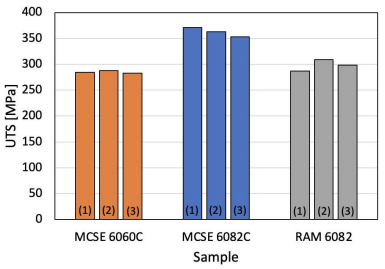

(d) T6b.

Figure 4.41: Ultimate tensile strength of extruded profiles.

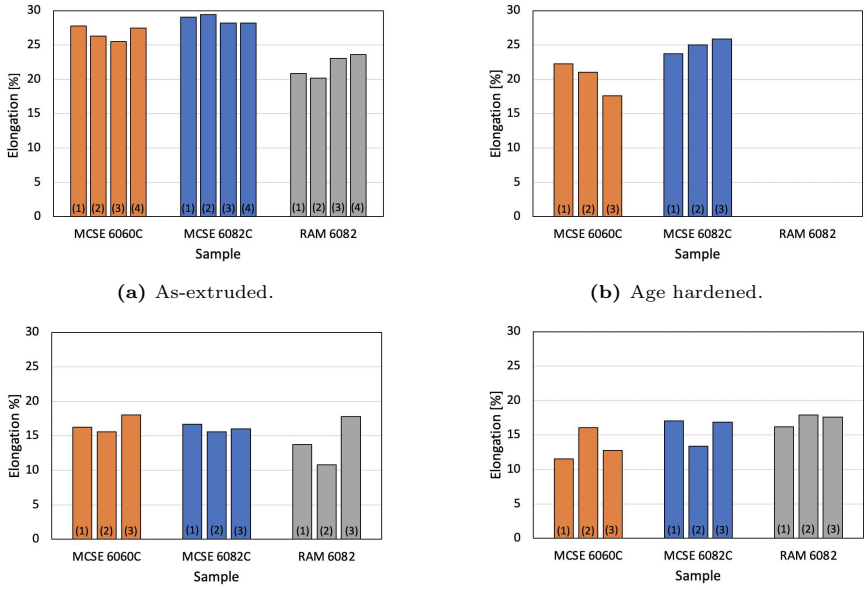

(a) As-extruded.

(b) Age hardened.

(c) T6a.

(d) T6b.

Figure 4.42: Elongation at fracture of extruded profiles.

4.4.5 Fractography

Fracture surfaces of representative tensile test specimens in as-extruded and T6b conditions are shown in Figure 4.43 and Figure 4.44.

The global fracture surfaces (Figure 4.43) indicate fractures along a spiraling pattern for the screw extruded samples. However, these "hills and valleys" in circles are not present for the same material in T6b condition. In addition, a significant increase in fracture diameter can be seen by comparing the screw extruded samples in as-extruded condition with T6b. For RAM 6082 the fracture surface is more faceted and also non-circular. In Appendix G, features in Figure 4.43b are further inspected, as there seems to be one large contaminant left to the center. Visual inspection indicates that fracture occurred 45° to the tensile direction for all samples in T6b condition (also shown in Appendix G).

The local fracture surfaces (Figure 4.44) indicate ductile behaviour for all samples, with formation of microvoids and dimples. The as-extruded specimens are mostly characterized by fracture from tensile stress, while the T6b specimens have a higher degree of dimples from shear stress.

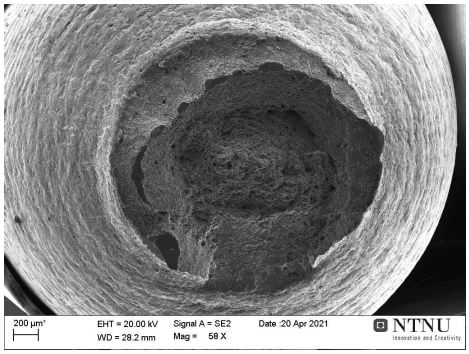

(a) MCSE 6060C as-extruded.

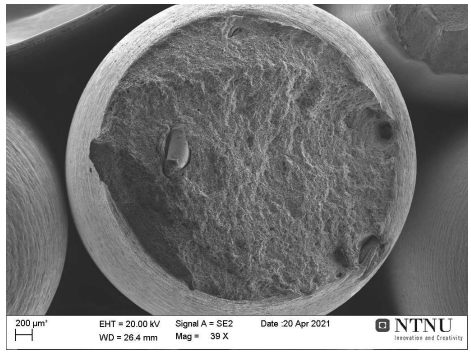

(b) MCSE 6060C T6b.

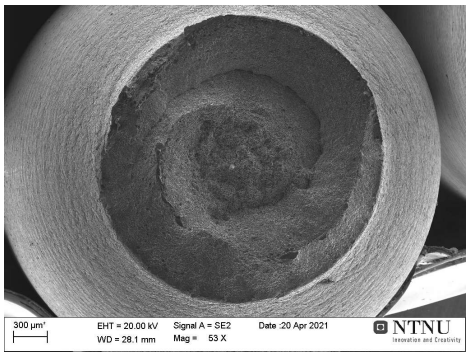

(c) MCSE 6082C as-extruded.

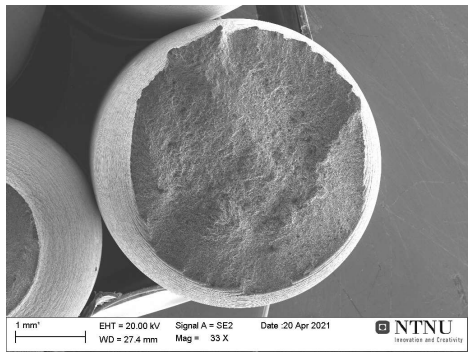

(d) MCSE 6082C T6b.

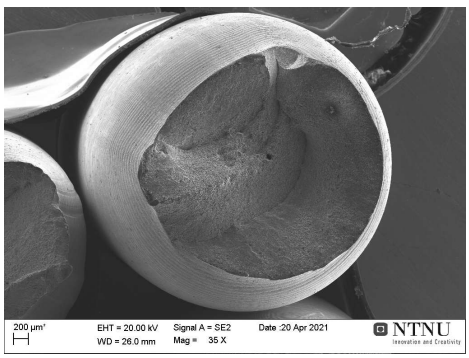

(e) RAM 6082 as-extruded.

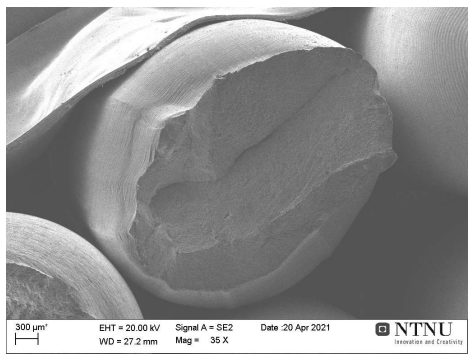

(f) RAM 6082 T6b.

Figure 4.43: Global fracture surfaces of representative extruded profiles after tensile tests. The left column shows samples in as-extruded condition, the right column shows samples in T6b condition.

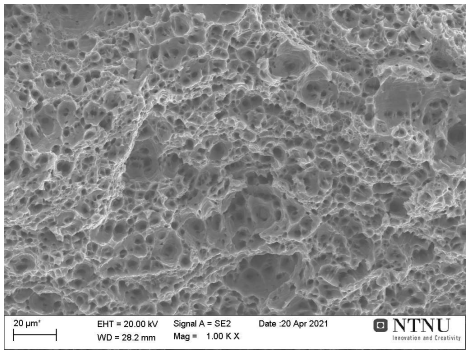

(a) MCSE 6060C as-extruded.

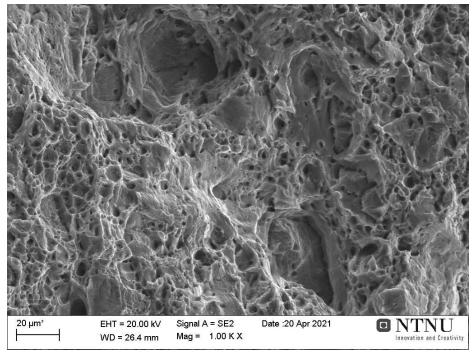

(b) MCSE 6060C T6b.

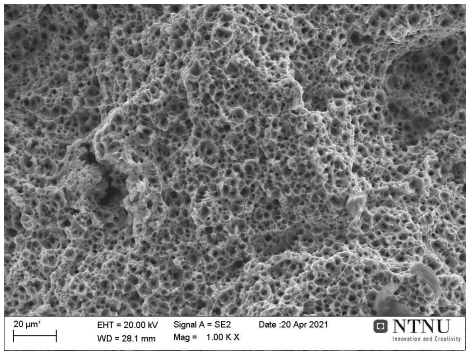

(c) MCSE 6082C as-extruded.

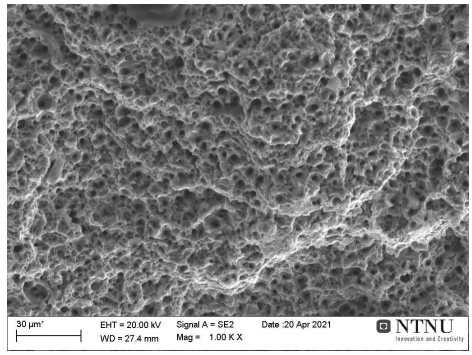

(d) MCSE 6082C T6b.

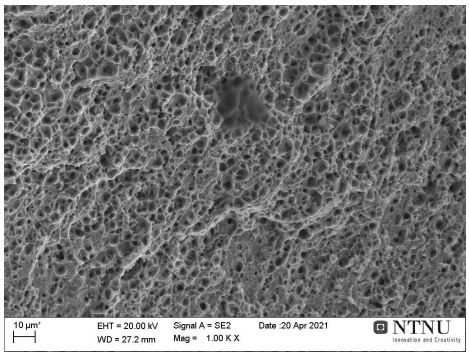

(e) RAM 6082 as-extruded.

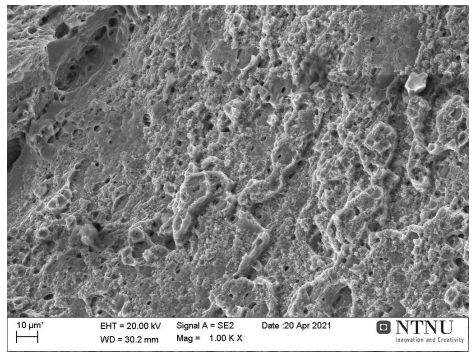

(f) RAM 6082 T6b.

Figure 4.44: Local fracture surfaces of representative extruded profiles after tensile tests. Images are taken from the middle of each respective image in Figure 4.43. The left column shows samples in as-extruded condition, the right column shows samples in T6b condition.

Area reduction at fracture is shown in Figure 4.45. For the screw extruded samples MCSE 6060C and MCSE 6082C, a clear reduction can be seen from as-extruded to T6b condition. However, this is not the case for RAM 6082, where area reduction is about similar in both cases. Also, it should be emphasized that the fracture surface of RAM 6082 in T6b condition was more elliptical than circular (Figure 4.43f). Therefore, the area of that specific sample was calculated as an ellipse. The measured diameters of fracture surfaces are displayed in Table 4.1. For RAM 6082 in T6b condition, these are the semi-major and semi-minor axes used for calculating the area of an ellipse. For the other five fracture surfaces, an average of two measured diameters are presented.

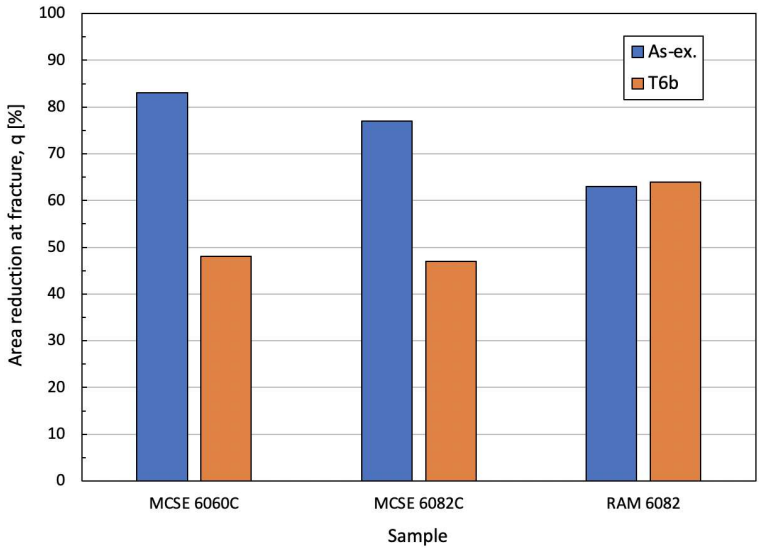

Figure 4.45: Area reduction after fracture from tensile testing.

Table 4.1: Measured diameter (mm) of fracture surfaces.

	MCSE 6060C	MCSE 6082C	RAM 6082
As-extruded	2.04	2.43	3.03
T6b	3.60	3.63	3.96/2.29[a)]

[a)] Shape of fracture surface was elliptical, hence two measured diameters.

5 Discussion

In this chapter, the significance of the presented results will be explored in further detail. Topics will be covered in a similar order as the previous chapter.

5.1 Extrusion ingot and feedstock material

The microstructural differences observed in Figure 4.1 (smaller grain sizes for 6082) seem reasonable given that 6082 had a marginally higher Ti content than 6060 (Table 3.1). Titanium has the highest grain growth restriction in aluminium, and will act as heterogeneous nucleation sites during casting and solidification [66]. Further, if the addition of grain refiner for the two castings was approximately equal, 6082 would have had a higher grain growth restriction from the other elements alone, as the concentration of each alloying element was higher than 6060.

A transformation from β- to α-AlFeSi as well as spherodization of α-AlFeSi is expected for both alloys, in addition to formation of Mn- and Cr-containing dispersoids for 6082. The former is highlighted in Figure 4.2, and is comparable to the micrographs presented in Figure 2.8. The lower resolution of a light optical micrograph is not fully able to capture the dispersoids, but they are seemingly visible in the matrix of 6082 (Figure 4.2b), which is more easily seen when comparing to the dispersoid-free aluminium matrix of 6060 (Figure 4.2a). Since the cooling rate after homogenization was relatively slow (400 °C/h, Figure 3.1) it is possible that the dispersoids were decorated with Mg-Si particles (e.g. β' needles) and therefore became more visible. Nevertheless, it is reasonable to assume that the homogenization at 575 °C for 2 hours and 15 min was sufficient to promote the transformation from β- to α-AlFeSi, spherodization of α-AlFeSi and precipitation of dispersoids. For 6082, due to the high content of Mn, it is also possible that most of the α-AlFe(MnCr)Si was formed during solidification, and that the homogenization step mainly promoted particle break-up and spherodization of particles [11].

The state of which the material enters the screw extrusion process is crucial with regards to properties and appearance of extruded profiles. In general, a process such as machining of aluminium will introduce severe deformation and thus increase the dislocation density of the material. This will, in turn, increase the driving force for recovery and recrystallization at elevated temperatures. Since 6060 has a lower recrystallization resistance than 6082 (Section 2.4), it seems likely that granules

from the 6060 extrusion ingot were recrystallized prior to screw extrusion.

To assess whether the thermal cleaning at 350 °C for 30 min affected the grain structure or not is a challenging exercise, as images were only taken prior to the heating step. As explained in Section 2.4, recrystallization behaviour is primarily dependent on two factors: strain rate and temperature. A cooling lubricant was used to reduce the friction during machining, decreasing the deformation and subsequent stored energy in the material.

For the 6060 feedstock, it seems likely that recrystallization occurred only moments after deformation [25]. If not fully recrystallized after machining, the stored energy in combination with an elevated temperature (350 °C) would likely have promoted recrystallization. For the 6082 feedstock, an annealing temperature of 350 °C seems too low to initiate recrystallization. Hjorth [67] conducted a thorough study on the recrystallization behaviour of AA6082 after torsion and subsequent heat treatment. For a wide range of Zener-Hollomon parameters, no recrystallization after heat treatment at 350 °C was reported. Therefore, a fibrous structure of 6082 feedstock after thermal cleaning seems reasonable. Also, this is in accordance with observations from Kristiansen [63], where feedstock imaged after thermal cleaning at 350 °C for 30 min revealed a fibrous structure of 6082 feedstock and a recrystallized structure of 6060 feedstock.

5.2 Aluminium plug

5.2.1 Microstructure

As the microstructure development through the screw extruder has not been thoroughly investigated in previous work, no direct comparison can be made across reports. However, studies on material flow (Section 2.10.1) are closely related and will serve as a foundation for synthesizing the results.

The grain structure observed in Plug 6060C closest to the extrusion die (Figures 4.5-4.7) can be divided into three main classes: coarse elongated grains, small elongated grains and equiaxed grains. These were observed in specific locations along the extrusion chamber and can be compared to the material flow. Combined with terminology from Figure 2.15, the coarse elongated grains were typically seen in "Dead zones", while the small elongated grains were seen in zones with "Fast moving material". The equiaxed grains were primarily found in front of the screw end, i.e. in a zone of "Slow replacement" (Figure 2.14). The above mentioned findings are summarized as a schematic drawing in Figure 5.1.

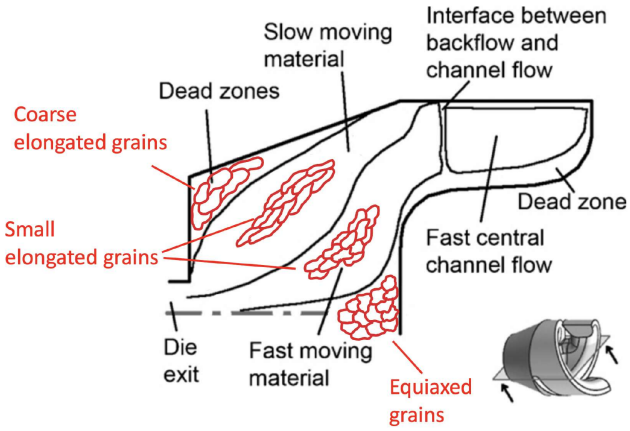

Figure 5.1: Summary of the microstructural development through the screw extruder. Modified figure from [59].

The microstructural development appeared in many ways similar to that of conventional ram extruded aluminium, presented in Figure 2.6. A detailed study conducted by Güzel et al. [68] gives further insight into grain structure development. In their study, a small AA6082 extrusion ingot was characterized by light optical microscopy and EBSD during extrusion. The main findings from their study are presented in Figure 5.2.

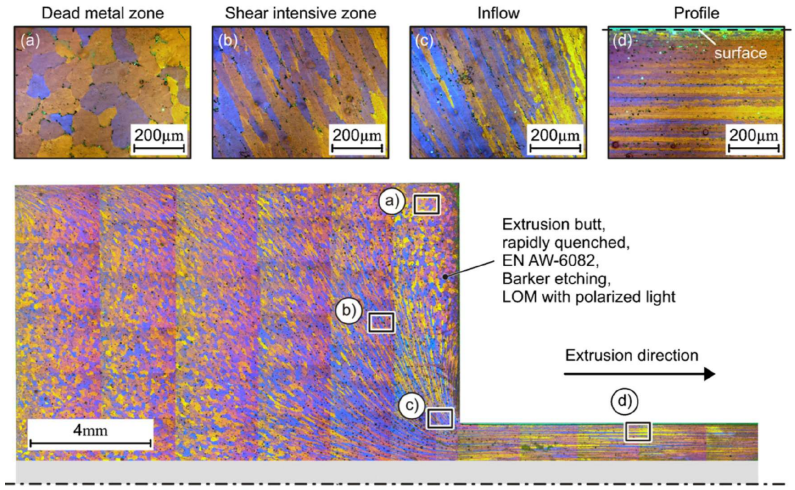

Figure 5.2: Grain structure of a conventional AA6082 extrusion butt using polarized light, taken from Güzel et al. [68]. Four areas are highlighted: (a) dead metal zone, (b) shear intensive zone, (c) inflowing material zone, and (d) exiting profile zone.

Firstly, a dead metal zone was located in both Figures 5.1 and 5.2 . For the extrusion ingot of Güzel et al., this area consisted mainly of equiaxed grains. This resembled the initial microstructure of the extrusion ingot, and was explained by negligible plastic strain and strain rates due to the material being stationary in this position. For the screw extruder, coarse elongated grains were observed in an equivalent area. Although characterized as a dead zone, material will still move relative to the extrusion die, due to constant rotational motion from the screw, as explained by Widerøe and Welo [59]. The hydrostatic pressure as well as rotational motion from the screw, together with an elevated temperature, are likely to have caused high enough strain rates and subsequent recrystallization for the 6060 alloy. As the metal in the dead zone was stationary in the extrusion direction, the grains were left to grow considerably larger than areas of fast material flow.

Secondly, the two zones characterized as "Shear intensive zone" and "Inflow" in Figure 5.2 are similar to the zones with "Slow moving material" and "Fast moving material" in Figure 5.1, respectively. Material along zones of "Fast moving material" will flow more easily into the extrusion die, while material along "Slow moving material" will experience high shear deformation, explained by differences in the velocities of upper and lower boundary by Güzel et al. Observations of grain morphology in these areas are similar in both figures (Figures 5.1 and 5.2), and consist of small elongated grains in the extrusion direction.

Lastly, the zone associated with "Equiaxed grains" in Figure 5.1 is not highlighted in Figure 5.2. However, equiaxed grains (from the initial extrusion ingot) can clearly be seen farther away from the extrusion die in Figure 5.2. Although similar observations, the process leading up to equiaxed grains in the screw extrusion process is not the same. While the conventional ram extrusion process (typically) starts from a homogenized extrusion ingot with an equiaxed grain structure, screw extrusion starts from granules typically with a deformation structure or partly recrystallized structure. Through the screw extrusion process, granules will be compacted and subject to severe deformation before reaching the extrusion die, as presented in Section 2.10.2. Therefore, the equiaxed grains observed in Plug 6060C are likely a product of recrystallization. Average grain size in these areas was 40–50 µm (Figures 4.5–4.7), compared to the average grain size of ∼100 µm for extrusion ingot samples of 6060 (Figure 4.1).

Assessing whether the observed microstructure is a result of dynamic or static recrystallization is a challenging exercise based on images from light optical microscopy alone. In addition, none of the trials performed in this study were water quenched, only air cooled. Log data (Figure A.4) shows that the temperature dur-

ing screw extrusion was about 560 °C before air cooling started. In other words, post-recrystallization effects (static recrystallization) were not avoided. Also, the plug was subject to severe mechanical deformation in the outer layers when removing parts after screw extrusion, as explained in Section 3.2. Trials with controlled cooling and more careful removal of the plug could provide further insight into the recrystallization behaviour.

Images farther away from the extrusion die (Figures 4.8–4.10), as well as images from Plug 6082C (Figure 4.11), were harder to analyze due to the more chaotic appearance of the grain structure. It is, however, interesting to note the structured layers of grains in Figure 4.9b which suggest that the rotating screw pushed the material forward batch-wise, i.e. each time the screw tip passed the area it deposited new material on top of existing material. This was also shown in the study by Widerøe and Welo.

5.2.2 Intermetallic particles

The homogeneous distribution of primary particles in both Plug 6060C (Figure 4.12) and Plug 6082C (Figure 4.13) seems reasonable given that the rotational motion of the screw caused movement in spirals and constant collisions (in all directions) of granules. Observations during the project work preceding this master's thesis resulted in a hypothesis of primary particle evolution during screw extrusion [10]. It was proposed that frictional forces and high shear deformation throughout the screw extrusion process could cause disintegration of primary particles into smaller spheroidized particles. The suggested mechanism is shown in Figure 5.3.

Figure 5.3: A hypothesis of primary particle evolution through the screw extruder. From [10].

By comparing primary particle observations in extrusion ingots (Figure 4.2) to aluminium plugs (Figures 4.13), there is seemingly a higher number density of particles in the plugs. As explained in Section 2.5.1, fragmentation of AlFeSi-particles has been observed in subcutaneous layers during conventional extrusion, in areas with high shear deformation. However, fragmentation similar to those in Figure 2.9 could not be directly observed in the present study. Other researches, e.g. Szczygiel et al. [69, 70], found similar particle disintegration of aluminium in studies

on severe plastic deformation (SPD) through the equal channel angular pressing (ECAP) technique. In their reports it was referred to as "particle break-up" and could be observed by both LOM and SEM. Although not directly observed in the present study, the possibility should not be ruled out, given the severe deformation through the screw extruder. More careful investigations of samples from the aluminium plug in SEM, similar to the images in Figure 2.9, could reveal more information on the suggested mechanism of particle fragmentation.

In the micrographs of intermetallic particles in Plug 6082C (Figure 4.13), there are particles that resemble the morphology of β-AlFeSi particles in as-cast Al-Mg-Si extrusion ingots (e.g. shown in Figure 2.8). A selected area from Plug 6082C containing these particles is shown in Figure 5.4. The thin, elongated particles are observed in most images of primary particles through Plug 6082C, but not in images before (extrusion ingot samples and feedstock material) and after (screw extruded profiles). Chemical composition of the mentioned particles was not investigated, but colour appearance in LOM (Figure 5.4) suggests that they are typical AlFeSi-particles and similar to the other intermetallic particles in the structure. Considering that the extrusion ingots prior to screw extrusion were homogenized at 575 °C for 2 hours and 15 minutes, α-AlFeSi is expected to be the dominant phase. However, it is possible that not all β-AlFeSi was transformed during the homogenization. This explains the observations in Figure 5.4 but not the fact that similar particles were not observed in micrographs of screw extruded profiles. Also, it is conceivable that the deformation through the screw extruder is so inhomogeneous that some areas are significantly less deformed than others, so that the particles retain much of their original shape. Then, upon further deformation through the extrusion die, the elongated phases are broken into smaller particles and are therefore not visible in the extruded profile.

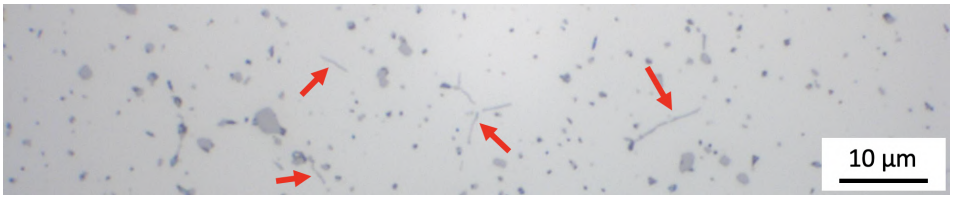

Figure 5.4: Observations of primary particles in Plug 6082C, Sample 3. Imaged in bright field light optical microscopy. Thin, elongated phases are highlighted with red arrows.

5.3 Extruded profiles

5.3.1 On the effect of CO_2 as cover gas

Based on promising results on the use of CO_2 as an oxidation inhibitor for aluminium alloys (Section 2.8), it was believed that CO_2 would reduce porosity in the screw extruded profiles. However, the effect from CO_2 was difficult to single out. As shown in Figure 4.15, the 6082 trial with CO_2 seems to have a reduced level of porosity, while 6060 appears similar in both trials. Two factors (other than atmosphere) that might have contributed to the observations in LOM are temperature during screw extrusion and different feedstock material.

Higher temperatures facilitate more rapid oxidation of aluminum, as shown in Figure 2.12, and should be considered an important factor. Log data from the screw extrusion trials (Appendix A) shows that temperatures in all four trials were stable around ∼560 °C, except for MCSE 6082 (Figure A.3), with more instability and a surge towards 600 °C at the end of screw extrusion. The instability in temperature might have caused an uneven compacting of granules and thus allowed for more oxidation, and, in turn, contributed to the porous appearance in Figure 4.15c. The other factor, feedstock material, follows a similar argument as that of temperature differences: For the trials with CO_2, both smaller and thinner feedstock (Figure 3.3) were utilized, compared to the two trials in ambient air atmosphere. This might have facilitated a more successful compacting and thus introduced smaller amounts of oxides into the screw extruded material. On the other hand, smaller granules lead to a higher surface-area-to-volume ratio and thus more surface oxides, but this do not seem to have affected the level of porosity in the profiles with smaller granules (MCSE 6060C and MCSE 6082C). Worth noting is that the thermal cleaning of feedstock in all trials was similar, i.e. 350 °C for 30 min, and is not expected to have contributed differently on oxidation of the feedstock.

In the study conducted by Ragnvaldsen [61], briefly presented in Section 2.10.3, a similar mechanism to that presented by Smith et al. [56] was suggested for the effect of CO_2 during screw extrusion. It was proposed that a complex oxide phase was formed around CO_2 absorbed on the surface during screw extrusion, due to the reduction in oxygen partial pressure caused by the constant flushing of CO_2. Further, it was assumed that the oxide phase would act as a protective cap and decrease the rate of out-diffusion and oxidation of Mg. A similar mechanism could be argued for in the Al-Mg-Si alloys used in the present study, but the porosity was not thoroughly investigated by other methods than LOM. Results are, however, promising and indicate a positive effect on oxidation inhibition and

resulting porosity in screw extruded profiles.

5.3.2 Recrystallization behaviour

By comparing the microstructures in Figure 4.16, it can be seen that RAM 6082 was more prone to recrystallization (in outer layers) than MCSE 6082C. The difference between the two 6082 extrudates and 6060, however, is explained by dispersoids in 6082 that act as pinning points and retard the recrystallization after deformation. Although no ram extruded 6060 sample was included in the present study, results from Kristiansen [63] indicate a significant difference between screw and ram extruded 6060 samples. A collection of four studies on screw extruded 6060 are compared to the conventional ram extruded 6060 sample by Kristiansen in Figure 5.5. Clearly, the ram extruded sample is more recrystallized while the screw extruded samples appear more fibrous.

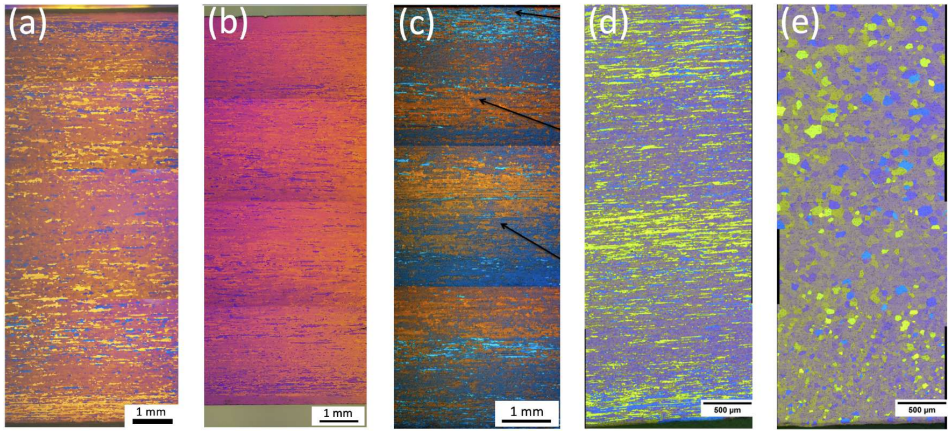

Figure 5.5: Comparison of grain structures in extruded 6060; a) MCSE 6060 [10], b) MCSE 6060C, c) Screw extruded 6060 by Bilsbak [62] (ignore black arrows), d) Screw extruded 6060 by Kristiansen [63], and e) ram extruded 6060 by Kristiansen. Temperature in the extrusion dies were ∼560 °C for all the screw extruded trials, and ∼500 °C in the ram extruded trial.

Firstly, temperatures in both processes should be compared. In both screw extrusion and ram extrusion, material exiting the extrusion die will experience high shear deformation, causing large strain rates at the surface. In addition, frictional forces will cause heating through deformation, which has the opposite effect on recrystallization [20]. Heat is generated at the surface but will spread through the profile as extrusion proceeds. Table 3.2 shows that the temperature close to the extrusion die was ∼560 °C for the screw extruded trials and ∼500 °C for the ram extruded trial. With regards to hot deformation, the extrusion die is the most important part

to consider, as the metal has "short memory" and recrystallization behaviour is primarily governed by the last deformation step [22]. This suggests that the higher temperatures during screw extrusion might have promoted increased dislocation cross slip and subsequent annihilation, which in turn lowered the stored energy in the material [33]. The screw extruded material would then have a smaller driving force for recrystallization than the ram extruded sample, which was extruded at a lower temperature.

The second factor, strain rate, can be estimated by Equation 2.2 for the ram extruded sample. Using the input parameters from Kristiansen ($D_B = 95$ mm, $D_E = 10$ mm, $V_R = 6$ mm/s) gives $\dot{\varepsilon} = 1.7\ s^{-1}$. Calculations for the screw extruder are more challenging due to the complex nature of rotational motion combined with the material entering through granules and not a continuous billet. The model created by Skorpen et al. [60], briefly presented in Section 2.10.2, considers all these factors and predicts a total accumulated strain of ∼15 through the screw extruder, compared to an equivalent strain of ∼4.5 for ram extrusion at similar conditions. However, process parameters from the screw and ram extrusion trials (Table 3.2) show that RAM 6082 had ∼7 times higher extrusion speed than MCSE 6082C. This might suggest that strain *rate* during screw extrusion was lower than during ram extrusion, in spite of the large differences in *strain*.

These two factors, temperature and strain rate, could explain the observed microstructure in screw extruded material, since low temperatures and high strain rates during deformation result in higher Zener-Hollomon parameters (Equation 2.1). A more in-depth analysis on recrystallization behaviour could be made by further developing the model by Skorpen et al. to include strain rate calculations. This would provide valuable input for calculations of the Zener-Hollomon parameter during screw extrusion. One possible mechanism that was suggested by Skorpen in another study (on the recrystallization resistance of screw extruder material) [7], is bands of finely dispersed oxide particles along elongated fibers, which was observed in an Al-10Mg alloy. This topic is further discussed in Section 5.3.6.

To follow up the investigations on recrystallization behaviour, light optical micrographs of extruded profiles after SSHT and subsequent water quenching are presented in Figure 5.6. The micrographs show a coarse recrystallized layer for MCSE 6060C, no recrystallization for MCSE 6082C, and abnormal grains for RAM 6082. By comparing the microstructure of RAM 6082 after SSHT to the microstructure in as-extruded condition (Figure 4.16), it becomes apparent that the fibrous structure of the core is much more prominent in as-extruded condition than after SSHT. Therefore, what appears to be a fibrous core after SSHT and water quenching (Fig-

ure 5.6c) might be only a few abnormal grains covering the whole cross section. The microstructures after SSHT are believed to have affected the mechanical properties, further discussed in Sections 5.3.7 and 5.3.8.

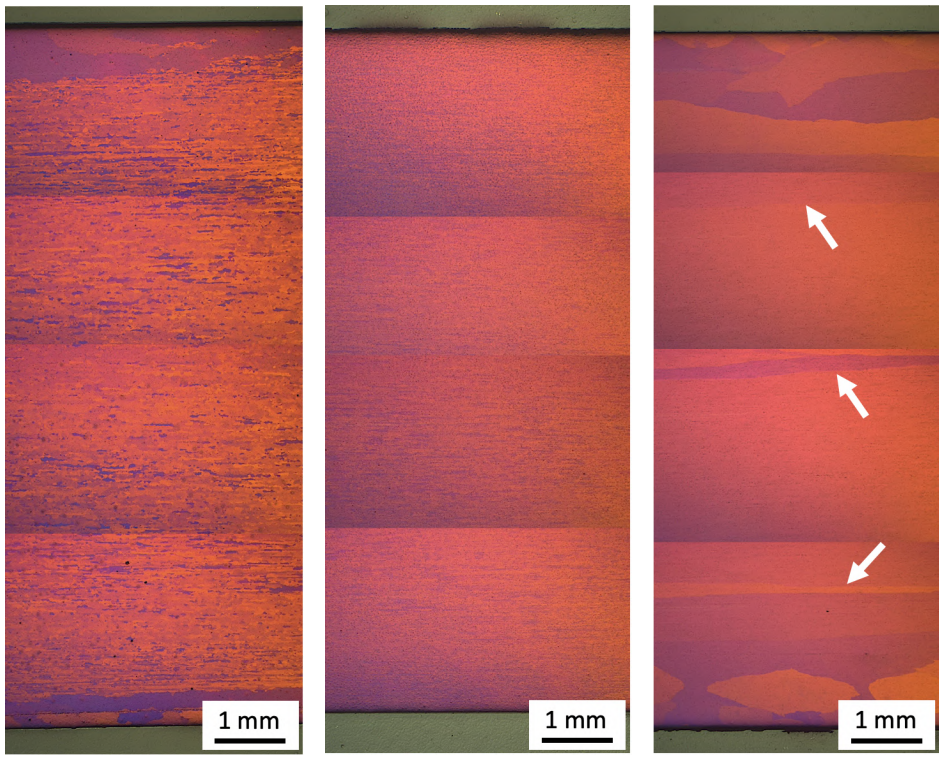

(a) MCSE 6060C. **(b)** MCSE 6082C. **(c)** RAM 6082.

Figure 5.6: Microstructures after SSHT (560 °C for 10 min) and subsequent water quenching. Anodized, longitudinal cross section under polarized light. White arrows in (c) indicate areas of abnormal grains.

5.3.3 Texture and grain size distribution

Extrusion textures from EBSD grain mappings in Figures 4.17–4.19 show that the profiles were dominated by <111> and <001> fibers in extrusion direction. These are both expected textures in extruded aluminium profiles, and occur through lattice rotations and slip activity [11]. Further, intensities of pole figures and inverse pole figures in Figure 4.23 show that the textures in MCSE 6082C and RAM 6082 were almost identical, while the figure for MCSE 6060C has somewhat lower intensities of both fibers. Zhang et al. [25] investigated conventional ram extruded AA6063 and found that the texture was a single strong <001> fiber (with no <111>) after extrusion at 550 °C and subsequent water quenching. In addition,

the grain structure was 71% recrystallized. The observations by Zhang et al. are considerably different from the ones in the present study, where <111> fibers were much more prominent in MCSE 6060C. The reason, however, is not clear, and needs further investigations.

Grain mappings shown in Figures 4.20–4.22 give further insight into the grain structure development. The multimodal distributions of MCSE 6082C and RAM 6082 suggest the presence of subgrains in both samples. The subgrain formation, in turn, indicates that the two structures were partially recovered, not recrystallized. This is supported by Figure 4.21, where the smaller grains appear elongated in extrusion direction, and not equiaxed. As was argued by Sakai et al. [71], recovery is a likely cause of the formation of subgrains in aluminium due to the high stacking-fault energy (SFE) and lowering of energy through annihilation of dislocations. While this seems reasonable for the two 6082 samples, no such multimodal distribution was found for MCSE 6060C, which suggests that the structure was partially recrystallized. As for the larger grains in MCSE 6060C (Figure 4.20), it is difficult to determine whether they are prolonged, deformed grains from the screw extrusion process or coarse recrystallized grains.

The resulting structure in MCSE 6060C is likely a result of static recrystallization (SRX) that occurred moments after extrusion. Zhang et al. found that recrystallization finishes within 2 seconds after high temperature extrusion and subsequent quenching for AA6063. Another possibility is continuous dynamic recrystallization (cDRX), which Satai et al. showed typically occurs during plastic deformation to very large strains in metals with high SFE. Screw extrusion of aluminium falls within this category, and could be investigated by comparing a deformed texture to a fully recrystallized texture after screw extrusion. As was also noted by Sakai et al., a recrystallized texture different from the deformed one would rule out cDRX.

Some considerations on the settings used for EBSD analysis should be made. The analysis and detection of grains in OIM are limited by the choice of step size, in this case 2 µm. A lower step size and more close-up micrograph on the two 6082 samples could reveal the subgrain structures better. Also, the method for counting grain size in OIM is by default the equivalent circle method. A more logical choice for fiber-like structures would be the line intercept method.

5.3.4 Primary particles and dispersoids

Particle analyses in Figures 4.27a and 4.28a show that the average size and number density of primary particles in MCSE 6082 and RAM 6082 were about similar. Pri-

mary particles display a stronger alignment in RAM 6082, Figure 4.24. The more homogeneous distribution in the screw extruded samples is attributed to the rotational motion of the screw and larger strains, i.e. a better mixing of the material. For the primary particles analyses, it should be noted that these were performed on the trials screw extruded in ambient air atmosphere, MCSE 6060 and MCSE 6082, due to difficulties with preparing samples for SEM without the automatic ultrasonic water-cleaner (Section 3.4.1). Analyses of primary particles for MCSE 6060C and MCSE 6082C are, however, not expected to deviate considerably.

The difference in dispersoid number density between RAM 6082 and screw extruded 6082 (both with and without CO_2 as cover gas) was not expected. Observations in SEM and subsequent analyses (Figure 4.28b) were strengthened by images from TEM (Figure 4.30), both showing a considerably higher number density of dispersoids in RAM 6082. Therefore, the difference is significant and should be given some consideration.

Although the dispersoids were smaller and more elongated in RAM 6082 (Figure 4.30), chemical analysis in EDS seems to confirm that they are of similar composition. This is shown in Appendix D. The analysis strongly suggests that both extruded profiles contained the same Al(MnCrFe)Si-dispersoids, as MCSE 6082C and RAM 6082 showed similar amounts of Fe, Si, Mn and Cr (Tables D.2 and D.3) in the EDS analysis of selected dispersoids. This was expected, as the dispersoid formation is a function of (a) alloying elements, (b) heating rate to homogenization temperature, and (c) homogenization temperature and time [15]. Since MCSE 6082C and RAM 6082 were produced from an identical extrusion ingot with similar homogenization scheme (Figure 3.1), chemical composition was expected to be equal. Apart from chemistry, the screw extrusion process seems to have altered the morphology and distribution of the dispersoids.

Two possible scenarios are: (a) dispersoids going into solid solution during screw extrusion, or (b) dispersoids being mechanically sheared into smaller particles. Firstly, solid solution content can be evaluated by measuring electrical conductivity of screw and ram extruded material, since atoms in solid solution increase the electrical resistivity in aluminium, hence decrease the conductivity [72]. Secondly, no literature has been found on dispersoids being easily shearable, and the latter should therefore be considered highly unlikely. Also, investigations in TEM did not reveal any particles smaller (but similar) to dispersoids. Further, it was unexpected that the material with the lowest number density of dispersoids (MCSE 6082C) seemed to have a higher recrystallization resistance than the material with the highest number density of dispersoids (RAM 6082). Therefore, new screw and

ram extrusion trials with dispersoid-containing alloys should be performed to see if observations are similar to those in the present study.

5.3.5 Precipitates

Following the arguments presented by Holmedal [47], briefly mentioned in Section 2.6.4, longer precipitates will contribute more to the overall strength, as they pierce more slip planes in the matrix than smaller precipitates. The histograms in Figure 4.32 show that MCSE 6082C has a stronger Weibull distribution than RAM 6082, i.e. a higher percentage of longer precipitates. This observation could explain some of the differences in mechanical properties (Figures 4.40–4.42), where MCSE 6082C outperformed RAM 6082. Further, if one makes the assumption that all the samples imaged in TEM had about similar thicknesses, number density of precipitates in MCSE 6082C would be highest, followed by RAM 6082, and then MCSE 6060C (based on total number of precipitates counted in Figure 4.32). The assumption is, however, questionable, as thickness is expected to vary between the samples. If the sample for MCSE 6082C was slightly thicker than RAM 6082, more precipitates would be included in the image and hence more counted. Also, the difference in counted precipitates was not significant, as the image area of MCSE 6082C had only 7 % more precipitates than RAM 6082. Therefore, the difference in number of precipitates is not considered as significant.

The precipitates need to be non-shearable to effectively hinder dislocation motion, and the diameter limit between shearable and non-shearable has been found to be $\sim$3 nm [73]. Manual measurements of images in Figure 4.31 showed that precipitates in all samples were between 3.5 and 5 nm, i.e. they should be non-shearable. It is therefore expected that dislocations bypass the precipitates via the Orowan process [74]. In addition, a difference between the two alloying systems, 6060 and 6082, is expected, as the precipitates (in a Cu-free alloy) are formed from Mg and Si (Section 2.6.4). 6082 has a higher wt% of both Mg and Si and will therefore result in a higher number density of β"-precipitates, given similar ageing conditions.

Although number density of precipitates cannot be inferred from the analysis, MCSE 6060C displayed the lowest number of precipitates counted as well as a distribution more centered around smaller precipitates. The difference, however, between MCSE 6060C and RAM 6082 was not significant, and could explain why MCSE 6060C performed close RAM 6082 in mechanical testing in T6b condition (Figures 4.40–4.42). In a study conducted by Frodal et al. [75], where precipitates in three different alloys were investigated (6060, 6082.25 and 6082.50), the difference in number density of precipitates was clearly visible by inspection of TEM

images alone. In it, they reported ∼7 times higher number density of dispersoids in 6082.25 compared to 6060, a much greater difference than what the images in the present TEM study suggest.

5.3.6 Grain boundary observations

The dispersoids found on grain boundaries in Figure 4.33 are expected for the two 6082 samples and will help preserve the fibrous microsturcture after extrusion (Figure 4.16). In MCSE 6060C there were some particles located along grain boundaries, as shown in Figure 4.33a. EDS analysis (Table D.1) of a similar particle suggests that the it contained mainly Mg and Si, and could therefore be the equilibrium phase Mg_2Si (Table 2.3) precipitated on the grain boundary.

As mentioned in Section 5.3.2, Skorpen [7] found bands of finely dispersed oxide particles on grain boundaries in an Al-10Mg alloy. Although particles in all three samples seemed to contain oxygen (Appendix D), so did the aluminum matrix. Therefore, it is likely that the samples were oxidized prior to investigations in TEM, which caused a thin Al_2O_3-layer on the surface. Moreover, no particles were found to contain a significant amount of oxygen. The results thus suggest that there were no oxides along grain boundaries for all samples investigated.

5.3.7 Mechanical properties

Hardness measurements (Figures 4.34–4.36) showed higher values of RAM 6082 compared to both MCSE 6082C and MCSE 6060C in as-extruded condition. Since the extrudates for RAM 6082 were produced one year prior to the screw extruded samples [63], it is likely an effect from natural ageing. For the tensile tests (Figures 4.37–4.39), results show that MCSE 6060C and MCSE 6082C responded differently to the "Age hardened" condition, i.e. T5 condition. Compared to the as-extruded samples, MCSE 6082C showed only minor increases in mechanical properties (Figure 4.38). As all samples in the present study were air cooled after extrusion, this is due to the quench sensitivity of 6082, explained in Section 2.7.

The significant difference in both yield strength and ultimate tensile strength for MCSE 6082C and RAM 6082 was not expected. As shown by the bar charts in Figures 4.40 and 4.41, the difference between MCSE 6082C and RAM 6082 was consistent across all samples in both T6a and T6b condition. These results should be given some consideration.

The four (main) contributions to strength in aluminium are presented in Section 2.6. First, work hardening is used for metals that do not respond to heat treatment and is not considered to be a factor for the 6xxx alloys. Second, as the grain structure in both 6082 samples were predominantly fibrous (Figure 4.16), the Hall-Petch contribution is considered to be about equal. However, abnormal grains was visible after SSHT and water quenching in RAM 6082 but not in MCSE 6082C (Figure 5.6). This may have lowered the Hall-Petch contribution slightly for RAM 6082, in addition to have caused crystallographic anisotropy and therefore directional dependence on tensile strength. Third, the contribution from elements in solid solution was not investigated, but may be a factor. As mentioned in Section 5.3.4, electrical conductivity tests could reveal differences in solid solution content. Lastly, the difference in both precipitate density and length was discussed in Section 5.3.5. The images in TEM suggested shorter and slightly lower number density of precipitates in RAM 6082 compared to MCSE 6082C. This could explain a small difference in mechanical properties, but not the surprisingly large difference seen here. The possibility of crystallographic anisotropy is further discussed in Section 5.3.8.

Potential sources of error should also be ruled out before reaching a conclusion. When solutionizing and ageing of samples from MCSE 6082C and RAM 6082, care was taken in order to obtain exactly similar (experimental) conditions. Following the labels in Figures 4.38 and 4.39, parallels labeled with the same number in parenthesis, e.g. MCSE 6082C T6a(1) and RAM 6082 T6a(1), were solutionized and aged in similar oil and salth baths, i.e. at the exact same temperature and time. Therefore, there should be no differences in heat treatment. Also, Kristiansen [63] and Fagermo [76], who both studied the similar ram extruded 6082 as in the present study, reported UTS values between 350 and 380 MPa in T6 condition. It can thus be concluded that MCSE 6082C reached its ageing potential while RAM 6082 did not. From an experimental point of view, the reason is not clear, as the heating schedule in Section 3.5.2, both T6a and T6b, allowed MCSE 6082C to reach its ageing potential but not RAM 6082. Kristiansen and Fagermo used, for the similar ram extruded 6082 material, solutionizing temperatures of 550 °C and 530 °C, respectively. This might suggest that the solutionizing temperature of 560 °C was too high for RAM 6082, and therefore initiated recrystallization which caused abnormal grains to form.

Apart from differences in tensile test results compared to RAM 6082, both MCSE 6060C and MCSE 6082C performed in the high-end of what can be expected for both alloys (Figures 2.2 and 2.3). Bilsbak [62] reported similar tensile test results for screw extruded 6060 in T6 condition, while Kristiansen [63] found similar values

for screw extruded 6082 in T6 condition. Therefore, the mechanical properties are yet another proof of concept of what can be achieved from screw extruded material.

5.3.8 Fractography

The spiraling pattern of fracture surfaces from specimens in as-extruded condition (Figure 4.43) has been reported by numerous authors working with screw extrusion of aluminium [62, 77, 78]. The pattern arises from the spiraling motion and subsequent material feeding from the screw, and may represent poor material bonding between the layers. However, the pattern was not reported on samples in T6b condition from the screw extruder, i.e. samples MCSE 6060C T6b and MCSE 6082C T6b in Figure 4.43. It seems likely that the elevated temperatures of solutionizing have initiated enhanced diffusion of atoms, thus achieving sufficient bonding between the spiraling layers from screw extrusion.

Local fracture surfaces in Figure 4.44, as well as supportive images in Appendix G, show typical ductile fractures for all samples, with cup-and-cone features as well as microvoids and dimples. This is expected for ductile materials such as aluminium [33]. Also, the transition towards more shear and faceted fracture surfaces in T6b condition (Figure 4.44) is expected for the aged hardened (and thus more brittle) material. Observations are reflected in the measured area reduction at fracture in Figure 4.45. Here, both MCSE 6060C and MCSE 6082C display a significant decrease from as-extruded to T6b condition, in contrast to the samples from RAM 6082, where area reduction is about similar for as-extruded and T6b condition.

As the tensile specimen of RAM 6082 showed an elliptical fracture surface in T6b condition and circular in as-extruded condition (Figure 4.43), it seems likely that the solutionizing and ageing have caused the elliptical fracture surface. This is also strengthened by the observations in Figure 5.6, where RAM 6082 was the only sample showing abnormal grains, which may have caused the anisotropy. Further, Dieter [33] writes that elliptical deformation of a tensile specimen may be the result of crystallographic anisotropy, and could explain why the specimen experienced large contractions along one of the semi-axes. Despite the fact that only one sample from each condition is presented in Figure 4.43, the elliptical fracture surface was seen in *all six samples* from RAM 6082 in T6 condition (both T6a and T6b). Therefore, the crystallographic anisotropy is most likely the main contributor in lowering the strength of RAM 6082, compared to MCSE 6082C which showed circular fracture surfaces for all six samples in T6 condition.

6 Conclusion

A full microstructural characterization of AA6060 and AA6082 through the metal continuous screw extrusion (MCSE) process has been conducted, from extrusion ingot and feedstock material, to butt sections left in the extrusion chamber and extruded profiles. Microstructure and mechanical properties have been compared to a standard ram extruded AA6082. Main conclusions that can be drawn from the study are summarized below.

- Grain structure evolution through the screw extruder was comparable to a standard ram extrusion, with both shear intensive and dead metal zones.
- A hypothesis for particle fragmentation through the screw extruder could not be confirmed by inspections in LOM alone.
- CO_2 as cover gas during screw extrusion seemed to help lower the porosity in screw extruded profiles of 6082, but not 6060. Other factors, such as temperature and feedstock material (e.g. thickness), were also discussed and are likely to have affected the compacting and amount of porosity.
- Screw extruded material showed a stronger recrystallization resistance compared to the ram extruded sample. This was suggested to be caused by lower strain rates and higher temperatures during deformation for the screw extruded samples.
- Images in SEM revealed between 3 and 9 times higher number density of dispersoids in ram extruded 6082 compared to screw extruded 6082. No satisfactory explanation was found for the surprisingly large difference.
- Screw extruded 6082 outperformed ram extruded 6082 in tensile testing, T6 condition. Precipitate size and distribution were seen in TEM to be about equal, but all ram extruded 6082 samples showed signs of strong crystallographic anisotropy, which was believed to be the main reason causing the difference.
- Screw extruded 6060 and 6082 performed in the high-end of what can be expected of tensile tests for each respective alloy in their classes, and is yet another proof of concept for the screw extrusion technology.

7 Further Work

- Investigate dynamic/static recrystallization through the screw extruder by doing a similar study to that of Güzel et al. [68], where AA6082 was characterized by EBSD at various locations during conventional hot extrusion.
- Build on the model by Skorpen et al. [60] by incorporating strain rate estimates. This would yield valuable information on recrystallization behaviour of screw extruded profiles by calculating the Zener-Hollomon parameter.
- Evolution of intermetallic particles and dispersoids through the screw extruder should be inspected by methods with higher resolution than LOM, such as SEM, and be compared to micrographs in this thesis.
- Perform a thorough EBSD analysis of both ram and screw extruded 6060 to see if differences in fiber structure are similar to those presented in this thesis. That is, a strong <111> and <001> fiber structure in screw extruded 6060, and close to no <111> fibers in ram extruded 6060. Both in as-extruded condition.
- Perform new trials with dispersoid-containing alloys. Investigate if there are any differences in number density of dispersoids by comparing screw and ram extruded profiles.
- Solid solution content in dispersoid-containing, screw extruded material should be inspected by measuring electrical conductivity and compared to ram extruded material.
- Quantify the contribution from precipitates in screw extruded material by doing a thorough investigation in TEM, including thickness measurements (by Electron Energy Loss Spectroscopy) of samples and subsequent number density estimates.
- EBSD scans of screw and ram extruded profiles in T6 condition could reveal any crystallographic anisotropy.

References

[1] R. Lindsey and L. Dahlman, "Climate Change: Global Temperature." https://www.climate.gov/news-features/understanding-climate/climate-change-global-temperature. Accessed: March 2021.

[2] U. N. F. C. on Climate Change, "The Paris Agreement." https://unfccc.int/process-and-meetings/the-paris-agreement/the-paris-agreement. Accessed: March 2021.

[3] Hydro, "Lifting profitability, driving sustainability." https://www.hydro.com/no-NO/investorer/reports-and-presentations/annual-reports/annual-report-2019/letter-to-shareholders/. Accessed: March 2021.

[4] J. Werenskiold, L. Auran, H. J. Roven, N. Ryum, and O. Reiso, "Screw extruder for continuous extrusion of materials with high viscosity." International patent publ. no. WO2008/063076, 2008.

[5] J. R. Duflou, A. E. Tekkaya, M. Haase, T. Welo, K. Vanmeensel, K. Kellens, W. Dewulf, and D. Paraskevas, "Environmental assessment of solid state recycling routes for aluminium alloys: Can solid state processes significantly reduce the environmental impact of aluminium recycling?," *CIRP Annals - Manufacturing Technology*, vol. 64, no. 1, pp. 37–40, 2015.

[6] F. Widerøe, *Material flow in screw extrusion of aluminium*. PhD thesis, NTNU, Trondheim. Faculty of Natural Sciences and Technology, Department of Materials Science and Engineering, 2012.

[7] K. G. Skropen, *Screw Extrusion of Light Metals - Development of materials, characterization and process analysis*. PhD thesis, NTNU, Trondheim. Faculty of Natural Sciences and Technology, Department of Materials Science and Engineering, 2018.

[8] Norsk Hydro, "Groundbreaking recycling pilot technology in pilot phase." https://www.hydro.com/en-NO/media/news/2021/groundbreaking-recycling-technology-in-pilot-phase/. Accessed: March 2021.

[9] NUVOSIL. https://nuvosil.com. Accessed: March 2021.

[10] O. Sveen, "Characterization of the microstructural development through screw extrusion of aluminium alloys AA6060 and AA6082." Specialization Project, Department of Materials Science and Engineering, NTNU, 2020.

[11] O. Reiso and B. Holmedal, "Extrusion and Al Metallurgy." Lecture notes, NTNU, 2020.

[12] J. K. Solberg, *Teknologiske metaller og legeringer*, pp. 191–243. Institutt for materialteknologi: NTNU, 2017.

[13] J. Zhang, Z. Fan, Y. Q. Wang, and B. L. Zhou, "Equilibrium pseudobinary Al–Mg2Si phase diagram," *Materials Science and Technology*, vol. 17, no. 5, pp. 494–496, 2001.

[14] Norsk Hydro, "Technical datasheet - Extruded products, Alloy EN AW-6082 [AlSi1MgMn] ." `https://www.hydro.com/Document/Index?name=Hydro%20EN%20AW%206082.PDF&id=7824`. Accessed: March 2021.

[15] L. Lodgaard, *Precipitation of dispersoids containing Mn and/or Cr in Al-Mg-Si alloys*. PhD thesis, NTNU, Trondheim, 2000.

[16] X. Qian, N. Parson, and X.-G. Chen, "Effects of Mn content on recrystallization resistance of AA6082 aluminum alloys during post-deformation annealing," *Journal of Materials Science & Technology*, vol. 52, pp. 189–197, 2020.

[17] R. Hu, T. Ogura, H. Tezuka, T. Sato, and Q. Liu, "Dispersoid Formation and Recrystallization Behavior in an Al-Mg-Si-Mn Alloy," *Journal of Materials Science & Technology*, vol. 26, no. 3, pp. 237–243, 2010.

[18] Norsk Hydro, "Technical datasheet - Extruded products, Alloy EN AW-6060 [AlMgSi]." `https://www.hydro.com/Document/Index?name=Hydro%20EN%20AW%206060.PDF&id=7822`. Accessed: March 2021.

[19] B. Verlinden, *Thermo-Mechanical Processing of Metallic Materials*. Elsevier Science, 2007.

[20] T. Sheppard, *Extrusion of Aluminium Alloys*. Department of Product Design and Manufacture, Bournemouth University: Kluwer Academic Publishers, 1999.

[21] T. Furu and K. Pedersen, "The influence of grain structure and texture on formability and toughness of extruded aluminium alloys," *Materials Science Forum*, vol. 519–521, pp. 1421–1428, 2006.

[22] J. Humphreys, G. S. Rohrer, and A. Rollett, *Recrystallization and Related Annealing Phenomena*. Oxford: Elsevier, third ed., 2017.

[23] F. J. Humphreys, "A unified theory of recovery, recrystallization and grain growth, based on the stability and growth of cellular microstructures—I. The basic model," *Acta Materialia*, vol. 45, no. 10, pp. 4231–4240, 1997.

[24] W. D. Callister and D. G. Rethwisch, *Materials Science and Engineering*, pp. 272–281. Wiley, 9th ed., 2015.

[25] K. Zhang, T. Pettersen, C. Paulsen, K. Marthinsen, B. Holmedal, and A. Segatori, "Recrystallization behaviour of AA6063 extrusions," *IOP Conf. Ser.: Mater. Sci. Eng.*, vol. 89, p. 012057, 2015.

[26] C. Zener and J. H. Hollomon, "Effect of Strain Rate Upon Plastic Flow of Steel," *Journal of Applied Physics*, vol. 15, no. 22, 1944.

[27] P. Feltham *Metal Treatment*, vol. 23, pp. 440–44, 1956.

[28] B. Rinderer, "The Metallurgy of Homogenisation," in *Aluminium Cast House Technology XII*, vol. 693 of *Materials Science Forum*, pp. 264–275, Trans Tech Publications Ltd, 2011.

[29] N. A. Belov, A. A. Aksenov, and D. G. Esking, *Iron in aluminium alloys: impurity and alloying element.* 11 New Fetter Lane, London EC4P 4EE: Taylor & Francis, 1st ed., 2002.

[30] K. Ito, R. Musick, and K. Lücke, "The influence of iron content and annealing temperature on the recrystallization textures of high-purity aluminium-iron alloys," *Acta Metallurgica*, vol. 31, no. 12, pp. 2137–2149, 1983.

[31] Y. L. Liu and S. B. Kang, "The solidification process of Al-Mg-Si alloys," *Journal of Materals Science*, vol. 32, no. 6, pp. 1443–1447, 1997.

[32] Y. L. Liu, S. B. Kang, and H. W. Kim, "The complex microstructures in an as-cast Al–Mg–Si alloy," *Materials Letters*, vol. 41, no. 6, pp. 267–272, 1999.

[33] G. E. Dieter and D. Bacon, *Mechanical Metallurgy.* London: McGraw-Hill, SI Metric ed., 1988.

[34] O. R. Myhr, Ø. Grong, and S. J. Andersen, "Modelling the age hardening behaviour of Al-Mg-Si alloys," *Acta Mater.*, vol. 49, pp. 65–75, 2001.

[35] O. R. Myhr, Ø. Grong, and H. G. Fjær, "Modelling of the microstructure and strength evolution in Al-Mg-Si alloys during multistage processing," *Acta Mater.*, vol. 52, pp. 4997–5008, 2004.

[36] E. O. Hall *Proc. Phys. Soc. London*, vol. 64, p. 747, 1951.

[37] N. J. Petch *J. Iron Steel Inst. London*, vol. 173, p. 25, 1953.

[38] K. Matsuda, Y. Sakaguchi, Y. Miyata, Y. Uetani, T. Sato, A. Kamio, and S. Ikeno, "Precipitation sequence of various kinds of metastable phases in Al-1.0mass% Mg2Si-0.4mass% Si alloy," *Journal of Materials Science*, vol. 35, no. 1, pp. 179–189, 2000.

[39] C. D. Marioara, S. J. Andersen, H. W. Zandbergen, and R. Holmestad, "The Influence of Alloy Composition on Precipitates of the Al-Mg-Si System," *Metallurgical and Materials Transactions*, vol. 36A, no. 3, pp. 691–702, 2005.

[40] C. D. Marioara, H. Nordmark, S. J. Andersen, and R. Holmestad, "Post-phases and their influence on microstructure and hardness in 6xxx Al-Mg-Si alloys," *Journal of Materials Science*, vol. 41, no. 2, pp. 471 – 478, 2006.

[41] Ø. Grong, "Recent Advances in Solid-State Joining of Aluminium," *Welding Journal*, vol. 91, no. 1, pp. 26–33, 2012.

[42] S. J. Andersen, H. W. Zandbergen, J. Jansen, C. Træholt, U. Tundal, and O. Reiso, "The crystal structure of the β" phase in Al–Mg–Si alloys," *Acta Materialia*, vol. 46, no. 9, pp. 3283–3298, 1998.

[43] S. J. Andersen, C. D. Marioara, R. Vissers, A. Frøseth, and H. W. Zandbergen, "The structural relation between precipitates in Al-Mg-Si alloys, the Al-matrix and diamond silicon, with emphasis on the trigonal phase U1-MgAl2Si2," *Materials Science and Engineering A*, vol. 444, pp. 157–169, 2007.

[44] R. Vissers, M. A. van Huis, J. Jansen, H. W. Zandbergen, C. D. Marioara, and S. J. Andersen, "The crystal structure of the β' phase in Al-Mg-Si alloys," *Acta Materialia*, vol. 55, no. 11, pp. 3815–3823, 2007.

[45] S. J. Andersen, C. D. Marioara, A. Frøseth, R. Vissers, and H. W. Zandbergen, "Crystal structure of the orthorombic U2-Al4Mg4Si4 precipitate in Al-Mg-Si alloy system and its relation to the β' and β" phases," *Materials Science and Engineering A*, vol. 390, no. 1–2, pp. 127–138, 2005.

[46] R. Vissers, C. D. Marioara, S. J. Andersen, and R. Holmestad, "Crystal structure determination of the B' phase in Al-Mg-Si alloys by combining quantitative electron diffraction and ab initio calculations," in *Aluminium Alloys. Their Physical and Mechanical Properties*, pp. 1263–1269, Weinheim, Germany: Wiley-VCH, 2008.

[47] B. Holmedal, "Strength contribution from precipitates," *Phil. Mag. Lett.*, vol. 95, no. 12, pp. 594–601, 2015.

[48] O. Lohne and A. L. Dons *Scand. J. Met.*, p. 34, 1983.

[49] K. Surla, F. Valdivieso, M. Pijolat, M. Soustelle, and M. Prin, "Kinetic study of the oxidation by oxygen of liquid Al-Mg 5% alloys," *Solid State Ionics*, vol. 143, no. 3, pp. 355–365, 2001.

[50] D. L. Belitskus, "Oxidation of molten Al-Mg alloy in air, air-SO_2, and air-H_2S atmospheres," *Oxid Met*, vol. 3, no. 4, pp. 313–317, 1971.

[51] C. N. Cochran, B. D. L, and D. L. Kinosz, "Oxidation of aluminum-magnesium melts in air, oxygen, flue gas, and carbon dioxide," *MTB*, vol. 8, no. 1, pp. 323–332, 1977.

[52] N. Smith, S. Wissam, B. Gleeson, A. Kvithyld, and G. Tranell, "The Mechanism Behind the Oxidation Protection of High Mg Al Alloys with Beryllium," *Met. Trans B*, 2018.

[53] W. Thiele, "Die Oxydation von Aluminium-und Aluminiumlegierungsschmelzen," *Aluminium*, vol. 38, pp. 780–786, 1962.

[54] N. Smith, B. Gleeson, W. A. Saidi, A. Kvithyld, and G. Tranell, "Effects of CO_2 cover gas and yttrium additions on the oxidation of AlMg alloys," *Light Metals 2019*, pp. 1025–1032, 2019.

[55] C. K. W. Solem, K. E. Ekstrøm, G. Tranell, and R. E. Aune, "Evaluation of the Effect of CO_2 Cover Gas on the Rate of Oxidation of an AlMgSi Alloy," *Light Metals 2020*, pp. 1141–1147, 2020.

[56] N. Smith, B. Gleeson, W. A. Saidi, A. Kvithyld, and G. Tranell, "Mechanism behind the Inhibiting Effect of CO_2 on the Oxidation of Al-Mg Alloys," *Ind. Eng. Chem. Res.*, vol. 58, no. 3, pp. 1434–1442, 2019.

[57] K. Wefers, "Properties and characterization of surface oxides on aluminium alloys," *Aluminium*, vol. 57, pp. 722–726, 1987.

[58] G. K. Sigworth, *Best Practices in Aluminium Metalcasting*. Schaumburg IL: American Foundry Society, 2014.

[59] F. Widerøe and T. Welo, "Using contrast material techniques to determine metal flow in screw extrusion of aluminium," *Journal of Materials Processing Technology*, vol. 213, no. 7, pp. 1007–1008, 2013.

[60] K. G. Skorpen, H. J. Roven, and O. Reiso, "A physical based empirical model for the accumulated strain in novel Metal Continuous Screw Extrusion (MCSE)," *Journal of Materials Processing Technology*, vol. 282, p. 116670, 2020.

[61] O. Ragnvaldsen, "Characterisation of an aluminium matrix nanocomposite wire manufactured by screw extrusion," Master's thesis, NTNU, Trondheim, 2019.

[62] A. Bilsbak, "Mikrostruktur og mekaniske egenskaper for skrueekstrudert aluminium," Master's thesis, NTNU, Trondheim, 2012.

[63] K. H. Kristiansen, "Characterization of extruded aluminium alloys from ram extrusion and screw extrusion," Master's thesis, NTNU, Trondheim, 2020.

[64] G. Langelandsvik, M. Grandcolas, K. G. Skorpen, T. Furu, O. M. Akselsen, and H. J. Roven, "Development of Al-TiC Wire Feedstock for Additive Manufacturing by Metal Screw Extrusion," *Metals*, vol. 10, no. 11, 2020.

[65] G. Langelandsvik, "Optimization of Electrical Conductivity in Screw Extruded Wires," Master's thesis, NTNU, Trondheim, 2017.

[66] M. Easton and D. StJohn, "An analysis of the relationship between grain size, solute content, and the potency and number density of nucleant particles," *Metallurgical and Materials Transactions A*, vol. 36, pp. 1911–1920, 2005.

[67] A. S. Hjorth, "The Effect of Deformation by Torsion and Subsequent Heat Treatment on the Microstructure of AA6082," Master's thesis, NTNU, Trondheim, 2018.

[68] A. Güzel, A. Jäger, F. Parvizian, H.-G. Lambers, A. E. Tekkaya, B. Svendsen, and H. J. Maier, "A new method for determining dynamic grain structure evolution during hot aluminium extrusion," *Journal of Materials Processing Technology*, vol. 212, no. 1, pp. 323–330, 2012.

[69] P. Szczygiel, H. J. Roven, and O. Reiso, "On the effect of SPD on recycled experimental aluminium alloys: Nanostructures, particle break-up and properties," *Materials Science and Engineering A*, vol. 410, pp. 261–264, 2005.

[70] P. Szczygiel, H. J. Roven, C. Simensen, and O. Reiso, "Microstructural development of "recycled-like" alloys during ECAP: Particle break-up, microstructure evolution and mechanical properties," *TMS Annual Meeting*, pp. 257–262, 2006.

[71] T. Sakai, A. Belyakov, R. Kaibyshev, H. Miura, and J. J. Jonas, "Dynamic and post-dynamic recrystallization under hot, cold and severe plastic deformation," *Progress in Materials Science*, vol. 60, pp. 130–207, 2014.

[72] F. Kutner, "Aluminium conductor materials," *Aluminium- Verlag GmbH*, pp. 15–27, 1981.

[73] W. J. Poole, X. Wang, D. J. Lloyd, and J. D. Embury, "The shearable-non-shearable transition in Al-Mg-Si-Cu precipitation hardening alloys: implications on the distribution of slip, work hardening and fracture," *Philosophical Magazine*, vol. 85, no. 26–27, pp. 3113–3135, 2005.

[74] E. Orowan, "Symposium on Internal Stress." Institute of Metals, London, 1947.

[75] B. H. Frodal, E. Christiansen, O. R. Myhr, and O. S. Hopperstad, "The role of quench rate on the plastic flow and fracture of three aluminium alloys with different grain structure and texture," *International Journal of Engineering Science*, vol. 150, no. 26–27, p. 103257, 2020.

[76] M. M. Fagermo, "The Use Of Aluminium in Sustainable Concrete Structures," Master's thesis, NTNU, Trondheim, 2020.

[77] T. Berulfsen, "Screw Extrusion from various Binary Al-XMg Feed Materials," Master's thesis, NTNU, Trondheim, 2016.

[78] T. J. Stedje, "Characterization of Screw Extruded Rapid Solidified AA6061," Master's thesis, NTNU, Trondheim, 2014.

Appendices

A Temperature logs from screw extrusion

Positions of thermocouples during screw extrusion are shown in Figure A.1. Figures A.2–A.5 show the temperature as a function of time during screw extrusion of MCSE 6060, MCSE 6082, MCSE 6060C and MCSE 6082C.

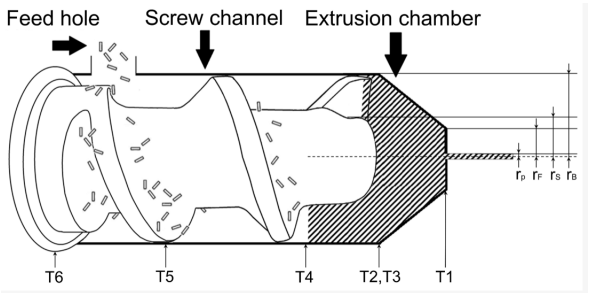

Figure A.1: A principal sketch of the metal screw extrusion process showing positions of thermocouples, labeled T1-T6. From [64].

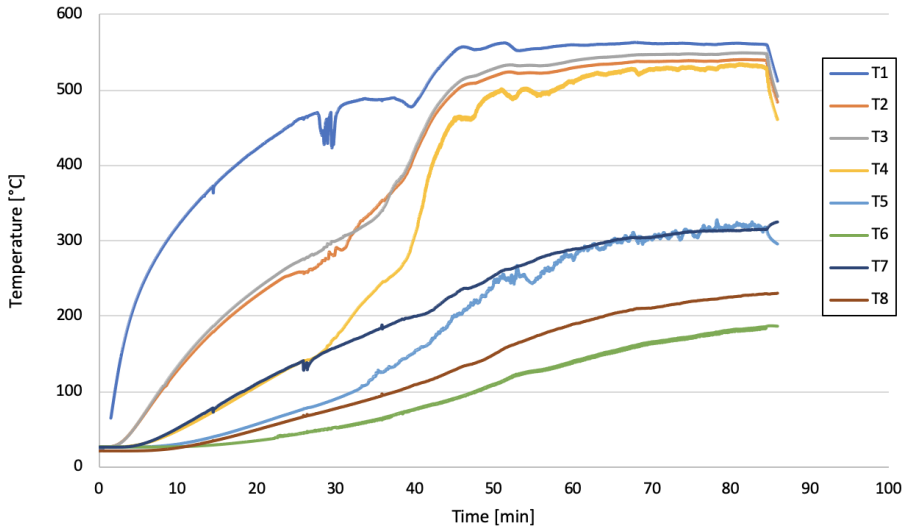

Figure A.2: Temperature during screw extrusion of MCSE 6060. Positions of thermocouples T1 through T6 are shown in Figure A.1. T7 is in a similar position as T5, while T8 is in a similar position as T6.

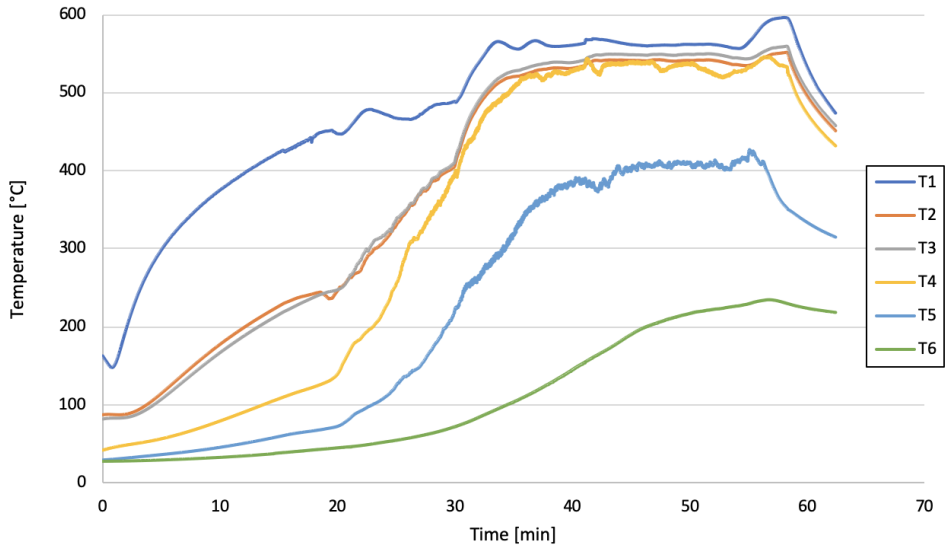

Figure A.3: Temperature during screw extrusion of MCSE 6082. Positions of thermocouples T1 through T6 are shown in Figure A.1.

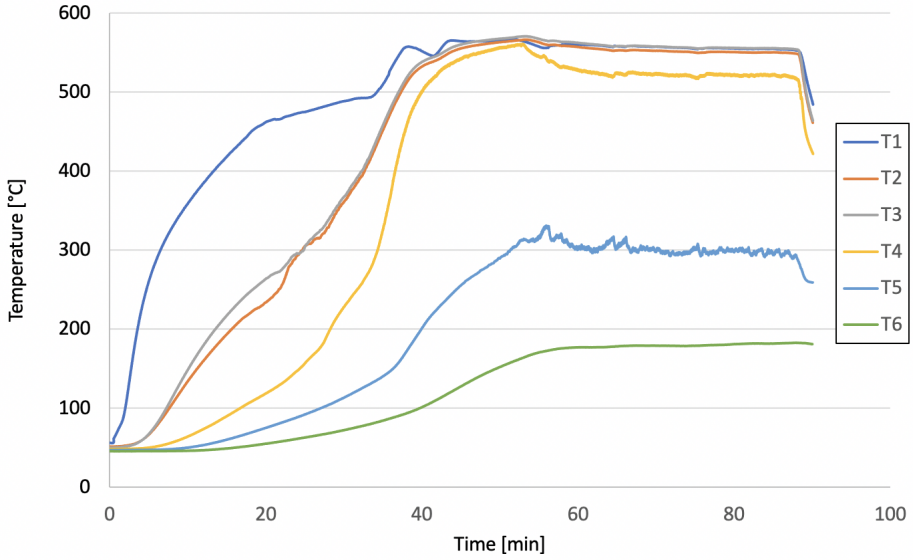

Figure A.4: Temperature during screw extrusion of MCSE 6060C. Positions of thermocouples T1 through T6 are shown in Figure A.1.

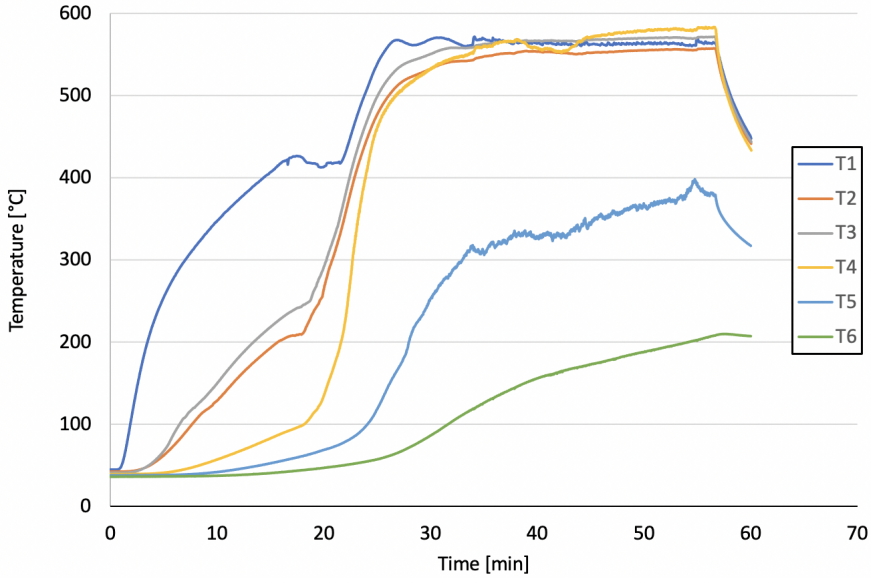

Figure A.5: Temperature during screw extrusion of MCSE 6082C. Positions of thermocouples T1 through T6 are shown in Figure A.1.

B Cutting of samples from screw plug – a detailed step-by-step guide

The following step-by-step guide was created during the project work leading up to the master's thesis [10]. ***Plug 6082*** *refers to an aluminium plug retrieved from screw extrusion trials during the project work, i.e. trials with ambient air atmosphere.*

First, a series of simple sketches of the plugs were made. As a basis for the drawings, approximate measurements from Plug 6082 were used, as seen in Figure B.1.

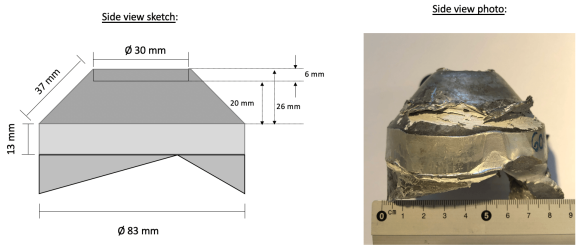

(a) Side view.

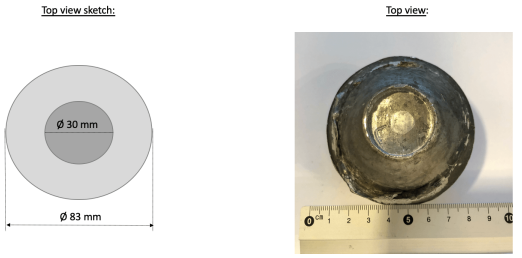

(b) Top view.

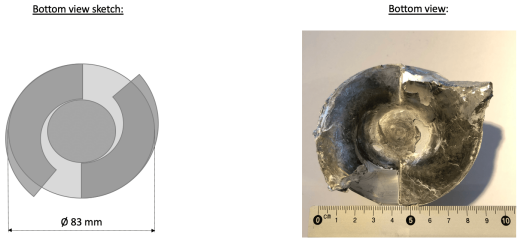

(c) Bottom view.

Figure B.1: Sketches of Plug 6082.

The first cut was made along Plane A, as indicated in Figure B.2.

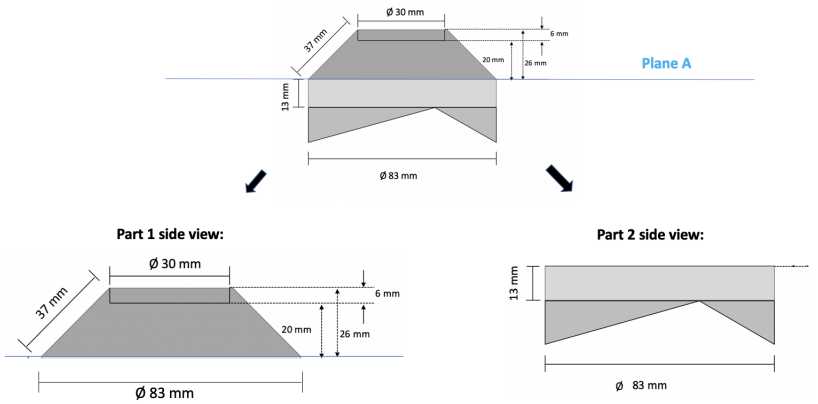

Figure B.2: First cut in plug.

The second and third cut were made on Part 1, as indicated in Figure B.3. The middle piece (indicated by red arrow) was further cut into smaller samples.

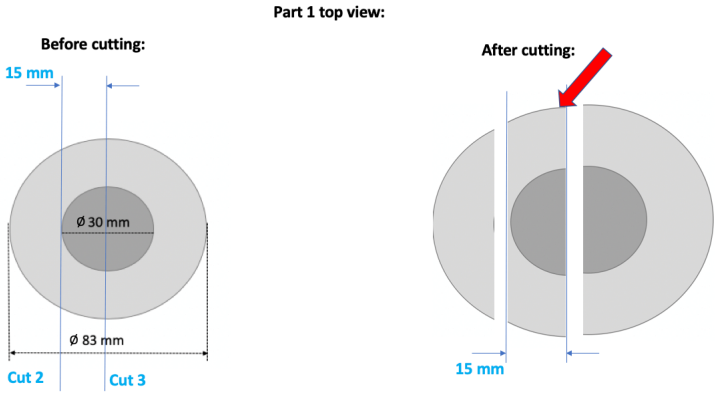

Figure B.3: Second and third cut in plug. The red arrow indicates which part was further cut in next steps.

Using the part indicated by a red arrow in Figure B.3, three samples were taken out for further metallographic preparation. These are shown in Figure B.4 and were labeled Sample 1, 2 and 3.

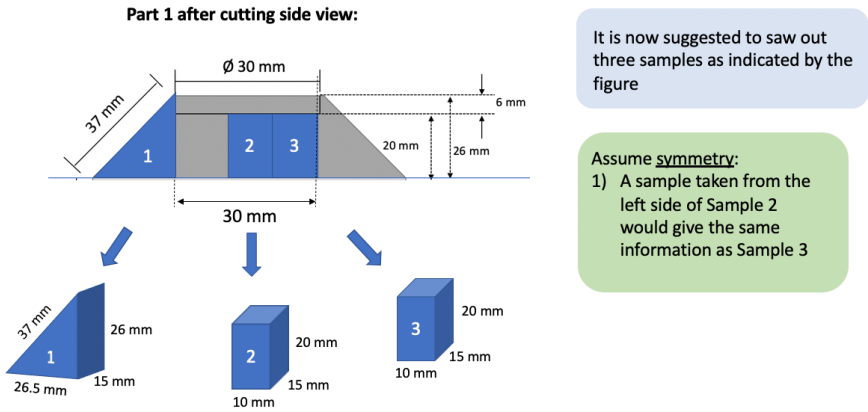

Figure B.4: Three samples taken out from Part 1.

Next, a method for performing cuts in the screw channel (Part 2 in Figure B.2) is suggested:

1. Every plug from the double flight screw extruder has two flights. Starting point for measurements is at the beginning of each of them, i.e. 0 mm.
2. Based on which flight is least deformed, start from either Starting point A or Starting point B (see Figure B.5)
3. Using a measuring tape (or any other tool), follow the chosen flight along the surface.
4. Perform cuts at appropriate intervals.
5. Extract pieces of whatever sizes fit your inspection needs and/or instruments.
6. Be aware of the extrusion direction at all times.
7. If the plug has a lot of material from the screw channel, several more cuts can be defined by following the screw channel with measuring tape and defining cuts.

Pieces that were extracted from the screw channel following the steps above were labeled Sample 4. If the plug allowed for more than one sample to be cut from the screw channel, these were labeled Sample 4.1, 4.2, 4.3, etc., and properly measured from the reference starting point.

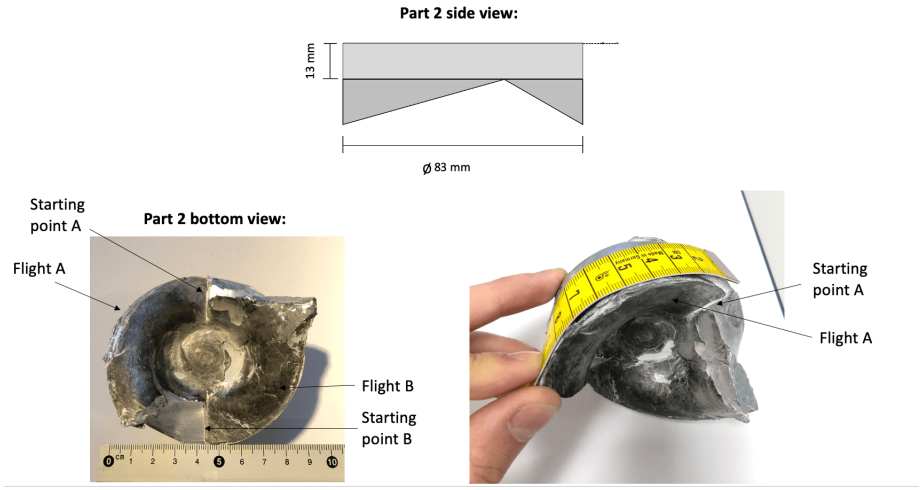

Figure B.5: Reference system for cuts along the screw channel.

Lastly, two pieces were cut out from part 2. These were labeled Sample 5 and 6, and can be shown in Figure B.6.

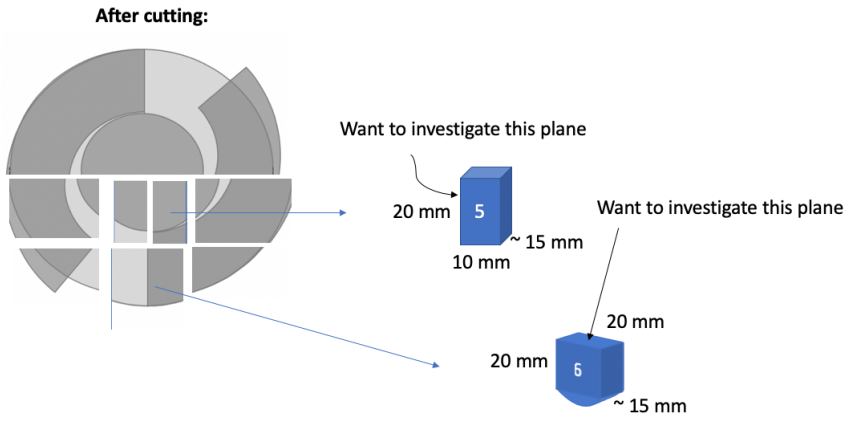

Figure B.6: Two samples taken out from Part 2.

C Particle analysis program

The particle analysis program was created by PhD student Håkon Wiik Ånes at NTNU, Department of Materials Science and Engineering. A brief description of the software will be given here, while the full script is available at GitHub.

Step 1: Import BSE image from SEM.

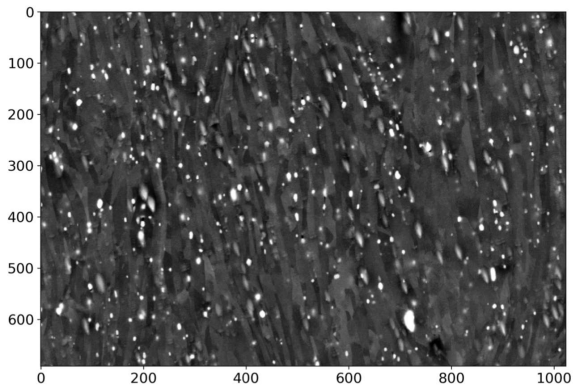

Figure C.1: BSE image from SEM. Acquired by Eirik Bugten Hamnes at NTNU.

Step 2: Convert image to grayscale and 8 bit, inspect image.

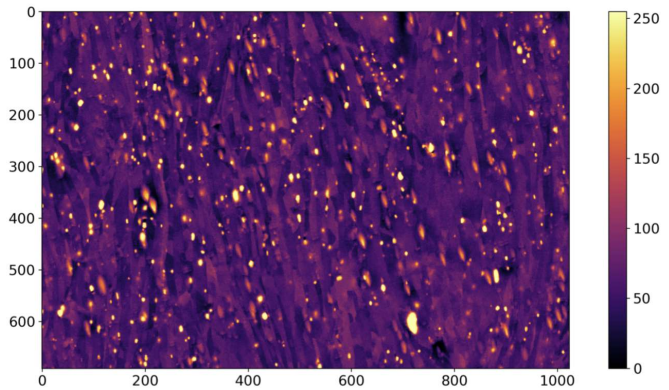

Figure C.2: Grayscale and 8 bit image.

Step 3: Create an elevation map with particle edges highlighted.

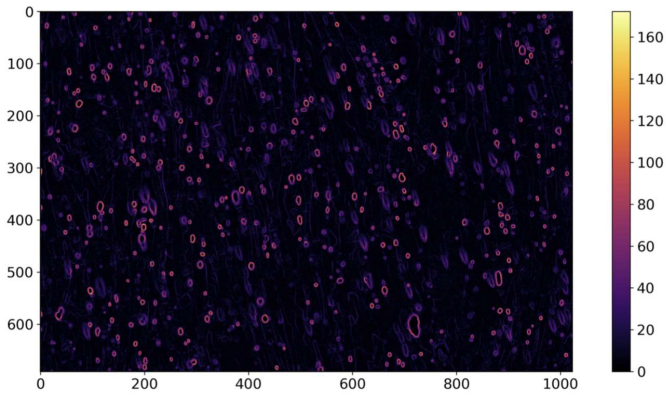

Figure C.3: Elevation map.

Step 4: Find markers of each particle and the background.

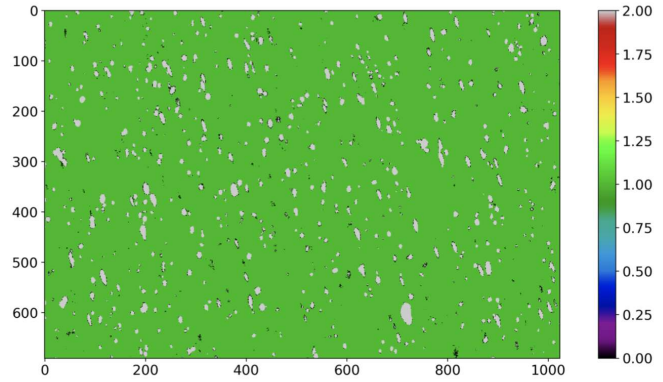

Figure C.4: Particles separated form the matrix.

Step 5: Perform a watershed transformation by flooding the elevation map starting from the markers.

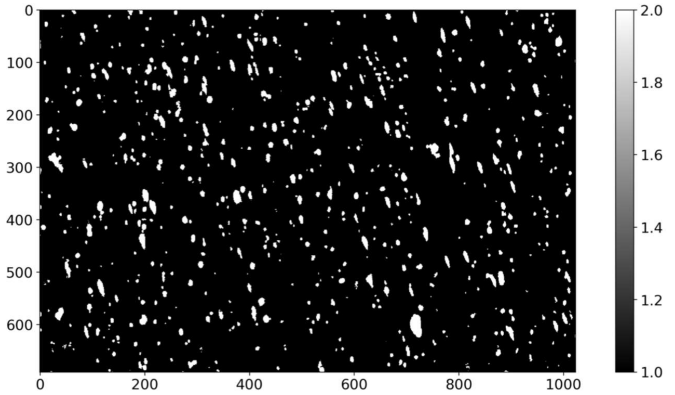

Figure C.5: Binary image separating particles and matrix.

Step 6: Segment particles from binary image.

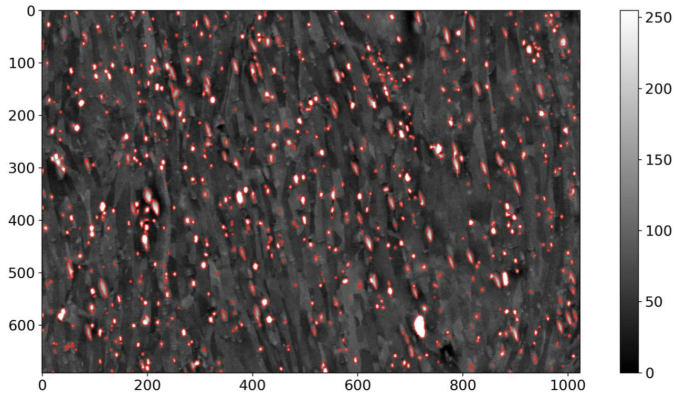

Figure C.6: Segmented particles imported onto original BSE image.

Step 7: Acquire particle properties. Remove wrongly segmented particles and confirm successful transformation.

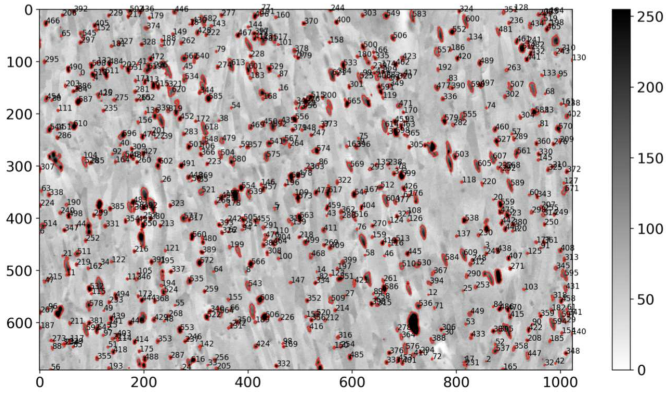

Figure C.7: Grayscale image with counted particles.

Step 8: Plot histogram showing particle distribution. Calculate particle density and particle area.

D EDS analysis from TEM

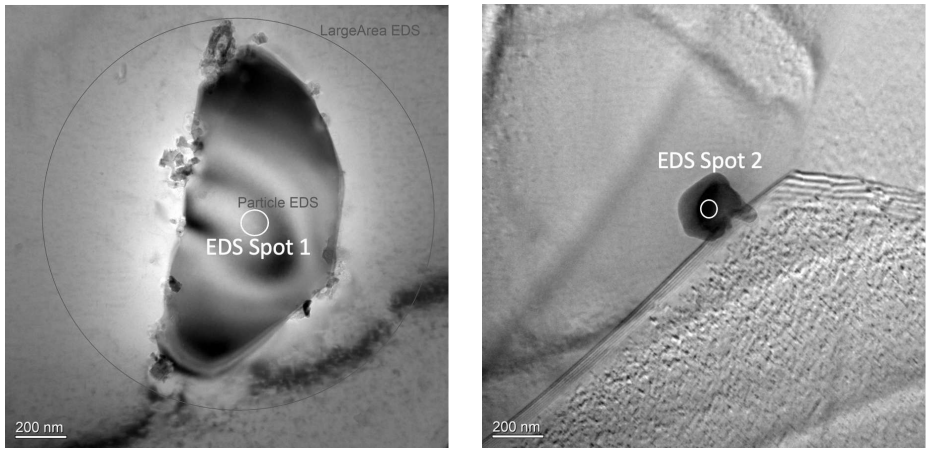

(a) EDS Spot 1. **(b)** EDS Spot 2.

Figure D.1: TEM image of particles in MCSE 6060C, T6b condition.

Table D.1: EDS analysis from Figure D.1.

	Chemical element (wt.%)						
EDS Spot #	Al	Fe	Si	Mg	Mn	Cr	O
1	62.53	22.32	6.90	-	0.55	-	5.48
2	86.32	0.13	6.28	3.73	-	-	3.21

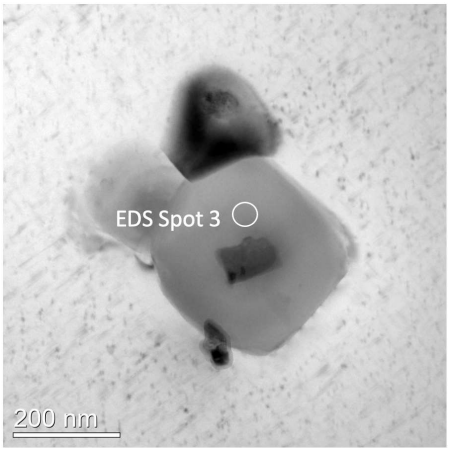

(a) EDS Spot 3.

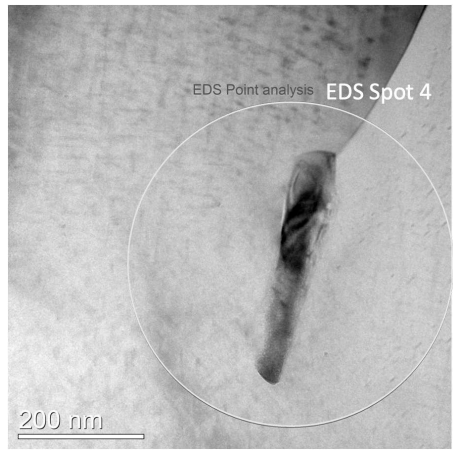

(b) EDS Spot 4.

Figure D.2: TEM image of particles/dispersoids in MCSE 6082C, T6b condition.

Table D.2: EDS analysis from Figure D.2.

	Chemical element (wt.%)						
EDS Spot #	Al	Fe	Si	Mg	Mn	Cr	O
3	62.61	5.23	10.08	-	14.99	4.72	2.01
4	94.56	-	2.22	1.46	0.07	-	1.07
Matrix	98.28	-	-	-	-	-	1.56

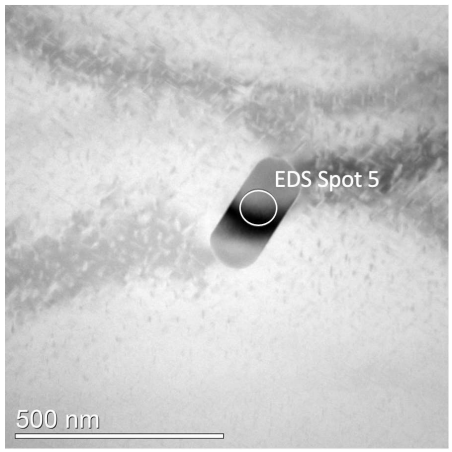

(a) EDS Spot 5.

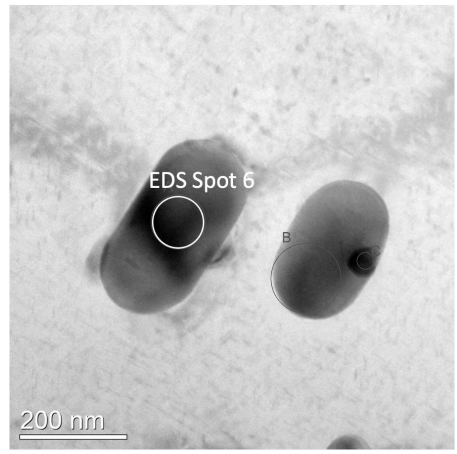

(b) EDS Spot 6.

Figure D.3: TEM image of particles/dispersoids in RAM 6082, T6b condition.

Table D.3: EDS analysis from Figure D.3.

	Chemical element (wt.%)						
EDS Spot #	Al	Fe	Si	Mg	Mn	Cr	O
5	59.65	6.60	10.49	-	14.97	5.00	2.68
6	60.55	5.73	10.64	-	15.81	4.67	2.25
Matrix	94.99	-	-	-	-	-	4.53

E Hardness measurements

Numerical values collected from hardness measurements are listed in Tables E.1–E.3. In the tables, LC = "Longitudinal cross section" and TC = "Transverse cross section". Numbers 1, 2 and 3 indicate positions of hardness indentations, 1 being 0.2 mm from the outer layer, 2 being 2.5 mm from the outer layer, and 3 being 5 mm from the outer layer, i.e. in the middle of the sample (Figure 3.12).

Table E.1: Hardness measurements (HV1) of MCSE 6060C, as-extruded condition.

Measurement no.	LC 1	LC 2	LC 3	TC 1	TC 2	TC3
1	41.47	45.75	42.35	40.31	44.37	41.45
2	41.88	44.47	43.06	42.02	44.14	44.68
3	42.08	45.28	42.07	40.66	44.83	41.25
4	42.58	45.92	43.32	41.39	43.50	40.87
5	39.65	46.62	41.20	41.66	44.14	44.12

Table E.2: Hardness measurements (HV1) of MCSE 6082C, as-extruded condition.

Measurement no.	LC 1	LC 2	LC 3	TC 1	TC 2	TC3
1	48.06	47.13	47.05	49.28	47.98	49.6
2	47.76	46.05	47.24	48.40	47.30	47.19
3	49.44	46.41	46.25	46.96	48.11	47.52
4	49.11	46.81	47.70	46.60	47.08	47.05
5	49.11	47.39	46.60	46.06	47.11	47.18

Table E.3: Hardness measurements (HV1) of MCSE 6060C, as-extruded condition.

Measurement no.	LC 1	LC 2	LC 3	TC 1	TC 2	TC3
1	65.23	61.02	63.27	63.57	63.15	63.36
2	61.61	60.76	62.38	66.55	63.27	61.70
3	67.67	61.56	63.66	67.55	60.48	63.89
4	68.33	61.78	63.34	66.40	62.65	62.34
5	68.80	61.94	61.65	68.80	62.38	62.79

F Tensile test results

Numerical values collected from tensile test results are listed in Tables F.1–F.3.

Table F.1: Results from tensile tests of MCSE 6060C.

Sample	σ_f [MPa]	σ_u [MPa]	ε_f [%]
As-extruded (1)	68.6	157.2	27.7
As-extruded (2)	68.1	154.6	26.3
As-extruded (3)	66.8	154.2	25.5
As-extruded (4)	66.7	155.5	27.5
Age hardened (1)	135.3	184.4	22.2
Age hardened (2)	132.6	182.3	21.1
Age hardened (3)	137.8	185.8	17.6
T6a (1)	245.2	265.6	16.3
T6a (2)	242.4	262.2	15.6
T6a (3)	241.9	262.6	18.0
T6b (1)	262.5	284.2	11.5
T6b (2)	265.9	287.9	16.0
T6b (3)	265.8	283	12.8

Table F.2: Results from tensile tests of MCSE 6082C.

Sample	σ_f [MPa]	σ_u [MPa]	ε_f [%]
As-extruded (1)	69.1	170.0	29.1
As-extruded (2)	70.1	171.3	29.4
As-extruded (3)	68.5	170.6	28.2
As-extruded (4)	69.7	170.9	28.2
Age hardened (1)	92.8	173.2	23.7
Age hardened (2)	98.2	176.7	25.0
Age hardened (3)	96.4	175.5	25.9
T6a (1)	334.4	348.5	16.7
T6a (2)	332.2	345.9	15.6
T6a (3)	333.1	347.8	16.0
T6b (1)	354.8	371.0	17.0
T6b (2)	344.2	362.9	13.4
T6b (3)	335.2	353.0	16.8

Table F.3: Results from tensile tests of RAM 6082.

Sample	σ_f [MPa]	σ_u [MPa]	ε_f [%]
As-extruded (1)	114.1	206.6	20.9
As-extruded (2)	106.9	194.5	20.2
As-extruded (3)	118.7	210.6	23.1
As-extruded (4)	118.4	212.8	23.6
T6a (1)	282.5	290.4	13.7
T6a (2)	288.2	290.8	10.8
T6a (3)	286.8	293.3	17.8
T6b (1)	271.5	286.6	16.2
T6b (2)	282.9	309.0	17.9
T6b (3)	281.1	298.3	17.6

G Fractography - additional images

Figures G.1–G.6 show representative images of fracture occurrence after tensile testing. Specimens shown here are the same ones investigated in SEM and presented in Section 4.4.5. Figures G.7–G.9 highlight features and details of the fractured specimens in SEM.

Figure G.1: MCSE 6060C as-extruded, fracture occurrence.

Figure G.2: MCSE 6060C T6b, fracture occurrence.

Figure G.3: MCSE 6082C as-extruded, fracture occurrence.

Figure G.4: MCSE 6082C T6b, fracture occurrence.

Figure G.5: RAM 6082 as-extruded, fracture occurrence.

Figure G.6: RAM 6082 T6b, fracture occurrence.

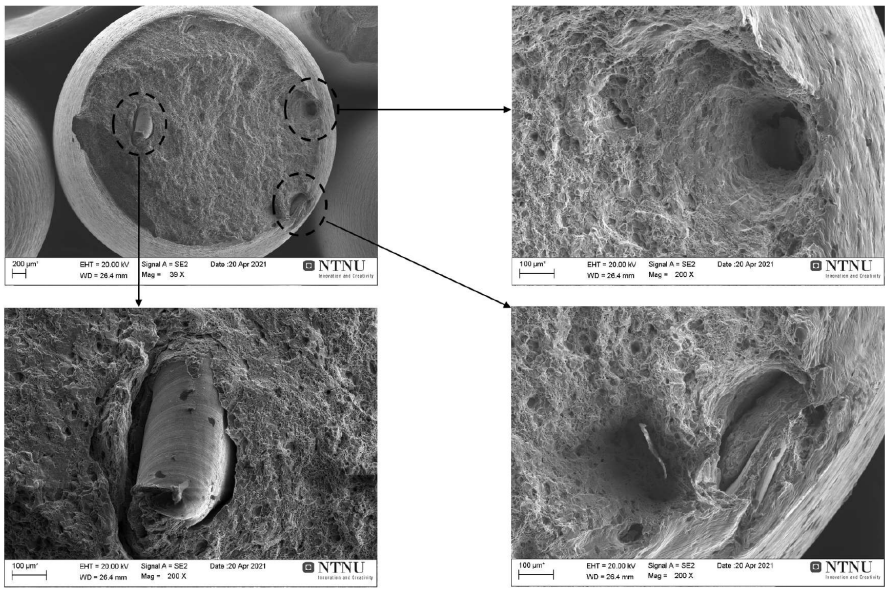

Figure G.7: MCSE 6060C T6b, fracture surface. A large impurity as well as holes in the fracture surface can be seen.

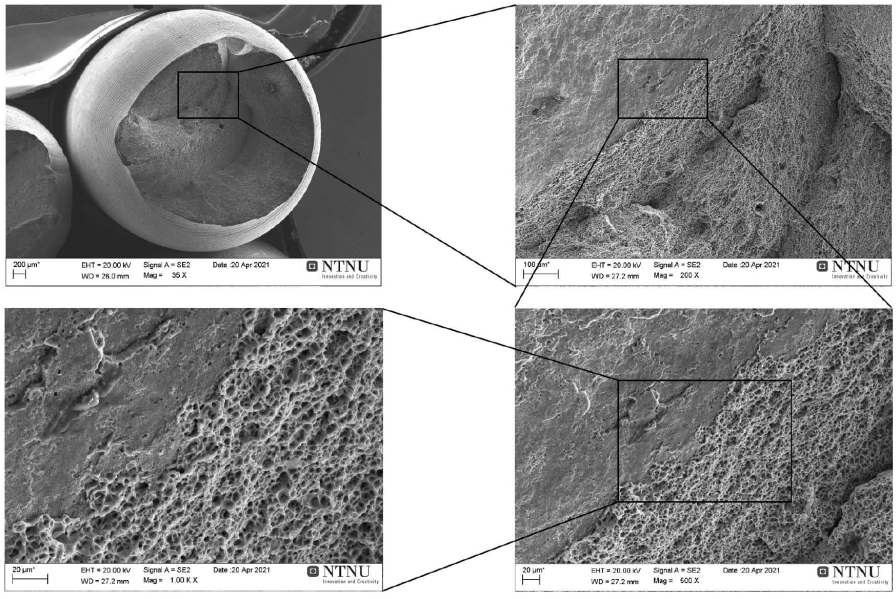

Figure G.8: RAM 6082 as-extruded, fracture surface. A transition from microvoids to a faceted shearing fracture can be seen. This area was most likely the last part to separate and thus experienced a rapid fracture occurrence, causing the transition.

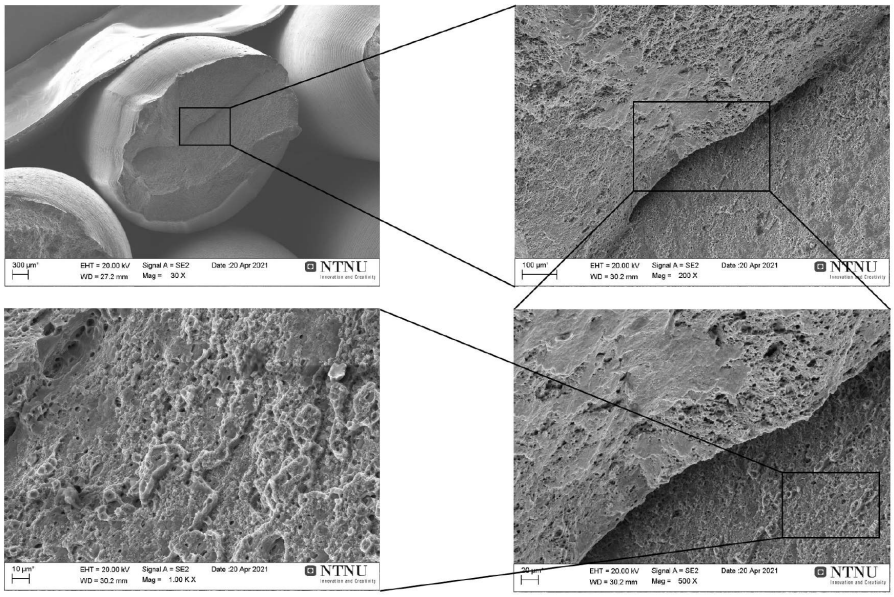

Figure G.9: RAM 6082 T6b, fracture surface. Two faceted surfaces meet in the middle of the fracture surface.

Ola Sveen

Characterization of the Microstructural Development through Screw Extrusion of AA6060 and AA6082

NTNU
Norwegian University of
Science and Technology